The Dissertation Committee for Sang Ok Kim Certifies that this is the approved version of the following dissertation:

Development of Nanostructured Alloy-based Composite Anode Materials for Lithium- and Sodium-Ion Batteries

Committee:

Arumugam Manthiram, Supervisor

John B. Goodenough

Paulo J. Ferreira

Guihua Yu

Gyeong S. Hwang

Development of Nanostructured Alloy-based Composite Anode Materials for Lithium- and Sodium-Ion Batteries

by

Sang Ok Kim, B.S.; M.S.

Dissertation

Presented to the Faculty of the Graduate School of

The University of Texas at Austin

in Partial Fulfillment

of the Requirements

for the Degree of

Doctor of Philosophy

The University of Texas at Austin

August 2016

Dedication

Dedicated to my wife, Kangmi Lee, and my precious daughter, Joowon Kim

Acknowledgements

I would foremost like to express my sincere appreciation to my supervisor, Professor Arumugam Manthiram, for all his continuous support and guidance during the pursuit of my degree. Without his persistent help, I could not have developed my research work successfully. I would also like to give a special thanks to my committee members, Professors John B. Goodenough, Paulo J. Ferreira, Gyeong S. Hwang, and Guihua Yu, for their valuable suggestions on my dissertation. I would also like to thank my financial supporting institution: the U. S. Department of Energy, Office of Basic Sciences, Division of Materials Sciences and Engineering.

Additionally, I would like to thank the former and current members in Prof. Manthiram's group, especially anode group members, Dr. Eric Allcorn and Dr. Il-Tae Kim, for their valuable discussion, insightful brainstorming, and sincere assistance with experiments. I also thank Craig Milroy for helping me with XPS measurement and data analysis. I must thank all Korean colleagues who share lots of time and memories with me, which made my time in Austin so enjoyable.

Lastly, and most importantly, I am really thankful to my wife, Kangmi Lee, for her love and sacrificial support during the course of my work. I must thank my parents, parents-in-law, brother, aunt, and friends in Korea for believing and supporting me. This dissertation would not have been possible without them.

Development of Nanostructured Alloy-based Composite Anode Materials for Lithium- and Sodium-Ion Batteries

Sang Ok Kim, Ph.D.

The University of Texas at Austin, 2016

Supervisor: Arumugam Manthiram

Lithium-ion batteries are the dominant energy storage technology in portable electronic applications due to their high energy density, long cycle life, and low self-discharge rate. Efforts to extend their implementation into rapidly growing electric vehicles and large-scale stationary energy storage devices require further improvements of performance and safety, as well as cost reduction. In this regard, the development of low-cost, advanced electrode materials for next generation lithium-ion batteries or sodium-ion batteries is increasingly being pursued to achieve these requirements. The purpose of this dissertation is to explore and develop several types of composite alloy-based anodes that can possibly lead to the enhancement of lithium- or sodium-storage performance.

Alloy anodes have shown great potential for realization of high-performance lithium- or sodium-ion battery systems with enhanced safety as they offer high theoretical specific capacity and higher operating voltages than graphite. In addition, the successful employment of earth-abundant materials such as silicon and phosphorus could also result in a reduction in battery manufacturing cost. However, the major obstacles associated with the large volume change upon electrochemical reactions give rise to severe capacity

fading in the first few cycles, making their implementation into commercial cells quite challenging.

In order to overcome this issue, the alloy-based composite anodes are synthesized by applying the active/inactive matrix concept. The composites are capable of possessing the following advantages: (i) structural reinforcement and suppression of particle agglomeration upon cycling through a mechanically durable buffer; (ii) enhanced electrochemical reversibility and fast electrode kinetics through nanoscale active materials; (iii) high conductivity and facile electron transport through a conducting phase; (iv) high chemical and electrochemical stability through an electrochemically inert buffer. Moreover, the composites synthesized have reasonably high tap density that is beneficial for improving the volumetric capacity of lithium- or sodium-ion cells.

In this dissertation, three different low-cost alloy-based composite anodes are developed by a low-cost, facile, and scalable high-energy mechanical milling: silicon-, zinc-, and phosphorus-based composites. All the composite systems studied in this work demonstrate enhancements in lithium- or sodium-ion storage performance in terms of high capacity, long cycle life, and high rate capability, while maintaining high tap density. By controlling the type and amount of an inactive matrix, the effects of each inactive matrix on the electrochemical performance of the composite anodes are investigated. In addition, the mechanism for the performance improvement is discussed.

Table of Contents

List of Tables

List of Figures

Chapter 1: Introduction

1.1 MOTIVATION

Since the first commercialization in 1991 by Sony Corporation, lithium-ion batteries have become the most widely used power source for portable electronics owing to their advantages such as high energy density, long cycle life, and low self-discharge rate. In recent years, with the rapid growth of emerging technologies including electric vehicles and grid-scale energy storage systems, there has been a great interest in the advancement of high-performance lithium-ion battery systems in terms of higher energy density, higher power capability, as well as enhanced safety. In this regard, rapid development of novel electrode materials with improved performance is considered to be indispensable and should be successfully accomplished.

For the anode materials, graphite is the most commonly used in commercial lithium-ion batteries. However, its major drawbacks including low theoretical specific capacity, poor rate capability, and severe safety issues associated with lithium plating have led to an extensive search for several alternative alloy-based anode materials. Enormous efforts have been dedicated to replace graphite with high capacity lithium-alloy systems in order to satisfy the ever-increasing demand for high performance lithium-ion batteries. Although such lithium-alloying compounds have much higher theoretical capacities than graphite, they inevitably suffer from the large volume change during cycling that leads to the active material pulverization and electrode degradation, resulting in poor cycle and rate performance. Nevertheless, a successful implementation of these alloy-based anode candidates into commercial battery systems would offer a breakthrough in the field of lithium-ion batteries, ensuring that they could play a crucial role in powering a variety of emerging applications in the future.

1.2 LITHIUM-ION BATTERIES

Lithium-ion battery is a secondary battery which outperforms other rechargeable batteries such as lead-acid, nickel-cadmium, and nickel-metal hydride in terms of high operating voltages of ~ 4 V, high gravimetric and volumetric energy densities, excellent cyclability, low self-discharge, and negligible memory effect.[1, 2]

1.2.1 Principle of Operation

Lithium-ion battery is classified as an electrochemical device that can deliver and store electricity through a movement of lithium ions and electrons back and forth between an anode and a cathode. Figure 1.1 shows the lithium-ion battery system composed of a $LiCoO_2$ cathode and a graphite anode, which are immersed in a liquid electrolyte and separated by a polymeric separator.

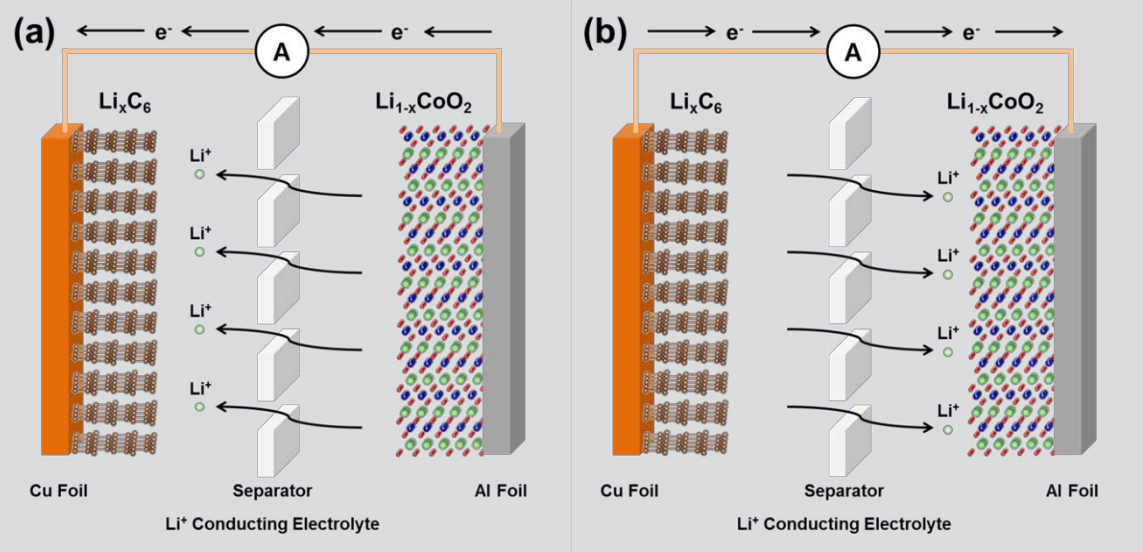

Figure 1.1. Representation of the electrochemical reactions occurring during the (a) charge and (b) discharge processes in a lithium-ion battery.

During the charge process (Figure 1.1(a)), lithium ions are extracted from the $LiCoO_2$ cathode and they move to the graphite anode, forming a Li_xC_6 intercalation

compound. Simultaneously, electrons flow from the cathode to the anode to maintain charge neutrality. The half-cell reactions occurring during charging are described below:

$$\text{Cathode:} \quad LiCoO_2 \rightarrow Li_{1-x}CoO_2 + x\,Li^+ + x\,e^- \qquad (1.1)$$

$$\text{Anode:} \quad C_6 + x\,Li^+ + x\,e^- \rightarrow Li_xC_6 \qquad (1.2)$$

Upon discharge (Figure 1.1(b)), the Li_xC_6 compound is converted back to graphite by releasing lithium ions. Lithium ions migrate to the cathode along with electrons and are inserted into the layered $Li_{1-x}CoO_2$ structure, reversibly forming $LiCoO_2$. Thus, the reverse half-cell reactions taking place during discharging are:

$$\text{Cathode:} \quad Li_{1-x}CoO_2 + x\,Li^+ + x\,e^- \rightarrow LiCoO_2 \qquad (1.3)$$

$$\text{Anode:} \quad Li_xC_6 \rightarrow C_6 + x\,Li^+ + x\,e^- \qquad (1.4)$$

Since the liquid electrolyte is ionically conducting, but electronically insulating, lithium ions can move between the cathode and anode only through the liquid electrolyte and electrons can flow through an external circuit during the charge and discharge operation.

As mentioned previously, lithium-ion batteries are capable of having high operating voltages and high energy densities originating from the very low standard reduction potential of the Li/Li^+ redox couple (–3.05 V vs. Standard Hydrogen Electrode). Figure 1.2 shows the schematic energy diagram of the cathode, anode, and electrolyte in a lithium-ion battery. The open circuit voltage (V_{oc}) of a lithium ion battery can be determined by the chemical potential difference between lithium ions in the cathode and anode and calculated by equation (1.5):

$$V_{oc} = (\mu_c - \mu_a) / F \qquad (1.5)$$

where F is the Faraday constant (= 96485 C mol^{-1}). The difference in lithium chemical potentials is the driving force to convert the chemical energy into electrical energy.

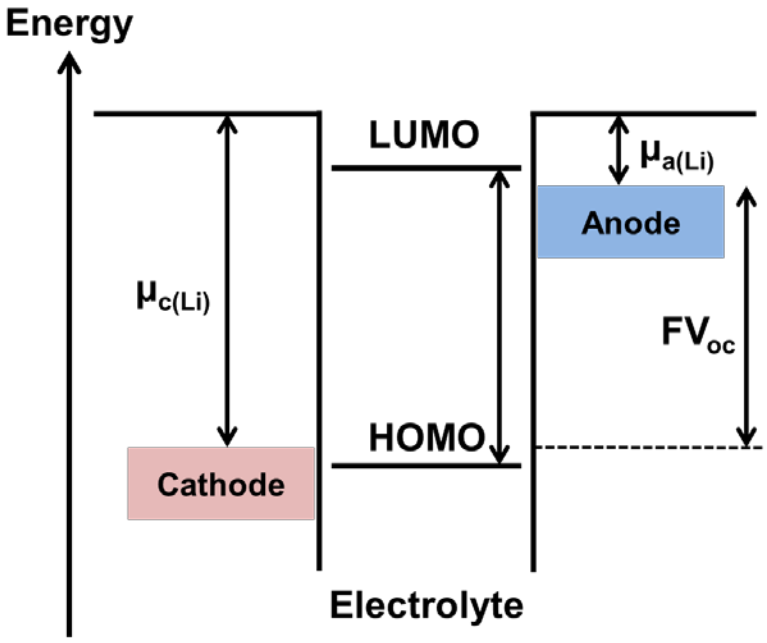

Figure 1.2. Schematic diagram of the energy diagram in a lithium-ion battery.

From Figure 1.2, it is obvious that a high voltage as well as a high energy density can be achieved by employing a cathode material with a lower lithium chemical potential ($\mu_{c(Li)}$) and an anode material with a higher lithium chemical potential ($\mu_{a(Li)}$). Due to the high operating voltage of ~ 4 V in lithium-ion batteries, an organic electrolyte with a large electrochemical stability window, which is determined by the energy difference between the highest occupied molecular orbital (HOMO) and lowest unoccupied molecular orbital (LUMO), should be used instead of an aqueous electrolyte with a much

smaller stability window of < 1.23 V.[3] If a cathode material with a lower energy than HOMO of the electrolyte or an anode material with a higher energy than LUMO of the electrolyte are used, undesirable reduction or oxidation of the electrolyte would take place, resulting in poor electrochemical stability during the battery operation.

1.2.2 Anode Materials

In order to be a suitable anode material for lithium-ion batteries, the following requirements need to be satisfied.

i) The anode material should have a high structural stability during the reversible lithium uptake and removal to obtain good cycling performance.

ii) The anode material with a high lithium chemical potential is preferred to achieve a high operating voltage.

iii) The anode material should be able to accommodate a large amount of lithium ions to obtain a high capacity as well as high energy density.

iv) The anode material with a high electronic / ionic conductivity is desirable to achieve a high rate capability.

v) The anode material should have a high thermal stability upon electrochemical reactions

vi) The anode material should have a low reactivity toward an organic electrolyte to avoid the irreversible side reactions.

vii) The anode material should be low-cost and non-toxic.

Metallic lithium is quite an attractive candidate as an anode material because of its extremely high theoretical specific capacity (3860 mA h g^{-1}) and the lowest standard reduction potential (–3.05 V vs. SHE) among all metals.[4] For these reasons, metallic

lithium was adopted as the anode in early rechargeable lithium batteries. The reaction mechanism of metallic lithium upon cycling is simple as shown below:

$$\text{Discharge:} \quad Li \rightarrow Li^{+} + e^{-} \qquad (1.6)$$

$$\text{Charge:} \quad Li^{+} + e^{-} \rightarrow Li \qquad (1.7)$$

In spite of the simple mechanism, there are severe safety concerns in that lithium dendrite growth and continuous electrolyte decomposition occur during repeated lithium deposition and dissolution, hindering the practical implementation of metallic lithium anode.[5] Therefore, effective suppression of lithium dendrites and formation of stable passivation layer on the lithium surface may be the key factors for metallic lithium to be a viable anode candidate for lithium rechargeable cells.

1.2.2.1 Graphite Anodes

Due to the aforementioned safety issues of lithium metal, the commercial lithium-ion batteries use graphite anodes operated based on the "rocking chair" concept,[6] which stores and delivers electrical energy by reversible intercalation / deintercalation of lithium ions into / from graphite. Graphite is a polymorph of the elemental carbon with two-dimensional layered structure, as shown in Figure 1.3. As an anode in lithium-ion batteries, graphite has several advantages such as good cyclability, thermal stability, and low operating voltage of below 0.1 V.[7] Graphite can accommodate one lithium atom for every six carbon atoms, forming LiC_6. Because of its highly reversible intercalation reaction, the volume expansion after the full lithiation is only about 10% compared to the structure before lithiation.[8] This small volume change is the reason for the high structural stability during electrochemical reactions, leading to desired cycle performance.

However, the low reduction potential (< 0.1 V) of lithium intercalation reaction into graphite, which is close to that of lithium deposition, causes potential safety issues related to lithium plating on the surface of graphite, especially upon fast charge process. During the initial lithium intercalation process, graphite forms stable solid electrolyte interphase (SEI) layer as a result of electrolyte reduction.[9, 10] This SEI layer acts as a protection against further decomposition of electrolyte, leading to an improvement in cycling stability. On the other hand, it prevents rapid transfer of lithium ions into the graphite structure, thereby resulting in a sluggish lithium ion diffusion and possible lithium plating / dendrite formation on the electrode surface.[11] In addition, other drawbacks including the limited theoretical capacity (LiC_6: 372 mA h g^{-1}) and relatively low tap density of ~ 1.0 g cm^{-3} have prompted interest in alternative alloy-based anode materials.

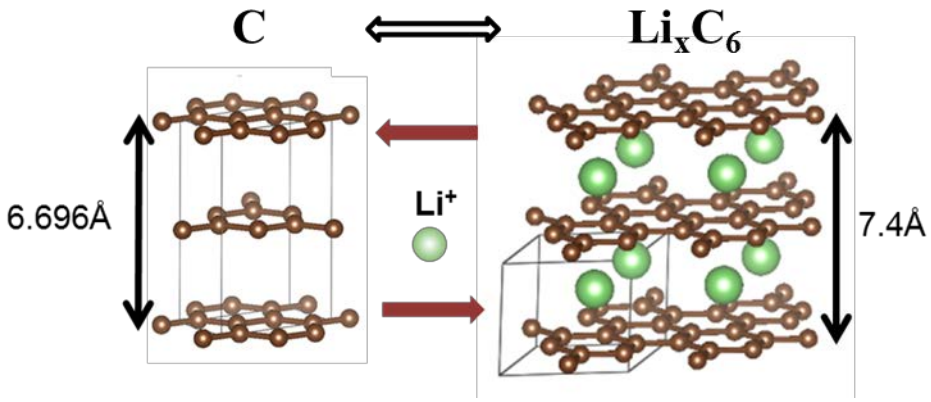

Figure 1.3. Schematic illustration of the structural variation of graphite during lithium intercalation and deintercalation.

1.2.2.2 Lithium Alloy Anodes

Due to several disadvantages of graphite, considerable efforts are being devoted to develop high capacity lithium-alloy systems. Lithium-alloy anodes are generally metallic or semi-metallic elements that can accommodate larger amounts of lithium in their structure. Some of the promising alloy-based anode materials are summarized in Table 1.1. The reaction mechanism of these alloy-based anodes upon cycling can be described as shown below:

$$\text{Discharge:} \quad M + x\,Li^{+} + x\,e^{-} \rightarrow Li_xM \qquad (1.8)$$

$$\text{Charge:} \quad Li_xM \rightarrow M + x\,Li^{+} + x\,e^{-} \qquad (1.9)$$

The primary advantage of using these alloy-based materials lies in the high theoretical specific capacities arising from the large stoichiometric ratio of lithium in the fully lithiated phases.[12, 13] Depending on the type of element, the specific capacity can reach > 3000 mA h g^{-1}, which is significantly higher compared to that of graphite. Moreover, the average operating voltages of these materials are generally in the range of 0.3 – 1.0 V (vs. Li/Li^{+}), resulting in a reduction in the potential risk of lithium plating or dendrite formation on the electrode surface. However, these alloy-based materials suffer from a large volume variation during the lithium alloying/dealloying processes that lead to mechanical failures of active materials and electrode pulverization,[14] making their commercialization quite challenging. In addition, particle cracking and crumbling occurring during electrochemical cycling causes continuous formation of the SEI layer, leading to poor electrochemical reversibility and a large irreversible capacity loss. In order to overcome these problems, extensive research has been conducted to develop

high capacity alloy-based materials with a focus on achieving long cycle life, high rate capability, good safety, and affordability.

Table 1.1. Comparison of lithium alloy-based materials.[12, 13]

Element	Lithiated phase	Volume expansion (%)	Average operating voltage (V)	Specific capacity (mAh g^{-1})
Si	$Li_{15}Si_4$	280	0.3	3579
Sn	$Li_{22}Sn_5$	244	0.5	993
Sb	Li_3Sb	147	0.948	660
Bi	Li_3Bi	126	0.82	385
Zn	LiZn	98	0.3	410
P	Li_3P	300	0.85	2596

Compared to other candidates, silicon has been regarded as the most promising material due to its highest theoretical capacity ($Li_{15}Si_4$, 3579 mA h g^{-1}).[15, 16] However, as shown in Figure 1.4, a large volume change (~ 300 %) upon lithium uptake and removal leads to pulverization of silicon particles and mechanical failure of the electrode.[17, 18] In addition, silicon has a low electrical conductivity and suffers from the formation of unstable SEI during cycling, which consequently results in poor rate capability and severe capacity fade.[19, 20] Several approaches for developing silicon-based anode materials have been proposed and implemented to overcome these shortcomings of silicon anodes. One such technique is the utilization of silicon nanostructures including nanowires,[17, 21, 22] nanorods,[23] and nanotubes,[24] which have led to improved cycling stability by accommodating the volume variation during cycling and enhanced rate

performance by shortening the lithium-ion diffusion length. Another promising technique is to make the composites with electrochemically inactive volume buffer phases. The composite system results in a homogeneous distribution of active/inactive phases in which the inactive phases do not react with lithium and remain unchanged during cycling, thereby reducing the internal stresses arising from the drastic volume change of the active particles and providing structural reinforcement for the electrodes. Owing to the above advantages, silicon-based composites composed of active silicon with various inactive metal silicides ($FeSi_2$, $CoSi_2$, $NiSi_2$, $TiSi_2$, Cu_3Si, and MnSi) or metal oxides (Al_2O_3 and Li_2O_2) have demonstrated enhanced lithium-storage performance over extended cycling.[25-32]

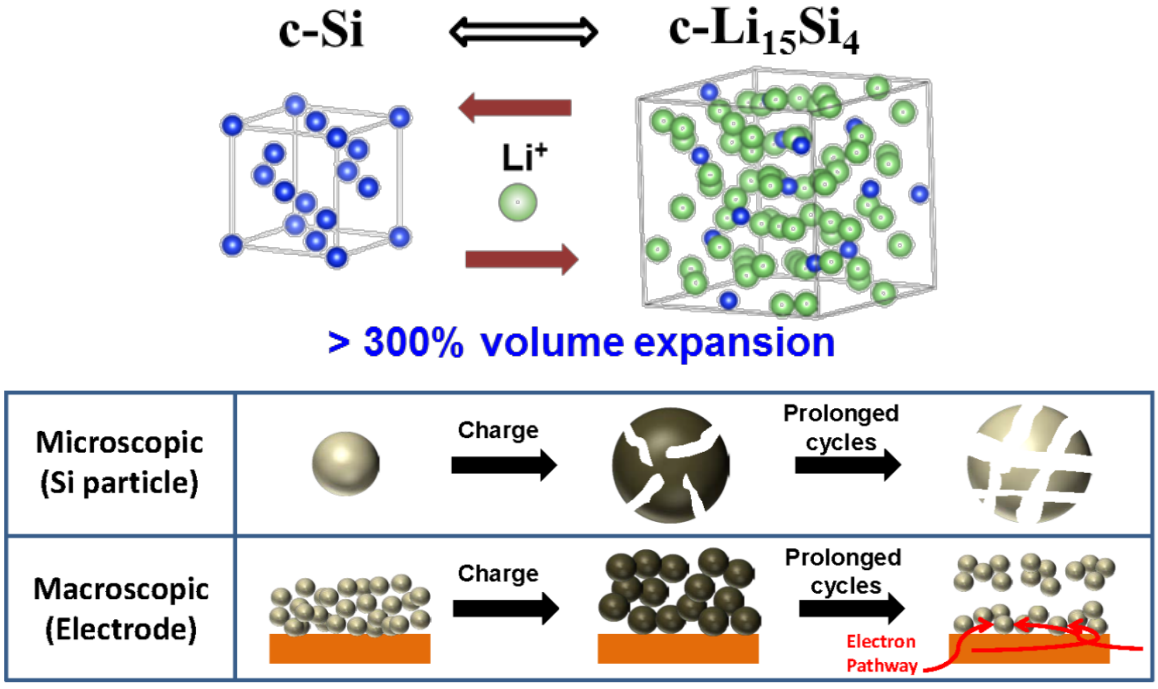

Figure 1.4. Schematic illustration of the volume variation of silicon and subsequent failure mechanism during cycling.

Elemental zinc is another possible option as a lithium-alloy based materials. Even though it has a relatively low theoretical gravimetric capacity (LiZn: 410 mA h g^{-1}) that is only slightly greater (~ 10%) than graphite, it has several advantages such as high volumetric capacity (1511 mA h cm^{-3}) and low operating voltage of < 0.4 V (vs. Li/Li^{+}). Other beneficial features including low cost, natural abundance, and eco-friendliness make it a desirable and promising candidate to be used as an anode material in LIBs.[13] Despite these merits, zinc has not attracted much attention because it also suffers from volume change during electrochemical processes and particle agglomeration upon extended cycling that eventually results in a severe capacity fade and poor rate capability, similar to other alloy-based materials. Accordingly, only a few studies on the synthesis and characterization of zinc-based anode materials have been reported.[33-37] Among them, use of a mixed Al_2O_3 and carbon matrix as an efficient buffer for zinc anode led to a relatively good cycling stability with a reversible capacity of ~ 380 mA h g^{-1} after 100 cycles,[37] thereby representing the feasibility of the active/inactive composite strategy.

Recently, elemental phosphorus has gained a wide interest as one of the most promising anode materials due to its high theoretical capacity of 2595 mA h g^{-1} for lithium-ion batteries, based on the formation of Li_3P.[38, 39] Among the three allotropes of phosphorus (white, red, and black), red phosphorus has several beneficial features such as high reactivity towards lithium, relatively high chemical stability, abundance, and eco-friendliness.[40] However, its major obstacles associated with the large volume change (> 300%) upon electrochemical reactions with lithium and low electrical conductivity (1.0×10^{-14} S cm^{-1}) eventually lead to poor cycling stability and a low rate capability.[41, 42] To overcome these problems, various strategies for accommodating the huge volume expansion and enhancing the powder conductivity have been explored. The majority of the studies have focused on developing phosphorus-based composites containing

different kinds of carbonaceous materials, which include phosphorus / graphite,[43-45] red phosphorus / activated carbon,[46] and amorphous red phosphorus / Super P systems.[47, 48] These composite systems with carbon have shown enhanced lithium-ion storage performance originating from the carbonaceous materials that endow improved conductivity and structural stability by acting as buffer matrices against the large volume variation upon repeated cycling.

1.3 SODIUM-ION BATTERIES

1.3.1 Sodium-Ion Batteries: Advantages and Challenges

Sodium-ion batteries have recently attracted much attention as a promising alternative to conventional lithium-ion batteries for large scale grid storage systems due to the low cost and high abundance of sodium-containing resources on earth's crust, in contrast to lithium sources of limited supply.[49-51] Moreover, the standard reduction potential of sodium (–2.71 V vs. SHE) is low enough to obtain a high operating cell voltage of > 3 V. However, there are also challenges to realize high-performance sodium-ion battery systems due to the size difference between sodium (1.02 Å) and lithium (0.76 Å) ions. The large size difference inevitably leads to a variety of problems, such as mechanical failure of the active materials due to the huge volume change during the sodium insertion/extraction processes, low rate capability resulting from a sluggish sodium-ion diffusion, and electrochemical instability caused by the formation of the unstable SEI layer.[41]

1.3.2 Anode Materials

The requirements for a suitable anode material for sodium-ion batteries are identical to those for lithium-ion batteries, as described in section 1.2.2 above. Here, hard

carbons and some of the alloy-based materials will be briefly introduced as potential anode candidates for sodium-ion batteries.

1.3.2.1 Hard Carbon Anodes

Although graphite shows good electrochemical performance in lithium-ion batteries, it delivers negligible reversible capacity in sodium-ion batteries. Sodium ions cannot be intercalated into the interlayer of graphite (d = ~ 0.34 nm) because the size of sodium ions is larger than that of lithium ions. Early study conducted by Doeff *et al.* revealed that sodium ions can undergo reversible insertion/extraction into/from hard carbon anodes such as petroleum coke and Shawinigan black.[52] Hard carbons are distinct from graphite in terms of their structure. While graphite has a two-dimensionally well-oriented layered structure, hard carbons are composed of randomly oriented graphene layers with a larger interlayer spacing, allowing insertion/extraction of sodium ions. In this regard, various kinds of hard carbons have been studied as potential anodes for sodium-ion batteries. Hard carbons including carbon black, pyrolized glucose, and sucrose have demonstrated sodium intercalation and deintercalation during cycling, with reversible capacities in the ranges of 150 – 300 mA h g^{-1}.[53-55] In addition, the realization of nanostructured morphology or porous structure has also proven that they are effective ways to enhance the electrochemical performance of hard carbon materials due to the reduction in sodium diffusion distance and formation of additional sodium storage sites.[56-58]

1.3.2.2 Sodium Alloy Anodes

Due to the resemblance of the operating mechanisms of lithium-ion and sodium-ion batteries, various alloy-based anode candidates for lithium-ion batteries have been tested. Of those, it has been shown that tin,[59] antimony,[60] and phosphorus[40] undergo

reversible uptake and removal of sodium upon electrochemical cycling. Some of the potential alloy-based anode materials are summarized in Table 1.2.

Table 1.2. Comparison of sodium alloy-based materials.[61]

Element	Sodiated phase	Volume expansion (%)	Average operating voltage (V)	Specific capacity (mAh g^{-1})
Sn	$Na_{15}Sn_4$	420	0.5	847
Sb	Na_3Sb	293	0.948	660
P	Na_3P	491	0.4	2596

Among these candidates, elemental phosphorus and metal phosphide systems have been intensively studied as a high capacity anode material for sodium-ion batteries in recent years. It is known that phosphorus can accommodate up to three sodium ions to give Na_3P, and therefore has the highest theoretical capacity of 2596 mA h g^{-1} among the sodium-alloying anodes like tin ($Na_{15}Sn_4$: 847 mA h g^{-1}) and antimony (Na_3Sb: 660 mA h g^{-1}). Despite its remarkably high capacity, phosphorus undergoes a large volume change (~ 490%) during sodiation/desodiation and has low electrical conductivity (1.0×10^{-14} S cm^{-1}) as mentioned previously. These factors eventually lead to severe capacity fade and poor rate performance. Several approaches for developing phosphorus-based anode materials for sodium-ion batteries, alike those for lithium-ion batteries have been employed to solve these drawbacks. For example, the following carbon composite systems have been explored: red phosphorus / carbon nanotubes,[62] amorphous red phosphorus / Super P,[63] phosphorus / graphene,[64] and phosphorene / graphene.[65] They have demonstrated improved sodium-storage performance resulting from conductive

carbon that provides enhanced conductivity and acts as a structure-reinforcing matrix against the large volume change during cycling. Metal phosphide systems (MP_x, M = Sn, Fe, Co, and Ni) have also shown higher reversible capacity, improved cycling stability, and good rate capability by enhancing particle conductivity. The use of these chemistries has resulted in sodiated intermediate phases (Na_xM or Na_xP) that serve as volume-buffer matrices during repeated electrochemical cycling.[66-70]

1.4 Active / Inactive Composite Strategy

Many studies with the concept of an active/inactive composite have demonstrated enhancement in electrochemical performance of alloy-based anodes for both lithium- and sodium-ion batteries.[71-76] The active/inactive composites are generally composed of active components homogeneously mixed with inactive volume buffer matrix, as can be seen in Figure 1.5. In this intermixed structure, the active components can accommodate some amounts of lithium or sodium inside of their structure, thereby storing electrical energy. As mentioned previously, during discharge (insertion) of lithium- or sodium-alloying anodes, the active particles inevitably suffer from large volume change, consequently leading to the pulverization of those particles and electrode degradation. Once these phenomena happen, the active components are no longer reactive toward lithium or sodium and therefore, the reversible capacity of the anode decays rapidly.

The primarily advantage in the use of the inactive components in the active/inactive composites is the suppression of the volume variation of active particles by absorbing the induced stresses during electrochemical cycling. This enables the active components to maintain the reactivity toward lithium or sodium by preserving the structural stability of electrodes. In addition, if the inactive components are highly conductive, faster lithium- or sodium-ion transport is achievable and thereby giving rise

to enhanced rate capability of the obtained composite. Moreover, the incorporation of robust, and tough inactive components effectively results in the reduction of particle size of the active materials, easing the reaction with lithium or sodium and maintaining high electrochemical reversibility. While the use of the active/inactive composite approach has made some progress in lithium- or sodium-alloying anodes, further improvements are required to satisfy the practical demands in terms of cycle life, rate capability, and coulombic efficiency. The realization of a novel nanostructured composite with a suitable choice of inactive reinforcing matrices provides (i) facile electron transport pathway that leads to rapid electrode kinetics, (ii) short diffusion distance of lithium or sodium ions through the formation of active nanoparticles, (iii) suppression of particle agglomeration during cycling by uniformly dispersing nanoscale active particles within the matrix, and (iv) high chemical and electrochemical stability of the nanocomposite in organic electrolyte.

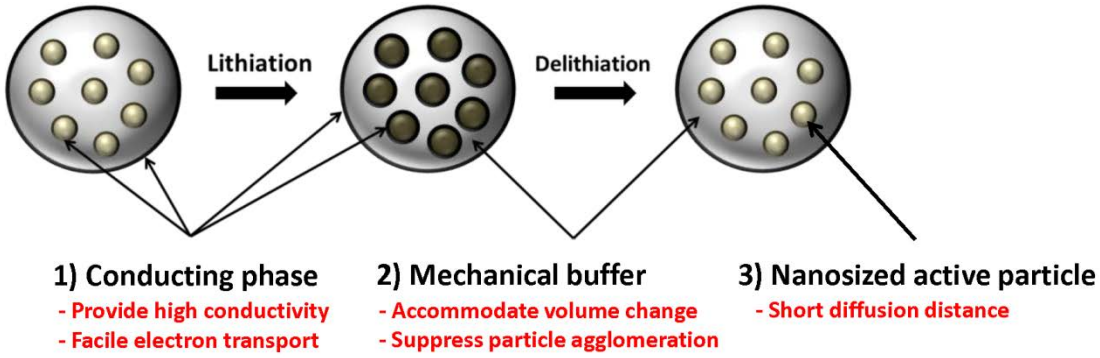

Figure 1.5. Schematic illustration of the advantages of active/inactive composite.

1.5 OBJECTIVES

The overall objective of my dissertation is to develop and explore low-cost and high-performance anode systems using the active/inactive nanocomposite strategy that can overcome the volume change and particle agglomeration issues. In order to be a

promising and practical anode material in lithium- and sodium-ion batteries, the material is required to have a variety of properties: (i) capacity equal to or greater than graphite or hard carbon, (ii) a higher chemical and electrochemical stability for a long cycle life and enhanced safety, (iii) good rate capability for fast charge and discharge processes, and (iv) high tap density for good volumetric and areal capacities. To realize nanostructured composites with the aforementioned properties, a high energy mechanical milling (HEMM) method is employed. The HEMM is a simple, low cost, and scalable process that leads to the *in situ* formation of nanosized active materials well-dispersed in buffer matrices with the aforementioned desired performance.

In Chapters 3 and 4, micro-sized carbon-coated silicon-based composites based on both conductive phase and an inactive buffer matrix concepts are introduced to accomplish high-performance anode systems for lithium-ion batteries. To examine the exact roles of each component in improving cycling stability and rate capability, half-cell performance of the silicon-based composites with and without metal silicides are compared. In addition, the optimized phase composition is explored by varying the amounts of conductive metal silicides incorporated into the composite. In Chapter 3, the feasibility of the composite strategy as a way to achieve an alloy-based anode with high volumetric and areal capacities is assessed by the half-cell behaviors of silicon-based composites with $NiSi_2$ phase. Full cell performance of a silicon-based composite with Cu_3Si anode combined with a commercial spinel cathode is further evaluated in Chapter 4 to determine the practicality of our approach.

In Chapter 5, the active/inactive nanocomposite strategy is applied to develop a micro-sized Zn–TiC–C nanocomposite anode for the high-performance lithium-ion batteries. A combined TiC and amorphous carbon conductive buffer is incorporated in order to mitigate large volume changes during electrochemical cycling and improve the

powder conductivity of the composite particles. The effects of TiC phase, which is highly conductive and electrochemically stable,[77, 78] on the active material utilization, Coulombic efficiency, cycling stability, and rate performance are investigated.

In Chapters 6 and 7, phosphorus and metal phosphide systems prepared by one-step HEMM are investigated. For the CuP_2/C hybrid system studied in Chapter 6, the effects of the amount of conductive carbon and the introduction of stable chemical bonding that can be formed during the synthesis on the electrochemical performance as a durable sodium-storage anode are systematically discussed by employing a combined structural, morphological, and electrochemical characterization. In addition, the application of red phosphorus-based composite with a metal phosphide, TiP_2, as both lithium-ion and sodium-ion battery anodes is studied in Chapter 7. The different mechanisms associated with the performance improvement in lithium-ion and sodium-ion cells are compared.

Chapter 2: General Experimental Procedures

2.1 Materials Synthesis

All the composite systems studied in this dissertation were synthesized by high energy mechanical milling and detailed procedures are described within each individual chapter.

High-Energy Mechanical Milling

High-energy mechanical milling (HEMM) is one of the most widely used powder processing techniques because of its simplicity, inexpensiveness, high yield, and eco-friendliness. During the HEMM process, a powder mixture loaded into a milling container is subject to a high temperature of around 200 ^{o}C as well as high pressure of about 6 GPa, and undergoes continuous plastic deformation and work hardening processes due to the collision between the mixture and the grinding media, which leads to the production of homogeneously mixed materials.

The HEMM process was performed with a SPEX 8000M mill and planetary ball mill apparatus (Pulverisette 5, Fritsch). The powder mixture was placed in a hardened stainless steel container (80 cm^3) containing hardened steel balls with two different diameters of 3/8 and 3/16 inch. The milling process was carried out under dry and inert atmosphere to minimize oxidation and avoid side reactions.

2.2 Materials Characterization Techniques

2.2.1 X-Ray Diffraction (XRD)

Powder X-ray diffraction (XRD) was performed on the as-synthesized samples with a Philips and Rigaku Miniflex 600 X-ray diffractometers with Cu Kα (λ = 1.54059 Å) radiation at a scan rate of 0.02^{o} s^{-1} over a scattering angle (2θ) range of $10 – 80^{o}$. The JCPDS crystallographic database was used to determine the crystalline phases generated

during the synthesis. To investigate the phase changes during cycling, *ex situ* XRD was conducted with electrodes at different states of charge (SOC). Cycled electrodes were obtained by disassembling the coin cells. The electrodes were washed with dimethyl carbonate (DMC), and dried in an argon-filled glove box for 30 min. Then, each electrode was sealed with Kapton polyimide tape before the XRD measurement.

2.2.2 X-Ray Photoelectron Spectroscopy (XPS)

X-ray photoelectron spectroscopy (XPS) was carried out with a Kratos Analytical X-ray photoelectron spectrometer with monochromatic Al Kα X-ray source at 150 W. The use of XPS provides information on chemical bonding and oxidation states of the composite samples, which makes it possible to determine the formation of amorphous phases that are undetectable by the XRD analysis. After the XPS measurement, the obtained XPS spectra were manually shifted based on C 1s peak position (284.5 eV) in order to eliminate sample charging effects. The peak analysis was conducted using Casa XPS software.

2.2.3 Scanning Electron Microscopy and Energy Dispersive X-Ray Spectroscopy (SEM/EDS)

In scanning electron microscopy (SEM), the electrons emitted from an electron gun interact with the surface of the sample, producing the secondary and backscattered electrons that are collected by the detector. From the secondary electrons obtained by inelastic scattering, SEM gives greyscale images of the sample with a resolution less than 0.5 nm. In addition, backscattered electrons obtained by elastic scattering lead to the strong image contrast, allowing the detection of chemical compositions of the specific area of the sample. In this dissertation, the surface morphology and elemental composition of the powder samples and cycled electrodes were investigated with a JEOL

JSM–5610 SEM equipped with Energy Dispersive X-ray Spectroscopy (EDS) operating at an accelerating voltage of 20 kV.

2.2.4 Transmission and Scanning Transmission Electron Microscopy (TEM/STEM)

Transmission electron microscopy (TEM) uses a high-energy electron beam passing through a thin specimen to provide a higher resolution image of the samples that contains information about the microstructure, phase distribution, and crystal orientation. Scanning transmission electron microscopy (STEM) is a type of TEM that is capable of rastering of the electron beam across the sample, producing elemental mapping images. The TEM and STEM analyses in this study were carried out with a JEOL 2010F TEM operating at an accelerating voltage of 200 kV and a Hitachi S–5500 STEM system.

2.2.5 Tap Density Measurement

Tap density of a sample powder is a practical measurement that is closely related to the volumetric capacity of the electrode material. For the measurement, a known mass of sample powder is placed in a graduated cylinder and the cylinder is tapped down on a hard surface. After thousands of times, the volume of the sample is measured and the tap density can be calculated by dividing the weight of the powders by the measured volume. The tap density of the samples was determined with a Quantachrome AT–4 Autotap machine.

2.2.6 Thermogravimetric Analysis (TGA)

Thermogravimetric analysis (TGA) was carried out with a Netzsch STA449 F3 Jupiter system. A small quantity of composite powder was placed in an alumina crucible and heated up to 900 ^{o}C under an air atmosphere. After cooling down to room temperature, the measured weight loss or gain is compared to the initial weight of the sample to estimate the carbon content in the sample powders.

2.3 ELECTROCHEMICAL CHARACTERIZATION

2.3.1 Electrode Preparation

Electrodes were prepared by conventional doctor-blade method. Slurries composed of 70 wt. % active material, 15 wt. % conducting agent (Super P), and 15 wt. % binder were left under magnetic stirring until completely mixed. The mixtures were pasted onto copper foil current collector and dried in a vacuum oven for several hours to remove moisture. The electrodes were then punched into disks with an area of ~ 1.0 cm^2. Two different types of binders were used to prepare the electrodes depending on the active materials. The electrodes for the active materials with large volume change during cycling were made with the polyacrylic acid (PAA) binder dissolved in water. Otherwise, conventional polyvinylidene fluoride (PVdF) binder dissolved in N-methyl pyrrolidinone (NMP) was used to fabricate the electrodes.

2.3.2 Coin Cell Assembly

The disk electrodes were assembled into CR2032 type coin cells in an argon-filled glove box with H_2O and O_2 concentrations less than 5 ppm to avoid contamination of the electrodes. Half cells were fabricated with the disk electrode as the working electrode, polypropylene (Celgard 2400) as the separator, and lithium or sodium metal foil as the counter / reference electrode. For full cell configurations, the working electrode was the disk electrode containing the cathode material and the counter / reference electrode was the disk electrode with the anode material, instead of using the metal foil. The coin cells were then filled with an appropriate amount of an organic electrolyte prior to crimping. The used electrolyte was 1 M $LiPF_6$ dissolved in a 50 : 50 vol. % mixture of ethylene carbonate (EC) and diethyl carbonate (DEC) in most cases. The electrolyte with

fluoroethylene carbonate (FEC, 5 – 30 vol. %) as an additive was used for long-term cycling tests.

2.3.3 Galvanostatic Charge and Discharge Cycling

The test cells were cycled within specified voltage ranges (generally, 0 – 2.0 V vs. Li / Li^+) at various current densities with an Arbin automated battery cycler to assess the cycle and rate performance.

2.3.4 Electrochemical Impedance Spectroscopy (EIS)

Electrochemical impedance spectroscopy (EIS) experiments were performed with an impedance/gain-phase analyzer (Solartron SI 1260) equipped with an electrochemical interface (Solartron SI 1286). The EIS data were recorded at the open-circuit potential of the cells with the AC amplitude of 5 mV over a frequency range from 100 kHz to 0.1 Hz.

Chapter 3: A Facile, Low-Cost Synthesis of High-Performance Silicon-based Composite Anodes with High Tap Density for Lithium-Ion Batteries[†]

3.1 INTRODUCTION

To meet the requirements of the rapid development of a wide range of new and large-scale energy storage systems and smart grids, considerable efforts are being devoted to develop electrode materials with high capacity and long cycle life for lithium-ion batteries.[79] In this regard, silicon-based materials have attracted significant attention as an anode and are considered as the most promising candidate to replace the currently used graphite anode. In contrast to the limited theoretical capacity of graphite (372 mA h g^{-1}, 830 mA h cm^{-3}), silicon possesses significantly higher gravimetric (~ 3579 mA h g^{-1}) and volumetric capacities (~ 7000 mA h cm^{-3}). In addition, silicon is abundant, inexpensive, and environmentally benign.[80-82] However, its commercial use is still impeded by the major drawbacks associated with the large volume change (~ 300%) and formation of unstable SEI layer during the lithium insertion/extraction processes that lead to structural failure of the electrode and poor capacity retention.[83]

As mentioned in section 1.2.2.2, various nanostructured silicon anodes have shown high-performance owing to their high capacity, long cyclability, and good rate capability. Nevertheless, since they are usually obtained by chemical vapor deposition or chemical etching techniques that rely on using expensive and toxic chemicals, it inevitably leads to high production cost and environmental concerns, making it difficult for large-scale battery applications. Moreover, nanosized silicon has large surface area compared to micro-sized silicon, which reduces the tap density and hinders high loading

[†] S. -O. Kim and A. Manthiram, "A facile, low-cost synthesis of high-performance silicon-based composite anodes with high tap density for lithium-ion batteries." *J. Mater. Chem. A* **2015**, 3, 2399.
S. –O. Kim carried out the experimental work. A. Manthiram supervised the project. All participated in the preparation of the manuscript.

mass, lowering the volumetric capacity. From a practical point of view, development of Si-based anodes with high packing density has become a critical issue. In this regard, a few groups have focused on maintaining high tap density during the preparation of Si-based materials by introducing micro-sized Si particles composed of nano-sized Si building blocks.[84-86]

In order to satisfy the practical demands in terms of high reversible capacity, cycle life, and rate capability, herein, we report the preparation of micro-sized carbon-coated silicon-based composites (hereafter, denoted as Si–$NiSi_2$–Al_2O_3@C) by a simple two-step high energy mechanical milling (HEMM) process and their enhanced electrochemical performance as lithium-ion battery anodes. Schematic diagram of the formation of the Si–$NiSi_2$–Al_2O_3@C composite is shown in Figure 3.1. The as-synthesized Si–$NiSi_2$–Al_2O_3@C composite is composed of well-mixed nanostructured Si/$NiSi_2$ crystallites uniformly embedded in an amorphous Al_2O_3 buffer matrix and further encapsulated by a carbon layer. There are several advantages that should be recognized with regard to this composite. Due to the unique nanostructure with small particle and crystallite size, enhanced lithium-storage kinetics is expected by facilitating fast electronic/ionic transport through short diffusion path and by alleviating the significant volume changes of the active material during cycling.[37, 79] In addition, the presence of $NiSi_2$ phase plays a crucial role in enhancing the electrochemical performance due to the much higher electronic conductivity of $NiSi_2$ (0.35 ~ 0.5 μΩ m) compared to that of silicon (640 Ω m).[87] Moreover, amorphous Al_2O_3 could act as a protective matrix to suppress the formation of SEI films, providing improved interfacial stability during cycling.[71, 88, 89] Finally, high tap density could also be achieved since the overall Si–$NiSi_2$–Al_2O_3@C composite has a micrometer size.

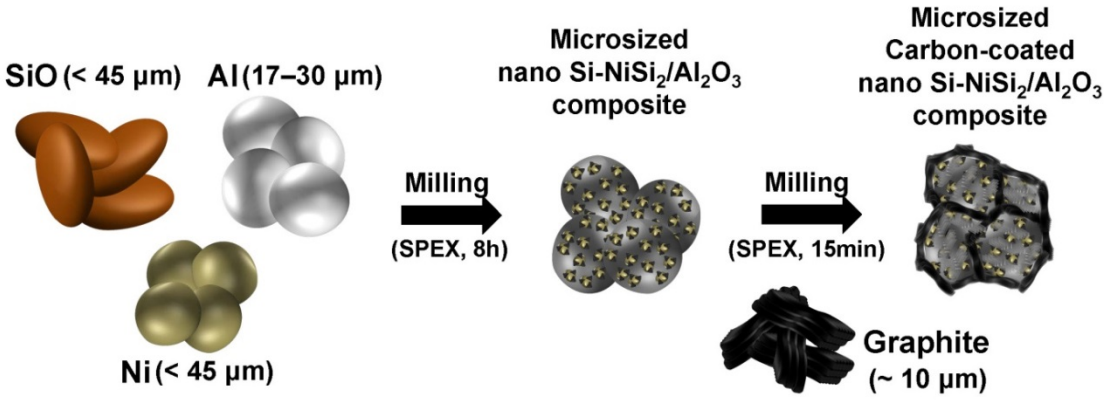

Figure 3.1. Schematic diagram of the formation of the Si–$NiSi_2$–Al_2O_3@C composites by a two-step high energy ball milling method.

3.2 EXPERIMENTAL

3.2.1 Sample Preparation

Silicon-based composites with and without conductive $NiSi_2$ phase were synthesized by a two-step HEMM process. The precursors used for the synthesis were silicon monoxide (SiO, –325 mesh, Aldrich), aluminum (99%, 17–30 μm, Alfa Aesar), nickel (99.9%, –325 mesh, Acros Organics), and commercial graphite (CGP–G8, Conoco) powders. All these chemicals were used as-received without further treatment. For the preparation of the Si–Al_2O_3@C composite, SiO and aluminum powders were mixed with a mole ratio of 6 : 4 and placed in a hardened stainless steel vial (80 cm^3) containing stainless steel balls with two different diameters (three of 3/8 and 14 of 3/16 inch). The vial was sealed and subjected to HEMM for 8 h at room temperature with a SPEX 8000M mill. The milling time was determined by the time required for the complete reduction of SiO to silicon by the mechanochemical reaction with aluminum (Figure 3.2). The HEMM process induced the reaction shown below in reaction (3.1):

$$6\ SiO + 4\ Al \rightarrow 6\ Si + 2\ Al_2O_3 \qquad (3.1)$$

In the second step, the resulting powder and graphite (9 : 1 weight ratio) were milled for 15 min with the same machine in order to provide enhanced powder conductivity. Both steps of the HEMM processes were carried out under an argon atmosphere. The total amount of powder was fixed to be 2.0 g for each step and the ball-to-powder mass ratio was 20 : 1. The final product was ground, sieved, and stored in a vacuum desiccator to minimize surface oxidation.

The Si–$NiSi_2$–Al_2O_3@C composites were prepared by the same method described above with the addition of an appropriate amount of elemental nickel powder (x = 0.5, 0.75, 1.0 in reaction (3.2) below) in the first HEMM step. During the HEMM process, the reduction of SiO to silicon occurs as metallic aluminum is oxidized and then the reduced silicon reacts with nickel to form $NiSi_2$ phase.

$$6\ SiO + x\ Ni + 4\ Al \rightarrow (6 - 2x)\ Si + x\ NiSi_2 + 2\ Al_2O_3 \qquad (3.2)$$

A high average milling yield over 90% was obtained by measuring the total mass after milling and comparing it with that before milling. All the data reported and analyzed here refer to the Si–$NiSi_2$–Al_2O_3@C composite with the optimum amount of nickel (x = 0.75 in reaction (3.2) above), based on preliminary electrochemical studies shown in Figure 3.3. EDS analysis showed no iron-related impurities in the silicon-based composite powders.

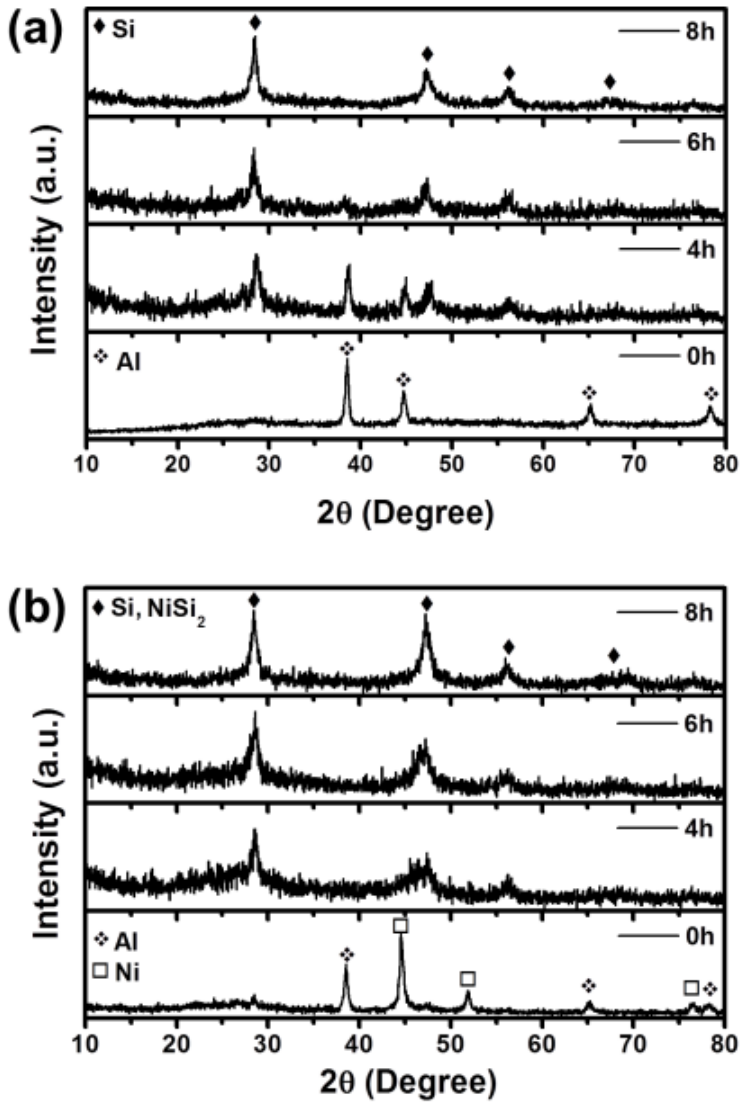

Figure 3.2. XRD patterns of the (a) Si–Al_2O_3@C and (b) Si–$NiSi_2$–Al_2O_3@C (sample prepared with x = 0.75 in reaction (3.2)) composites after different milling times.

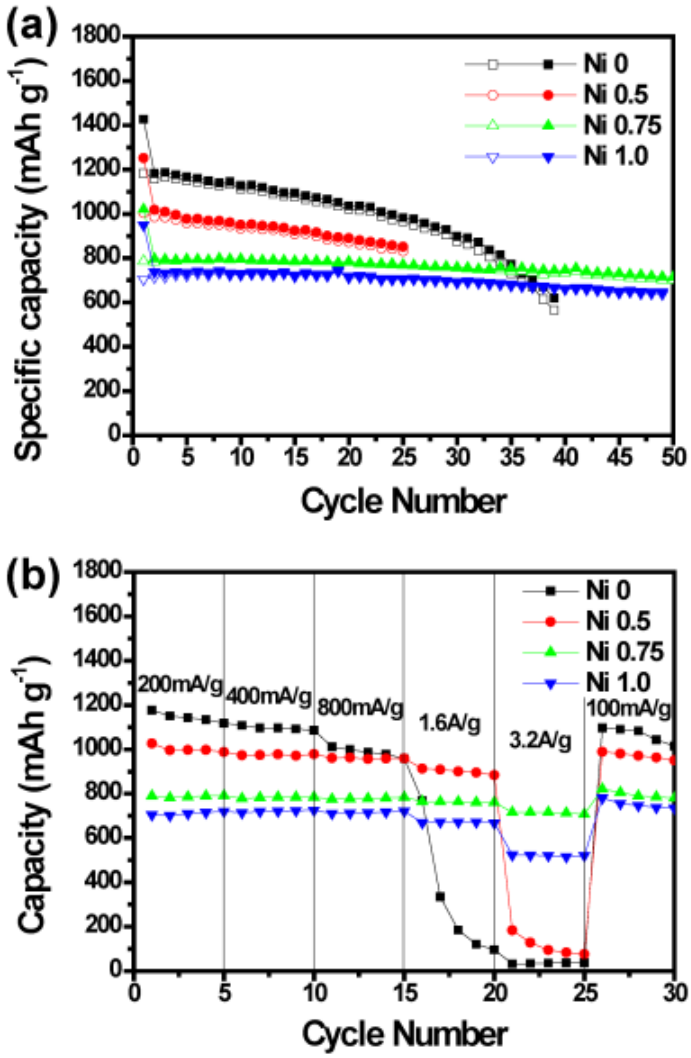

Figure 3.3. (a) Cycle performance of the Si–Al_2O_3@C and Si–$NiSi_2$–Al_2O_3@C composites at a current density of 100 mA g^{-1} within a voltage range of 0.0 – 2.0V (vs. Li / Li^+). (b) Rate performance of the Si–Al_2O_3@C and Si–$NiSi_2$–Al_2O_3@C composites at various current densities. The discharge current density was fixed at 100 mA g^{-1}.

3.2.2 Sample Characterization

The silicon-based composites were examined with a Philips X-ray diffractometer with Cu Kα (λ = 1.54059 Å) radiation at a scan rate of 0.03^{o} s^{-1} over a scattering angle (2θ) range of 10 – 80^{o} and X-ray photoelectron spectrometer (Kratos Analytical). The surface morphology of the powder samples was analyzed with scanning electron microscopy (SEM, JEOL JSM–5610) equipped with EDS and transmission electron microscopy (TEM, JEOL 2010F) operating at an accelerating voltage of 200 kV. The elemental distribution in the silicon-based composite was investigated by scanning transmission electron microscopy (STEM, Hitachi S–5500). For the TEM and STEM characterization, the Si-based composite powders were dispersed and sonicated for 10 min in ethanol, and then dropped onto a carbon-coated copper grid and dried at room temperature to remove the solvent completely. Tap density of the samples was measured with a Quantachrome AT–4 Autotap machine.

3.2.3 Electrochemical Measurements

The test electrodes were fabricated by mixing the slurries containing the active material (silicon-based composites), conducting agent (Super P), and polyvinylidene fluoride (PVdF) binder dissolved in N-methyl pyrrolidinone (NMP) with a weight ratio of 70 : 15 : 15, and then coating the mixture onto a copper foil current collector with a doctor-blade method. The electrodes were then dried in a convection oven at 80 ^{o}C for 1 h and transferred to and stored in a vacuum oven at 120 ^{o}C for over 8 h. After drying, the electrodes were rolled and cut into disks with a diameter of 1.13 cm. The typical mass loading of active material was ~ 1.25 mg cm^{-2}. The half cells were fabricated with CR2032 type coin cells in an argon-filled glove box including the lithium foil as the reference/counter electrode and Celgard 2400 polypropylene as the separator. The electrolyte was 1 M $LiPF_6$ dissolved in a mixture of ethylene carbonate (EC) and diethyl

carbonate (DEC) (1 : 1 vol. %). Long-term cyclability test was performed with the electrodes fabricated with poly(acrylic) acid (PAA) binder (average MW ~250,000, 35 wt. % in distilled water, Aldrich) instead of PVdF in the electrolyte with fluoroethylene carbonate (FEC, 30 vol. %) as an additive. In this case, the electrodes with higher loading mass of active material of ~ 1.65 mg cm^{-2} could be achieved.

Galvanostatic charge-discharge experiments were performed within a voltage range from 0.0 to 2.0 V (vs. Li / Li^+) with an Arbin automated battery tester. The specific capacity was calculated based on the total weight of the active material in the electrode. Rate capability was also assessed by applying various current densities. Electrochemical impedance spectroscopy (EIS) experiments were carried out with an impedance/gain-phase analyzer (Solartron SI 1260) equipped with an electrochemical interface (Solartron SI 1286). The AC amplitude was 5 mV over a frequency range from 100 kHz to 0.1 Hz. To investigate the changes in electrode surface morphology during cycling, *ex situ* SEM analysis was also performed with the electrodes before and after 5, 20, and 40 cycles. The cycled electrodes were disassembled in an argon-filled glove box, washed with DEC several times, and dried at room temperature. Then, they were quickly loaded into the SEM chamber to minimize any unwanted side reactions.

3.3 RESULTS AND DISCUSSION

3.3.1 Structure and Morphology

The XRD patterns of the silicon-based composites are shown in Figure 3.4 and compared with those of pure silicon and $NiSi_2$ phases. All the diffraction peaks of the Si–Al_2O_3@C composite could be indexed to crystalline silicon (JCPDS No. 77-2110, cubic, S.G. = Fd-3m, a = 5.4298 Å), with no other peaks related to oxides or metallic precursors, indicating the successful formation of silicon and amorphous Al_2O_3. Due to

the high reducing power of metallic aluminum, SiO is reduced to silicon with the formation of amorphous Al_2O_3 during the HEMM technique, which is in good agreement with the previous studies on alloy-based composite materials such as silicon,[90, 91] antimony,[88, 89] and zinc.[37] Moreover, graphite peaks were no longer detected owing to the loss of its layered structure by continuous crumbling and pulverization induced by HEMM. When nickel was added, the positions of the characteristic peaks were almost the same to that of the Si–Al_2O_3@C composite, since silicon and $NiSi_2$ (JCPDS No. 43-0989, cubic, S.G. = Fm-3m, a = 5.416 Å) have similar structures and lattice parameters. The structural similarity between silicon and $NiSi_2$ (lattice mismatch below ~ 0.4%) leads to only differences in the peak intensity ratio of the (111) peak to the (220) peak without any noticeable change in the XRD patterns.[27] These results also imply that $NiSi_2$ is the only stable phase formed among the various Ni-Si binary phases.

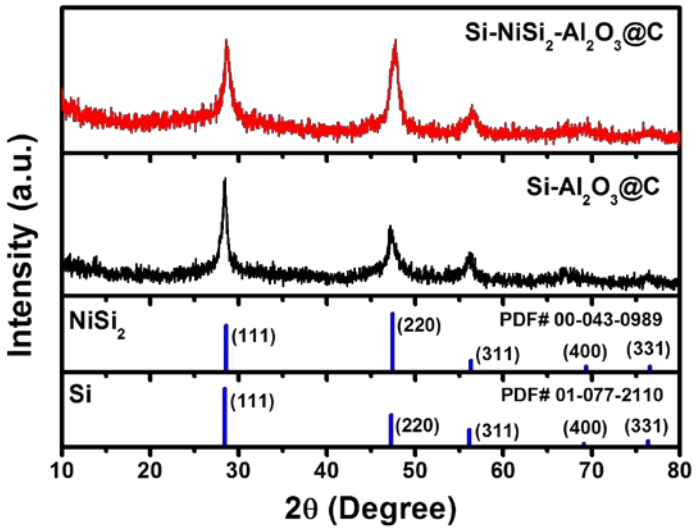

Figure 3.4. XRD patterns of the as-synthesized Si–Al_2O_3@C and Si–$NiSi_2$–Al_2O_3@C composites.

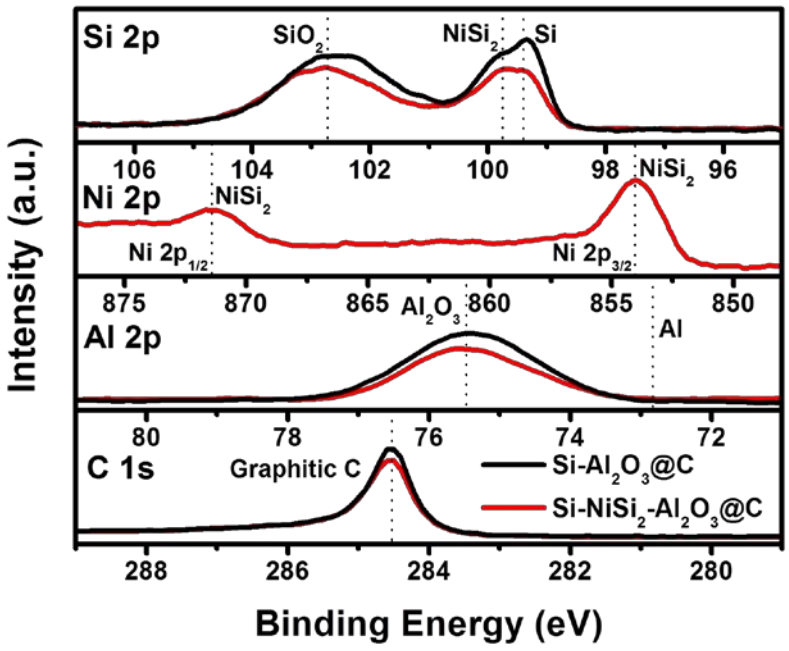

Figure 3.5. XPS spectra in the Si 2p, Ni 2p, Al 2p, and C 1s regions of the silicon-based composites.

The structural characterization of the as-synthesized silicon-based composites was further carried out by XPS measurements as shown in Figure 3.5. The XPS survey spectra of silicon-based composites are compared and the detailed fitting results for Si 2p, Al 2p, and O 1s spectra are shown in Figure 3.6. The XPS spectrum of Si 2p shows the presence of silicon, with the Si $2p_{3/2}$ and Si $2p_{1/2}$ peaks occurring, respectively, at ~ 99.4 and ~ 100.0 eV in the Si–Al_2O_3@C composite.[91] However, in the case of Si–$NiSi_2$–Al_2O_3@C composite, two additional Si 2p peaks appeared at ~ 99.9 (Si $2p_{3/2}$) and ~100.3 eV (Si $2p_{1/2}$) in the Si 2p spectrum and two Ni 2p peaks centered at ~ 854.6 (Ni $2p_{3/2}$) and ~ 871.8 eV (Ni $2p_{1/2}$) appeared in the Ni 2p spectrum, confirming the presence of $NiSi_2$ phase along with silicon.[92] Since the XPS technique has high surface sensitivity, the peak corresponding to SiO_2 (~ 103.5 eV) could also be detected, probably due to the formation

of thin native oxide on silicon surface.[93] The binding energy of Al 2p in Al_2O_3 shows a significant shift to a higher value (~ 75.4 eV) compared to that in metallic aluminum (~ 72.7 eV) because of a higher oxidation state of aluminum, confirming the complete oxidation of Al to Al_2O_3.[89] Meanwhile, the binding energies of carbon in both the Si-based composites were identical, as indicated by the XPS C 1s spectra. The C 1s peak positioned at ~ 284.5 eV is assigned to graphitic carbon in the composite, revealing that graphite was not involved in the mechanochemical reaction. Accordingly, the combination of XRD and XPS data confirms the presence of crystalline silicon, amorphous Al_2O_3, and graphitic carbon in the Si–Al_2O_3@C composite and the additional crystalline $NiSi_2$ in the Si–$NiSi_2$–Al_2O_3@C composite. Based on these results and the ratios of precursors used for the synthesis in accordance with reactions (3.1) and (3.2), the amounts of Si, $NiSi_2$, Al_2O_3, and carbon were estimated to be, respectively, 40.7, 0, 49.3, and 10 wt. % in the Si–Al_2O_3@C composite and 27.3, 18.6, 44.1, and 10 wt. % in the Si–$NiSi_2$–Al_2O_3@C composite, which were found to be almost identical to those obtained by the EDS analysis (Figure 3.7).

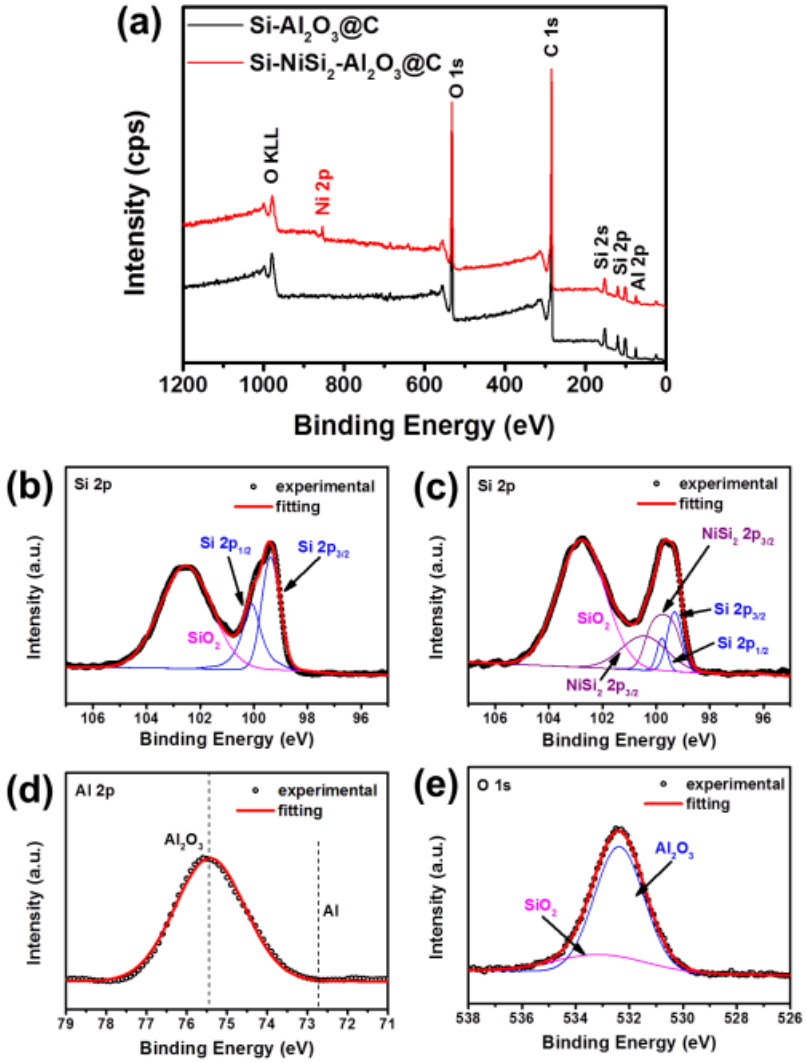

Figure 3.6. (a) XPS survey spectra of the Si–Al_2O_3@C and Si–$NiSi_2$–Al_2O_3@C composites. XPS peak fitting results of (b) Si 2p spectrum in the Si–Al_2O_3@C composite and (c) Si 2p, (d) Al 2p, and (e) O 1s spectra in the Si–$NiSi_2$–Al_2O_3@C composite.

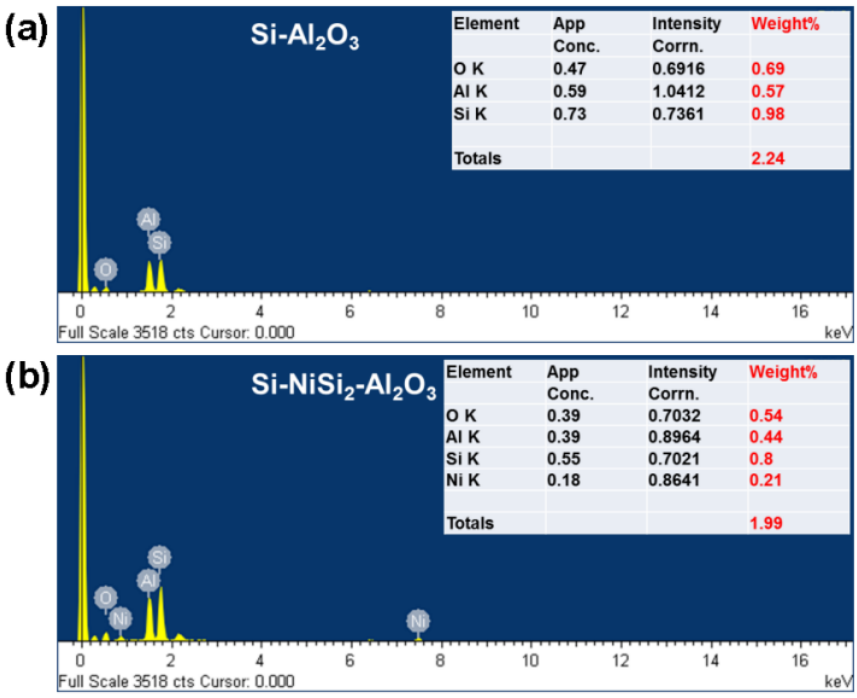

Figure 3.7. SEM/EDS results of the (a) Si–Al_2O_3 and (b) Si–$NiSi_2$–Al_2O_3 composites.

The surface morphology and microstructural evolution of the silicon-based composites during milling were investigated by SEM, TEM, and STEM analyses and the images are shown in Figure 3.8 (TEM and STEM images of the Si–Al_2O_3@C composite are given in Figure 3.9 for a comparison). Apparently, the particle morphology of the as-synthesized Si-based composites with and without $NiSi_2$ appears quite similar. The milled powders have small particle size (a few microns or smaller) as shown in Figure 3.8a and b. We could expect that the micro-sized Si–$NiSi_2$–Al_2O_3@C composites are composed of agglomerated particles containing nanocrystalline silicon and $NiSi_2$, amorphous Al_2O_3, and graphitic carbon.

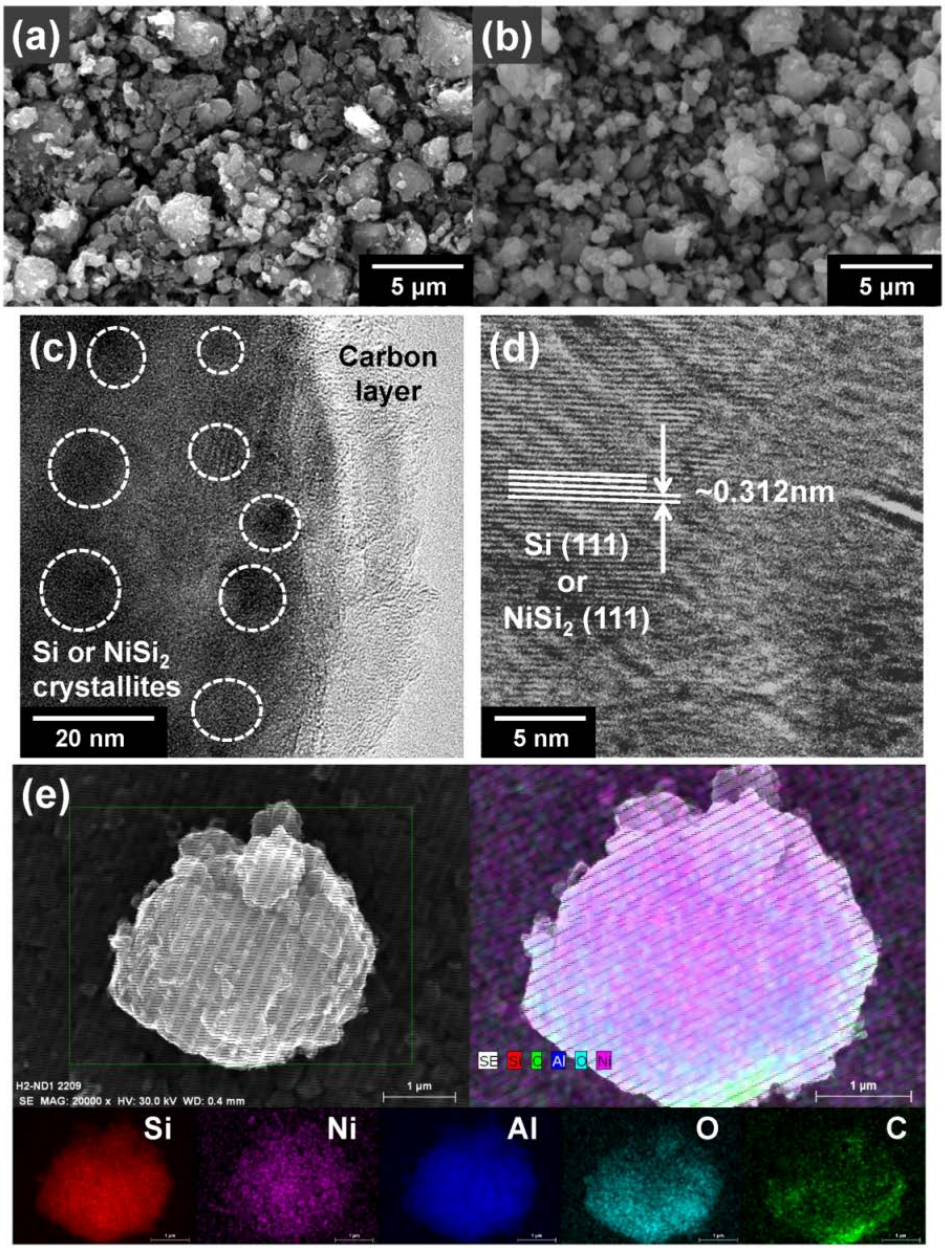

Figure 3.8. SEM images of the ball-milled (a) Si–Al_2O_3@C and (b) Si–$NiSi_2$–Al_2O_3@C composites. (c) TEM, (d) HRTEM, and (e) STEM images of the Si–$NiSi_2$–Al_2O_3@C composite. In STEM, corresponding EDS mapping images of each element are also shown with different colors.

The detailed microstructure of the Si–$NiSi_2$–Al_2O_3@C composite can be elucidated by the TEM and HRTEM images illustrated in Figure 3.8c and d. As shown in Figure 3.8c, the composite particles consist of nanosized crystallites, with diameters roughly ranging from 5 to 10 nm, finely dispersed within an amorphous Al_2O_3 matrix and further encapsulated by carbon layers. This agrees quite well with our XRD and XPS results described above. We could also clearly see the lattice fringes with an interplanar spacing of ~ 0.312 nm in Figure 3.8d, which corresponds to either Si (111) or $NiSi_2$ (111) planes. As mentioned earlier, since both silicon and $NiSi_2$ have cubic symmetry with a very similar lattice parameter, it is difficult to differentiate between silicon and $NiSi_2$ nanocrystallites in the composite particles. However, it is reasonable to assume that highly conductive $NiSi_2$ is generated on the surface of silicon during milling, which gives rise to the formation of well-intermixed Si/$NiSi_2$ nanocrystallites in the composite.[27] The STEM and corresponding EDS mapping images for each element (Si, Ni, Al, O, and carbon) of the Si–$NiSi_2$–Al_2O_3@C composite particle are represented in Figure 3.8e. The mapping results further reveal a homogeneous distribution of Si, $NiSi_2$, Al_2O_3, and carbon in a particle and this unique structure might lead to not only improved particle conductivity but also an effective buffering matrix that mitigates the severe volume changes occurring during cycling.

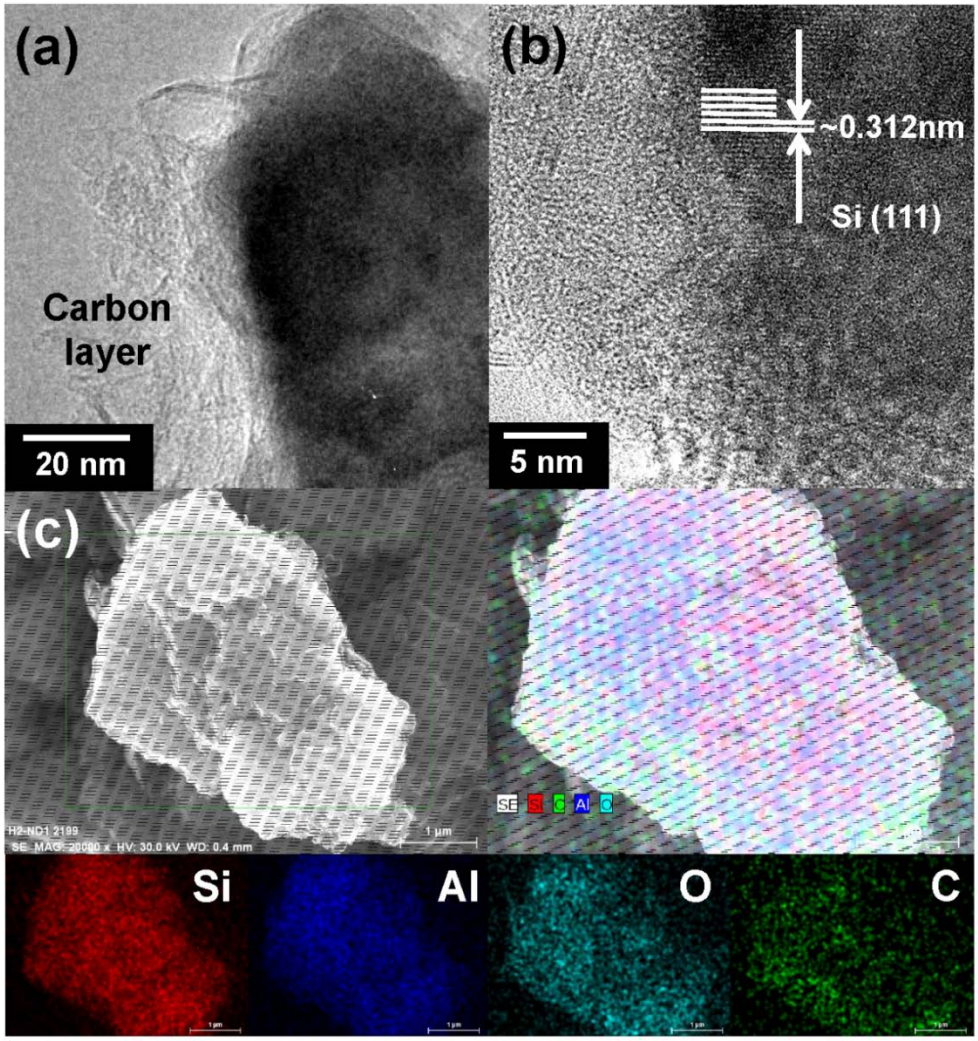

Figure 3.9. (a) TEM, (b) HRTEM, and (c) STEM images of the Si–Al_2O_3@C composite. In the STEM, the corresponding EDS mapping images of each element are also shown with different colors.

3.3.2. Electrochemical Characterization

Electrochemical performance of the silicon-based composite electrodes was characterized by galvanostatic charge-discharge technique at a current density of 100 mA g^{-1} within a voltage range of 0.0 – 2.0 V (vs. Li / Li^+). Figure 3.10a-d represents the voltage profiles and differential capacity plots (DCPs) of the Si–Al_2O_3@C and Si–$NiSi_2$–Al_2O_3@C electrodes. The theoretical and observed specific capacities and Coulombic efficiencies in the first cycle and the capacity retentions are compared in Table 3.1. In both electrodes, there are two potential plateaus located at ~ 0.1 V during discharge (Li insertion) and ~ 0.45 V during charge (Li extraction) in the first cycle and followed by the sloping profiles in the subsequent cycles due to the solid-state amorphization of silicon, showing the typical characteristics of a silicon electrode.[94-96] While the first discharge and charge capacities of the Si–Al_2O_3@C electrode are, respectively, 1427 and 1183 mA h g^{-1} with a high initial Coulombic efficiency of ~ 82.9% (Figure 3.10a), the Si–$NiSi_2$–Al_2O_3@C electrode delivers first discharge and charge capacities of, respectively, 1020 and 787 mA h g^{-1} with a slightly lower initial Coulombic efficiency of ~ 77.1% (Figure 3.10c). Considering that the amorphous Al_2O_3 is inactive to lithium,[71, 90] this is thought to be arising from the irreversible reaction of the $NiSi_2$ in the first cycle,[97] along with the SEI formation.[83, 98] The specific capacity of the Si–$NiSi_2$–Al_2O_3@C electrode remains unchanged over 10 cycles in contrast with that of the electrode without $NiSi_2$, demonstrating the enhanced cycling stability and capacity retention with the aid of highly conductive $NiSi_2$ in the composite.

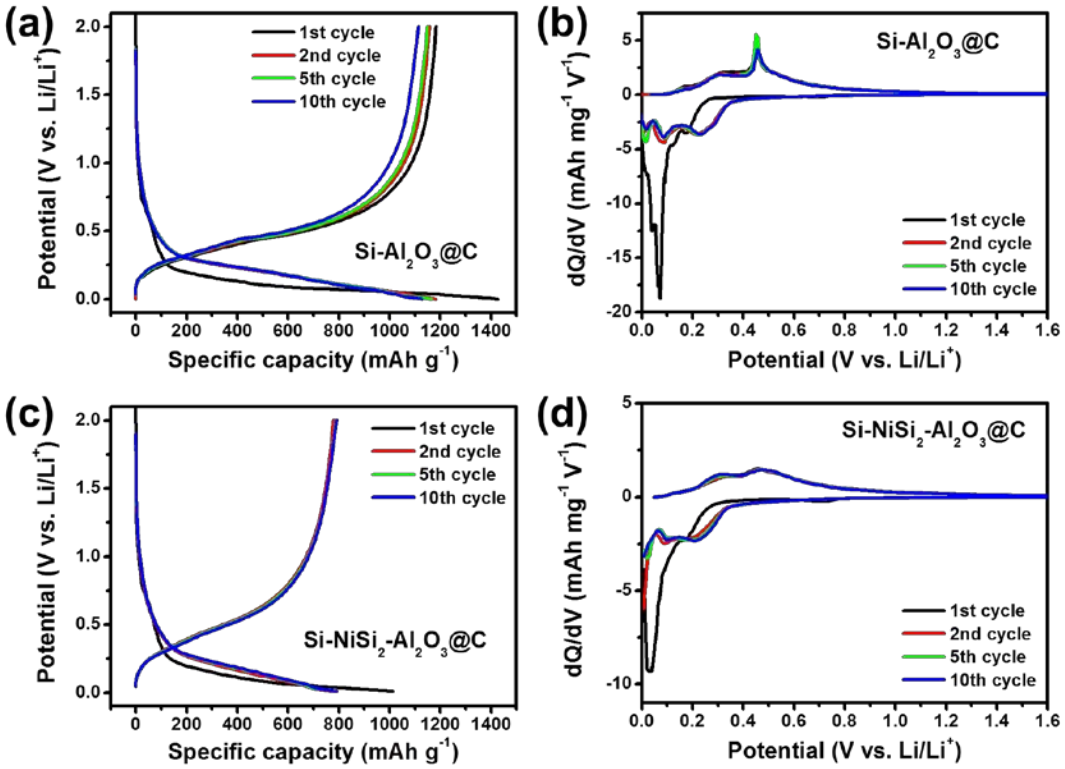

Figure 3.10. Voltage profiles and corresponding differential capacity plots of (a and b) the Si–Al_2O_3@C and (c and d) Si–$NiSi_2$–Al_2O_3@C composite electrodes at a current density of 100 mA g^{-1} in 1 M $LiPF_6$ dissolved in EC/DEC (1 : 1 vol. %) electrolyte.

Table 3.1. Electrochemical data of the silicon-based composite electrodes.

Electrode	Theoretical capacity (mA h g^{-1})	1st charge capacity (mA h g^{-1})	1st discharge capacity (mA h g^{-1})	1st Coulombic efficiency (%)	Capacity retention (n^{th}/1st charge capacity) (%)
Si–Al_2O_3@C	1457	1427	1183	83	43.6 (n = 40)
Si–$NiSi_2$–Al_2O_3@C	978	1020	787	77	89.0 (n = 50)

The DCP data more clearly provide the detailed reaction mechanism of the Si-based composites. Upon the first discharge of the Si–Al_2O_3@C composite (Figure 3.10b), there is a small, insignificant peak appearing at ~ 0.75 V, which is related to the SEI layer formation on the surface of the active material.[83, 98] When the potential reaches ~ 0.25 V, the reaction of lithium with silicon starts to proceed, forming an intermediate binary Li-Si alloy. A remarkable sharp peak is observed below 0.1 V due to the transformation into amorphous Li_xSi in sequence progressing to crystalline $Li_{15}Si_4$ (at ~ 0.05 V) at the end of the discharge process (*i.e.*, fully lithiated state).[99] During the first charge, a broad peak at ~ 0.3 V and a sharp, prominent peak at ~ 0.45 V were observed, which are ascribed to the delithiation reactions from, respectively, amorphous Li_xSi and crystalline $Li_{15}Si_4$.[94-96] In the second discharge, the lithiation processes can be identified with two broad peaks centered at ~ 0.25 and ~ 0.1 V, and a rather sharp peak positioned at ~ 0.01 V. While the broad peaks are indicative of the formation of amorphous Li_xSi and do not show a considerable change, the intensity of the sharp peak related to crystalline $Li_{15}Si_4$ gradually decreases during repeated cycling. This result is consistent with previous studies reporting that crystalline Li_xSi is eventually converted to amorphous form after prolonged cycles.[95] The DCP curves shown in Figure 3.10d illustrate that the lithium alloying and dealloying processes in the Si–$NiSi_2$–Al_2O_3@C composite closely resemble those in the Si–Al_2O_3@C composite. However, it is notable that there is a broad peak at ~ 0.45 V instead of a sharp peak corresponding to the delithiation of crystalline $Li_{15}Si_4$ during the charge process, which is a typical behavior of nanosized silicon or thin-film silicon.[84, 100, 101] This might be attributed to the $NiSi_2$ inclusions in the well-mixed Si/$NiSi_2$ nanostructure that could suppress the formation of crystalline $Li_{15}Si_4$ that causes severe volume expansion.[27]

Figure 3.11a compares the cycle performance of the silicon-based composite electrodes at a current rate of 100 mA g^{-1}. The initial specific charge capacity of the Si–Al_2O_3@C electrode is 1183 mA h g^{-1}, but it continues to decrease with cycling. After 40 cycles, the remaining capacity is 516 mA h g^{-1}, around only 43.6% of its initial capacity. On the other hand, the Si–$NiSi_2$–Al_2O_3@C electrode shows much improved cyclability even after 50 cycles, with a capacity retention of ~ 89%. The enhanced cycle performance might be associated with the presence of highly conductive $NiSi_2$ phase homogeneously mixed with the active silicon nanocrystallites as discussed from the TEM and STEM results, providing better electronic conductivity. In addition, the irreversible SEI layer formation during cycling could be minimized due to the micrometer size of the silicon-based composite and the presence of the electrochemically stable Al_2O_3 matrix.[80] Furthermore, this amorphous Al_2O_3 matrix could prevent the agglomeration of silicon during cycling that can lead to the electrode degradation.

Rate capability tests were also carried out at various current densities from 200 mA g-1 to 3.2 A g^{-1} to examine the influence of the conductive $NiSi_2$ phase on electrochemical properties of the silicon-based composites. As shown in Figure 3.11b, the charge capacities of the Si–Al_2O_3@C electrode are ~ 1140, ~ 1090, and ~ 980 mA h g^{-1}, respectively, at 200, 400, and 800 mA g^{-1}, but capacity drastically decreases to less than 100 mA h g^{-1} at 1.6 A g^{-1}. However, the Si–$NiSi_2$–Al_2O_3@C electrode exhibits stable charge capacities of ~ 790, ~ 785, ~ 780, and ~ 760 mA h g^{-1}, respectively, at 200, 400, 800, and 1600 mA g^{-1}. Moreover, its capacity is maintained over ~ 710 mA h g^{-1} even at a very high current density of 3.2 A g^{-1}, indicating a dramatically improved rate capability. Such an excellent rate performance is attributed not only to the unique nanoscale architecture composed of well-mixed Si/$NiSi_2$ nanocrystallites within amorphous Al_2O_3 and carbon matrix but also to the high electronic conductivity

associated with the $NiSi_2$ inclusions as well as the carbon network that could provide fast Li ion mobility.

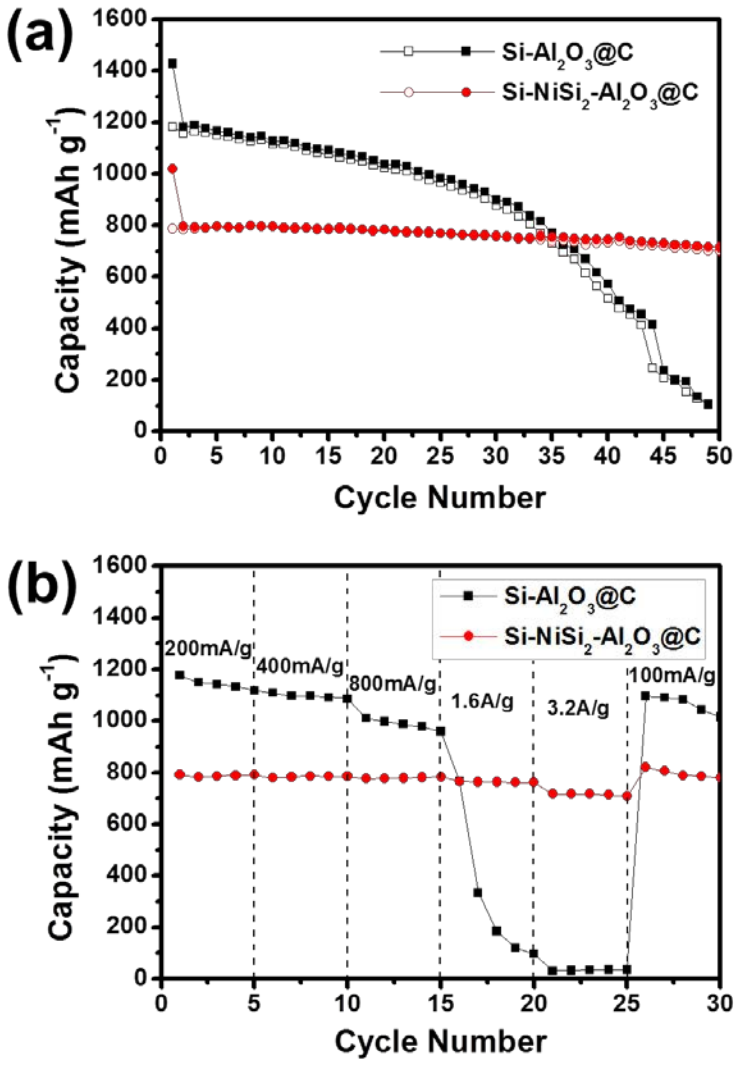

Figure 3.11. Comparison of (a) cycle performance and (b) rate capability of the Si–Al_2O_3@C and Si–$NiSi_2$–Al_2O_3@C composite electrodes. For the rate capability test, the discharge current density was fixed at 100 mA g^{-1}. The typical electrode loading mass of active material was 1.25 ± 0.1 mg cm^{-2}, and all capacity values were calculated based on the total mass of the Si-based composites (including $NiSi_2$, Al_2O_3, and C).

To further check the origin of the enhanced electrochemical properties of the silicon-based composite with $NiSi_2$ phase, the EIS spectra and corresponding electrode surface morphologies at various cycles were investigated and presented in Figure 3.12. The Nyquist plots for both the electrodes (Figure 3.12a and b) are comprised of two depressed semicircles in the high and medium frequency regions and one straight line in the low frequency region. It is generally known that the first and second semicircles directly correlate with, respectively, the interfacial resistance (R_{int}) of the surface of electrode material and the charge transfer resistance (R_{ct}) between the active material and lithium; the linear region is related to the lithium-ion diffusion through the bulk material.[102, 103] The values of each resistance component estimated by curve fitting are summarized in Table 3.2. While the intercept of the first semicircle reflecting electrolyte resistance (R_s) for both the electrodes remains almost the same upon cycling, a significant difference in R_{int} and R_{ct} values could be observed between the two electrodes. Initially, the R_{int} and R_{ct} values of the Si–Al_2O_3@C electrode are 7.5 and 38.6 Ω mg, both of which are similar to those of the Si–$NiSi_2$–Al_2O_3@C electrode (R_{int} = 6.0 Ω mg, R_{ct} = 43.35 Ω mg). After 40 cycles, however, the Si–$NiSi_2$–Al_2O_3@C electrode exhibits much lower resistance values (R_{int} = 54.4 Ω mg, R_{ct} = 135.9 Ω mg) compared to the Si–Al_2O_3@C electrode (R_{int} = 164.9 Ω mg, R_{ct} = 403.9 Ω mg), confirming the multifunctional effects of the $NiSi_2$ phase: (i) providing improved interfacial stability by retarding the abrupt structural changes associated with the formation of crystalline $Li_{15}Si_4$ during cycling and (ii) providing enhanced electronic conductivity. This could also be verified by observing the changes in electrode surface morphology by the *ex situ* SEM images shown in Figure 3.12c and d. While the Si–Al_2O_3@C electrode illustrates severe electrode degradation after 40 cycles, the Si–$NiSi_2$–Al_2O_3@C electrode still shows rather

a smooth surface morphology, demonstrating the effectiveness of the highly conductive $NiSi_2$ phase on the mechanical stability.

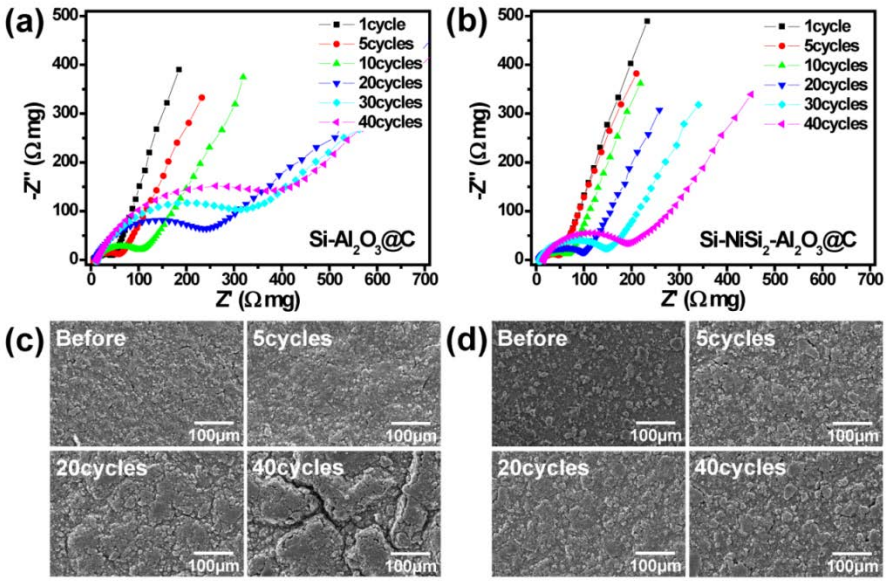

Figure 3.12. Impedance spectra and changes in electrode surface morphologies of the (a and c) Si–Al_2O_3@C and (b and d) Si–$NiSi_2$–Al_2O_3@C composite electrodes as a function of cycle numbers.

Table 3.2. Variations of each resistance component values of the Si-based composite electrodes upon cycling.

Electrode	Component	Resistance (Ω mg)			
		at 1st cycle	at 5th cycle	at 20th cycle	at 40th cycle
Si–Al_2O_3@C	R_s	5.5	6.4	10.1	12.5
	R_{int}	7.5	19.2	127.0	164.9
	R_{ct}	38.6	39.8	151.6	403.9
Si–$NiSi_2$–Al_2O_3@C	R_s	7.1	7.7	6.7	15.5
	R_{int}	6.0	8.8	32.0	54.4
	R_{ct}	43.4	39.9	66.4	135.9

The long-term cyclability and Coulombic efficiency of the silicon-based composite electrodes at a current density of 200 mA g^{-1} are shown in Figure 3.13. The Si–Al_2O_3@C electrode exhibits poor cycle performance with a rapid decrease in Coulombic efficiency after 30 cycles. On the contrary, despite the higher current density, the cycle performance and the first Coulombic efficiency of the Si–$NiSi_2$–Al_2O_3@C composite electrode are comparable to those tested at 100 mA g^{-1} (Figure 3.11a). The first charge capacity is 701 mA h g^{-1}, and the capacity gradually decreases after 50 cycles, maintaining over 78.7% (551 mA h g^{-1}) of its initial capacity after 100 cycles. Moreover, the Coulombic efficiency quickly reaches 99.6 % in the 5th cycle and keeps the value higher than 99.8 % until 100 cycles, confirming the dramatic enhancement of cycle performance. By implementing PAA binder and 30 vol.% FEC-containing electrolyte, which have been considered, respectively, as an effective binder[104, 105] and electrolyte additive[103] for stable SEI formation, the Si–$NiSi_2$–Al_2O_3@C composite electrode exhibits a reversible capacity of ~ 720 mA h g^{-1}, with a capacity retention of 81.5% after 200 cycles. The initial Coulombic efficiency is slightly decreased to ~ 74.3%, which might be a result of the strong binding effect of PAA on the composite particles.[104] Subsequently, the Coulombic efficiency rises to ~ 99.0% after 10 cycles and maintains a very high value of over 99.5% until 200 cycles, demonstrating superior cyclability of the Si–$NiSi_2$–Al_2O_3@C electrode.

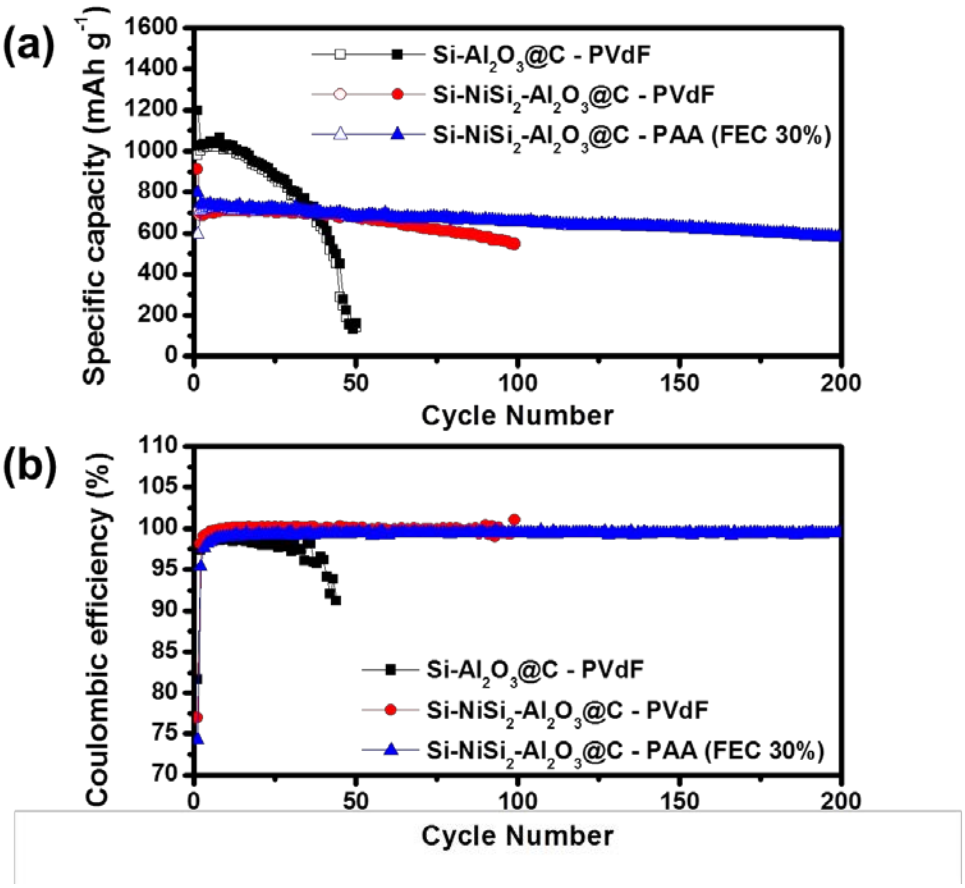

Figure 3.13. (a) Comparison of the long-term cyclability of the Si–Al_2O_3@C and Si–$NiSi_2$–Al_2O_3@C composite electrodes prepared with the conventional PVdF binder in electrolyte without electrolyte additive and Si–$NiSi_2$–Al_2O_3@C composite electrode prepared with PAA binder in electrolyte containing 30 vol. % of FEC as the electrolyte additive. (b) Variation of the Coulombic efficiency of the Si–Al_2O_3@C and Si–$NiSi_2$–Al_2O_3@C composite electrodes. The typical electrode loading of active material was 1.65 ± 0.1 mg cm^{-2} when PAA binder was used. Note that all the capacity values were calculated based on the total mass of the Si-based composites (including $NiSi_2$, Al_2O_3, and C).

In terms of the feasibility of commercial implementation, significant consideration should be given to the possibility of high packing density that could lead to high volumetric capacity.[84, 85] The tap density of the Si–$NiSi_2$–Al_2O_3@C composite was

measured to be ~ 1.34 g cm^{-3}, which is higher than that of the Si–Al_2O_3@C composite (~ 0.95 g cm^{-3}) due to the higher density of $NiSi_2$ (~ 4.83 g cm^{-3}) compared to that of silicon (~ 2.33 g cm^{-3}). Besides, the Si–$NiSi_2$–Al_2O_3@C composite has about two times higher tap density compared to the micrometer-size silicon-based materials recently studied as shown in Table 3.3. To the best of our knowledge, such a high tap density has been rarely reported for silicon-based materials.[106] When considering high electrode loading mass of ~ 1.65 mg cm^{-2}, the Si–$NiSi_2$–Al_2O_3@C composite exhibits an areal capacity of as high as ~ 1.2 mA h cm^{-2} in the first few cycles and ~ 0.96 mA h cm^{-2} even after 200 cycles, which is comparable to micro-sized Si-C composite (0.96 mA h cm^{-2}),[85] despite the relatively lower specific capacity.

Table 3.3. Comparison of the tap densities, specific capacities, volumetric capacities, and areal capacities of several silicon-based materials. Calculations were made by assuming that the composite electrodes could be prepared with the measured tap density.

Electrode	Tap density (g cm^{-3})	Specific capacity (mA h g^{-1})	Volumetric capacity (mA h cm^{-3})	Areal capacity (mA h cm^{-2})
Nano Si[84]	0.16	1200	192	-
Milled Si[84]	0.70	1200	840	0.84
Si-C composite[85]	0.68	1600	1088	0.96
Si–$NiSi_2$–Al_2O_3@C	1.34	720	965	1.2

3.4. CONCLUSION

In conclusion, we have developed a highly practical silicon-based composite anode material and demonstrated excellent performance in terms of reversible specific capacity, cyclability, and rate capability. Carbon-coated micron-sized particles that consist of aggregated nanostructured building blocks with uniform dispersion of well-mixed Si/$NiSi_2$ nanocrystallites within the amorphous Al_2O_3 matrix were synthesized by a facile, low-cost, environmentally benign synthesis method with high yield. The Si–$NiSi_2$–Al_2O_3@C electrode exhibits a high reversible capacity of ~ 720 mA h g^{-1} with a good capacity retention of 81.5% after 200 cycles. Such a high performance of the Si–$NiSi_2$–Al_2O_3@C electrode is attributed to the combination of the multifunctional conductive $NiSi_2$ nanoinclusions and electrochemically stable Al_2O_3 buffer matrix. With a high tap density and a high loading mass, high volumetric and areal capacities of, respectively, ~ 965 mA h cm^{-3} and ~ 1.2 mA h cm^{-2} could also be obtained. Although further improvement is still needed to overcome the low Coulombic efficiency and achieve higher areal capacity without deteriorating cyclability for commercial implementation, it is remarkable that the Si–$NiSi_2$–Al_2O_3@C composite shows a great potential to be realized as a high-performance anode for lithium-ion batteries.

Chapter 4: Low-Cost Carbon-Coated Si-Cu_3Si-Al_2O_3 Nanocomposite Anodes for High-Performance Lithium-Ion Batteries

4.1. INTRODUCTION

In Chapter 3, we showed that the incorporation of nano-sized silicon into a multiphase buffer composed of conductive $NiSi_2$ and electrochemically inert Al_2O_3 by the low-cost HEMM process could provide enhanced powder conductivity, high electrochemical stability, and strong structure-reinforcing effects, while maintaining a reasonably high tap density (> 1.2 mg cm^{-3}). As a result, the silicon-based composite exhibited improvement in the electrochemical reversibility, volumetric and areal capacities, as well as cycling and rate performance, demonstrating the effectiveness of the multifunctional inactive matrices. For practical application, however, the real electrochemical properties need to be further investigated by fabricating a full lithium-ion cell. In addition, the use of nickel is less favorable in composite strategy because of the high cost of nickel precursor.[13]

Herein, we report a low-cost, facile HEMM approach for synthesizing a carbon-coated silicon-based composite with a combined inactive buffer phase including both crystalline Cu_3Si and amorphous Al_2O_3 and significantly enhanced electrochemical characteristics as an anode material for lithium-ion batteries. The as-synthesized composite particles have well-intermixed nanostructure with a few microns in size, giving a reasonably high tap density of > 1.0 g cm^{-3}. The introduction of low-cost copper precursor induces the formation of highly conductive Cu_3Si phase, which has good mechanical flexibility and high electronic conductivity,[107] thereby effectively accommodating the large volume change of silicon active particles as well as offering improved conductivity with the composite particles. Moreover, the presence of amorphous Al_2O_3 plays an important role in endowing enhanced interfacial stability

during cycling. Furthermore, carbon coating ensures the formation of stable SEI and reduction in interparticle resistance. The synergistic effects derived from the multiphase inactive buffer matrix result in superior electrochemical performance in both half cells and full cells, making it a desirable anode candidate for high-performance lithium-ion batteries.

4.2. EXPERIMENTAL

4.2.1. Sample Preparation

The carbon-coated silicon-based composites with Cu3Si buffer phase were prepared via a two-step HEMM with a SPEX 8000M apparatus. Commercial silicon monoxide (SiO , –325 mesh, Aldrich), aluminum (99%, 17–30 μm, Alfa Aesar), copper (99%, 45 μm, Acros Organics), and graphite (CGP–G8, Conoco) were used as raw materials without further purification. Stoichiometric amounts of SiO and aluminum (molar ratio of 6 : 4) were mixed with different amounts of elemental copper powder (x = 0.33, 0.66, and 1.0 in reaction (4.1) below) and sealed in a hardened stainless steel vial (80 cm^3) with hardened steel balls under argon atmosphere. Then, the HEMM was conducted for 8 h at room temperature to obtain the silicon-based composites with Cu_3Si. The mechanochemical reaction occurring during the first HEMM process can be described as shown below in reaction (1):

$$6\ SiO + 4\ Al + 3x\ Cu \rightarrow (6 - x)\ Si + x\ Cu_3Si + 2\ Al_2O_3 \qquad (4.1)$$

The composite powders were further mixed with 10 wt. % of graphite and milled for 15 min under argon atmosphere to obtain the carbon-coated silicon-based composites with different Si/Cu_3Si ratios (Si : Cu_3Si = 18 : 0, 17 : 1, 16 : 2, and 15 : 3, respectively, for x = 0, 0.33, 0.66, and 1.0 in reaction (1) above). For a comparison, the carbon-coated

silicon-based composite without Cu_3Si was also synthesized under the same condition without the addition of elemental copper.

4.2.2. Sample Characterization

The microstructure, chemical states, and particle morphology of the carbon-coated silicon-based composites were characterized with a Rigaku X-ray diffractometer (MiniFlex 600) with Cu Kα (λ = 1.54059 Å) radiation, a Kratos X-ray photoelectron spectrometer, scanning electron microscopy equipped with energy dispersive X-ray spectroscopy (SEM-EDS, JEOL JSM–5610), high resolution transmission electron microscopy (HRTEM, JEOL 2010F), and scanning transmission electron microscopy (STEM, Hitachi S–5500). A Quantachrome AT–4 Autotap machine was utilized to measure the tap density of the composite samples.

4.2.3. Electrochemical Measurements

The test electrodes were prepared by the doctor-blade method. Slurries containing active material, Super P conductive carbon, and poly(acrylic) acid (PAA) binder (70 : 15 : 15 wt.%) were coated onto copper foil current collectors and dried in a vacuum oven at 120 ^{o}C for 8 h. The disk electrodes (diameter of 1.2 cm) with a typical loading of 1.5 ~ 2.0 mg cm^{-2} were used to assemble the CR2032 type coin cells with a polypropylene (Celgard 2500) separator and a lithium metal reference/counter electrode. The electrolyte used was 1 M $LiPF_6$ dissolved in ethylene carbonate (EC) / diethyl carbonate (DEC) mixture (1 : 1 by vol.) containing fluoroethylene carbonate (FEC) additive (5 vol. %). The charge-discharge experiments were carried out with an Arbin BT2000 battery tester within the voltage range of 0.0 – 2.0 V (vs. Li / Li^+) at various current densities for half-cell tests. Commercial spinel manganese oxide cathode was used for full-cell tests, and the cells were cycled within a cut-off voltage of between 2.5 and 4.3 V (vs. Li / Li^+), An

impedance/gain-phase analyzer (Solartron SI 1260) equipped with an electrochemical interface (Solartron SI 1286) was used to perform the electrochemical impedance spectroscopy (EIS) with an ac amplitude of 5 mV over the frequency range of 100 kHz to 0.1 Hz.

4.3. RESULTS AND DISCUSSION

4.3.1. Structure and Morphology

The XRD patterns of the carbon-coated silicon-based composites without and with various amounts of the Cu_3Si phase are presented in Figure 4.1. The sample without the Cu_3Si phase shows only the characteristic peaks of crystalline silicon (JCPDS No. 77-2110, cubic, S.G. = Fd-3m, a = 5.4298 Å) without any of the diffraction peaks of metallic aluminum, suggesting that SiO is completely reduced to silicon during HEMM for 8 h due to the high reducing power of aluminum. When copper was added during the HEMM process, the composites display three additional peaks at ~ 44.6, ~ 45.1, and ~ 65.4^o along with the silicon peaks, which can be indexed to crystalline copper silicide (Cu_3Si, JCPDS No. 59-0262, hexagonal, space group: P-*3m1*) phase. These newly generated peaks become dominant as the amount of copper increases, while the intensity of the silicon peaks decreases. This may be due to both the decreasing amount of elemental silicon and a reduction in the crystallite size of silicon due to the Cu_3Si inclusion during ball milling. No peaks related to graphite are observed, possibly due to the structural damage imposed by HEMM. In addition, the absence of the Al_2O_3 peaks suggests the presence of amorphous Al_2O_3 in the composites. This is verified by the XPS measurement of the carbon-coated silicon-based composites (Figure 4.2). In the Al 2p spectra (Figure 4.2a), all the composite samples show the Al 2p peak located at ~ 75.2 eV, which is obviously at a higher binding energy than that of metallic aluminum (~ 72.7 eV), originating from

the Al 2p signal in amorphous Al_2O_3 due to a higher oxidation state of aluminum.[89] Moreover, the O 1s peak at ~ 532.1 eV can be found for all the composite samples (Figure 4.2b), further indicating the formation of amorphous Al_2O_3 during ball milling.[108] Therefore, it can be concluded from the combined XRD and XPS analyses that the crystalline silicon, Cu_3Si, and amorphous Al_2O_3 are the major components of the silicon-based composites prepared with copper addition.

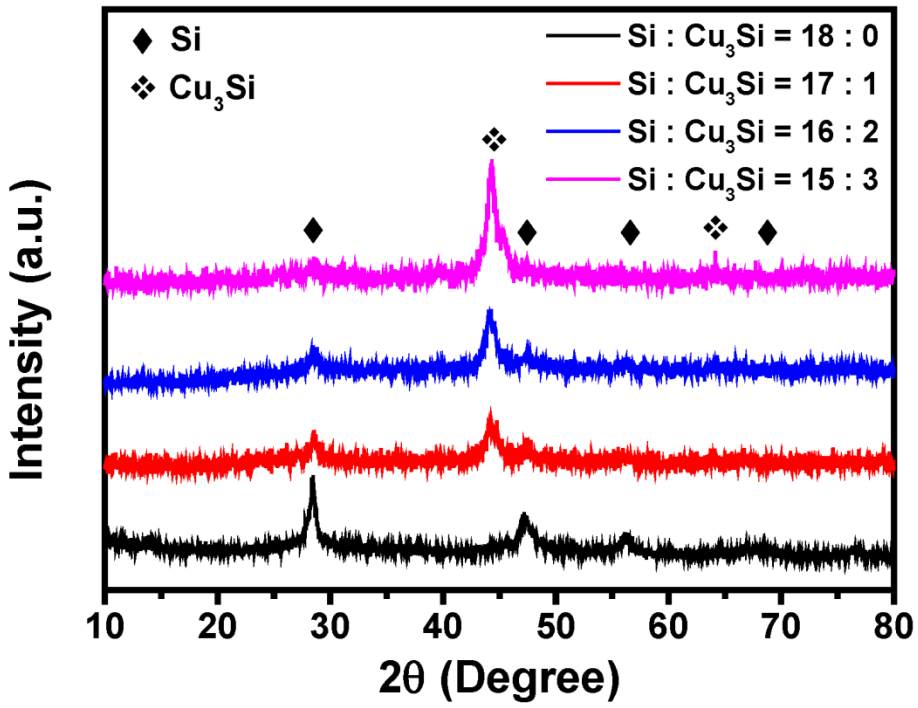

Figure 4.1. XRD patterns of the carbon-coated silicon-based composites with and without conductive Cu_3Si.

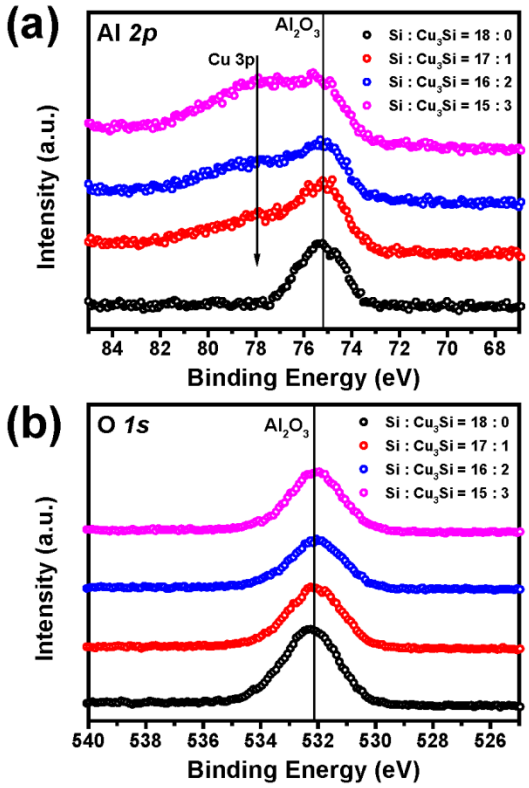

Figure 4.2. Comparison of the XPS spectra of (a) Al 2p and (b) O 1s regions of the carbon-coated silicon-based composites with and without the conductive Cu_3Si.

The SEM micrographs of the composite samples (Si : Cu_3Si = 18 : 0, 17 : 1, 16 : 2, and 15 : 3) depicted in Figure 4.3 indicate that all the powders have a similar particle morphology regardless of the copper content with an average secondary particle size of < 10 μm. The formation of micro-sized composite secondary particles could lead to an increase in the tap density of bulk powder, making it possible to achieve high volumetric and areal capacities that are key parameters for commercial implementation.[86, 109] The tap densities of the composite samples were measured to be ~ 0.95, 1.08, 1.11, and 1.18, respectively, for the Si : Cu_3Si = 18 : 0, 17 : 1, 16 : 2, and 15 : 3 samples, which are

similar to or even higher than that of graphite (~ 1.0 g cm^{-3}).[75] The approximate amounts of each component in the composite samples were also estimated by the EDS analysis (Figure 4.4), and the results show that the amounts of silicon, Cu_3Si, and amorphous Al_2O_3 are almost the same as those calculated based on reaction (4.1).

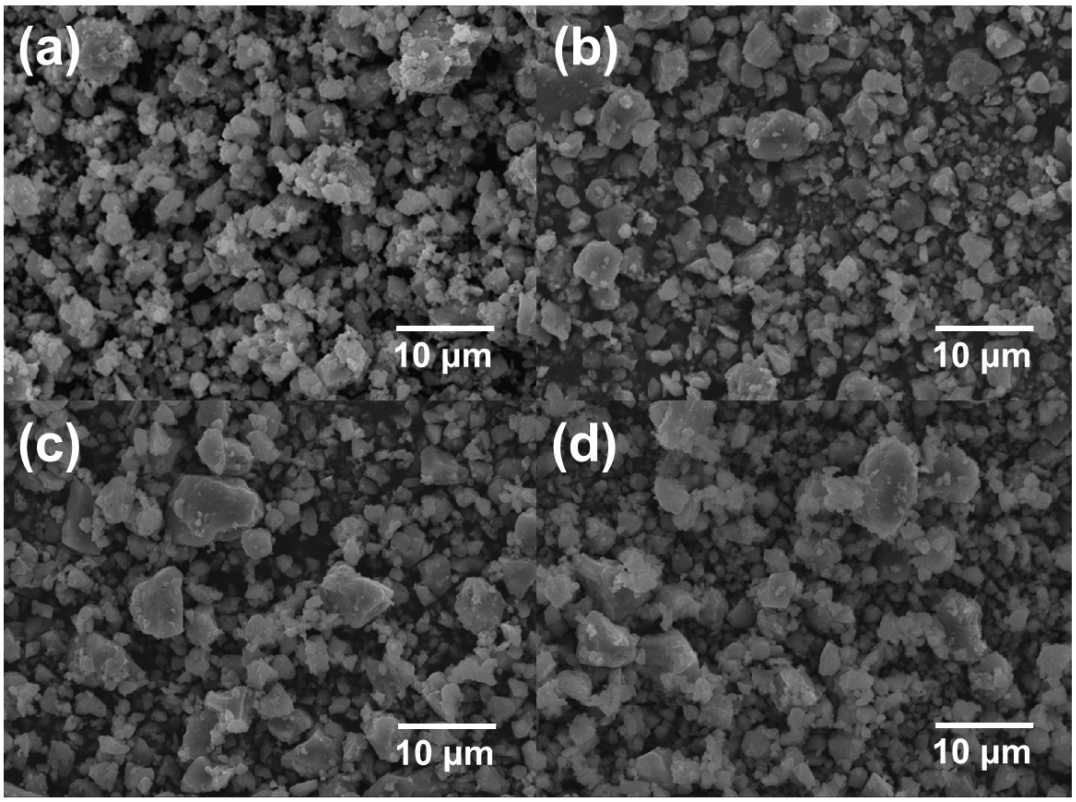

Figure 4.3. SEM micrographs of the carbon-coated silicon-based composite powders with (a) Si : Cu_3Si = 18 : 0, (b) Si : Cu_3Si = 17 : 1, (c) Si : Cu_3Si = 16 : 2, and (d) Si : Cu_3Si = 15 : 3.

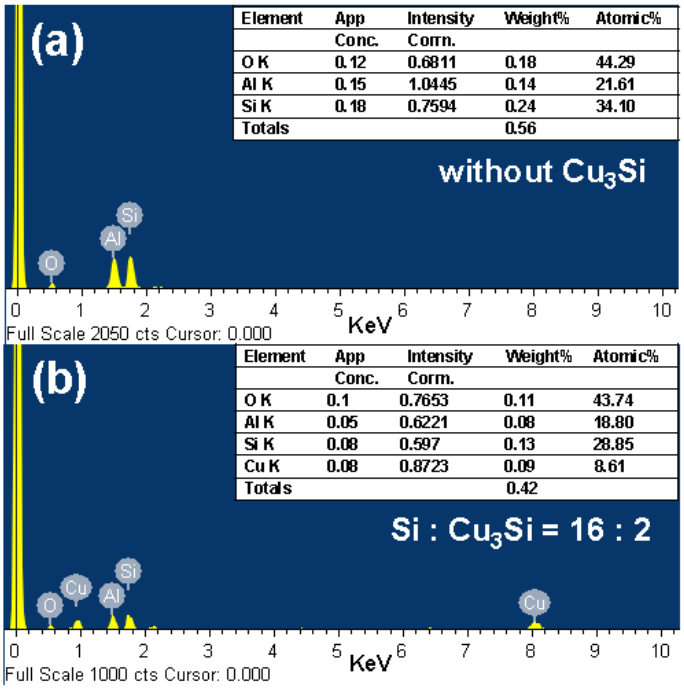

Figure 4.4. SEM/EDS results of the carbon-coated silicon-based composites with (a) Si : Cu_3Si = 18 : 0 and (b) Si : Cu_3Si = 16 : 2.

It should be noted that the composite particles synthesized by HEMM, which undergo continuous structural deformation and reconstruction caused by the mechanical stresses induced by the milling process,[110] generally exhibit nanostructured morphology consisting of aggregated nanoclusters containing multiple phases, giving rise to enhanced electrochemical performance with the composite materials. In order to observe the microstructure of the composites in more detail, TEM was employed for the silicon-based composites with Si : Cu_3Si = 18 : 0 and 16 : 2. Both samples have the carbon coating layers generated as a result of the second milling step with graphite (Figure 4.5a and Figure 4.6), which is expected to improve the powder conductivity. However, while the sample without Cu_3Si shows only one interplanar spacing of ~ 0.313 nm (Figure 4.6),

corresponding to the (111) plane of crystalline silicon, there are lattice fringes with two different interplanar spacings that can be identified to be the (111) plane of crystalline silicon (d = ~ 0.313nm) as well as the (103) plane of Cu_3Si for the sample with Si : Cu_3Si = 16 : 2 as shown in Figure 4.5b, confirming the presence of both crystalline silicon and Cu_3Si in the composite with the addition of copper. Besides, each phase (silicon, Cu_3Si, and Al_2O_3) is homogeneously incorporated within the composite particle, as evident from the STEM and corresponding EDS mapping images presented in Figure 4.5c. It can be also seen that carbon is mainly distributed on the surface of the particle, which is in accordance with the TEM results described above.

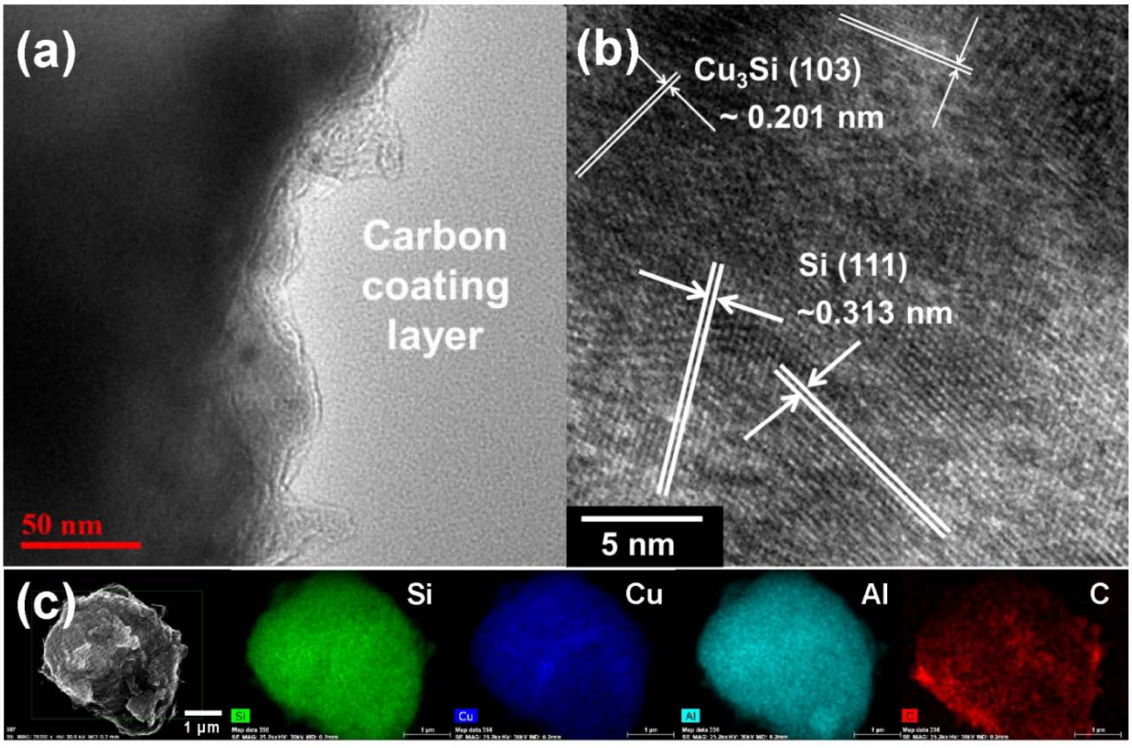

Figure 4.5. (a) TEM, (b) HR-TEM, and (c) STEM images of the carbon-coated silicon-based composite with Cu_3Si (Si : Cu_3Si = 16 : 2). In STEM, the EDS mapping images of each element are indicated (silicon: green, copper: blue, aluminum: cyan, and carbon: red).

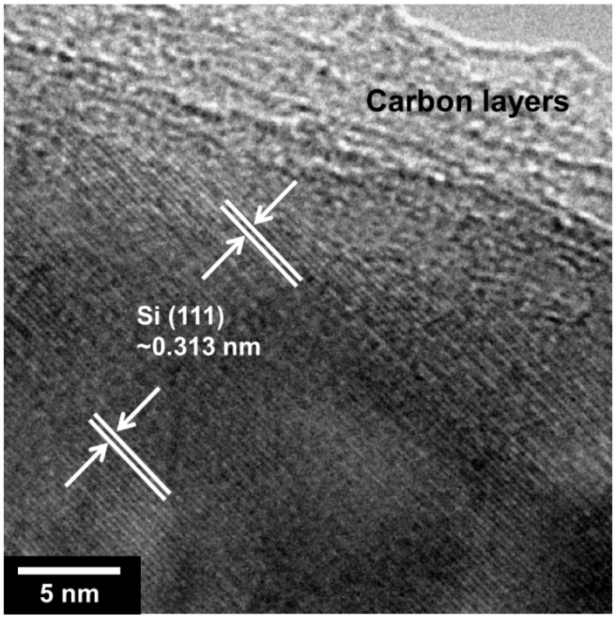

Figure 4.6. HR-TEM image of the carbon-coated silicon-based composite without Cu_3Si.

4.3.2. Electrochemical Characterization

Half-cell cycling tests were performed with the carbon-coated silicon-based composites to investigate the anode performance in lithium-ion batteries. Figure 4.7a shows the charge-discharge profiles tested at a constant current density of 100 mA g^{-1} between 0.0 and 2.0 V (vs. Li / Li^+). During the first cycle, all the composite electrodes seem to exhibit sloping profiles upon discharge (lithiation) and following charge (delithiation) reactions. The first charge (delithiation) capacities of the samples were ~ 1180, 1083, 841, and 615 mA h g^{-1}, respectively, for the Si : Cu_3Si = 18 : 0, 17 : 1, 16 : 2, and 15 : 3 samples. The decrease in the specific capacity values is due to the decreasing amount of electrochemically active silicon phase in the composites as can be seen in the EDS results (Figure 4.4). In addition, the initial Coulombic efficiencies diminish with the

increase in the Cu_3Si content, from ~ 83 % for the sample without Cu_3Si to ~ 66 % for the Si : Cu_3Si = 15 : 3 sample. However, the composite samples with a higher amount of copper addition (Si : Cu_3Si = 16 : 2 and 15 : 3) have much better electrochemical reversibility and cyclability as evident from the well overlapped voltage profiles up to 10 cycles, suggesting that the introduction of Cu_3Si phase provides enhanced ionic or electronic conductivity and mechanical buffering effects against volume change during cycling. Specifically, the sample with Cu_3Si (Si : Cu_3Si = 16 : 2) exhibit more than double the specific capacity of graphite with reasonably high initial Coulombic efficiency of ~ 76 % and improved capacity retention compared to the composite without Cu_3Si.

In order to understand the detailed reaction mechanism, the differential capacity plots (DCPs) at initial two cycles for the composite electrodes are presented in Figure 4.7b. The sample without Cu_3Si shows a broad peak within the voltage range of 0 – 0.2 V with a sharp peak centered at ~ 0.1 V upon first discharge, which are attributed to the lithiation reactions into silicon, eventually forming a crystalline $Li_{15}Si_4$ binary alloy.[15, 99] During the first charge, a broad peak located in the voltage range of 0.3 – 0.8 V is seen along with a sharp peak centered at ~ 0.45 V, arising from the delithiation processes of, respectively, amorphous Li_xSi and crystalline $Li_{15}Si_4$.[94] In the subsequent discharge, DCP curve becomes broadened and no sharp peaks can be observed, indicating the formation of amorphous silicon after the initial cycling. In contrast, in the cases of the composites with Cu_3Si, the lithiation and delithiation reaction peaks during the first discharge are much broader compared to the composite without Cu_3Si, possibly due to the reduced crystallite size of silicon. In addition, the sharp peak at ~ 0.45 V occurring upon charge disappears, suggesting that silicon cannot be converted to the fully lithiated phase ($Li_{15}Si_4$) even at the end of discharge when Cu_3Si is present in the composites. This is beneficial for improving the electrochemical performance of silicon anode since the

formation of crystalline $Li_{15}Si_4$ during cycling results in severe volume expansion, consequently leading to the pulverization of the electroactive materials and mechanical degradation of the electrodes.

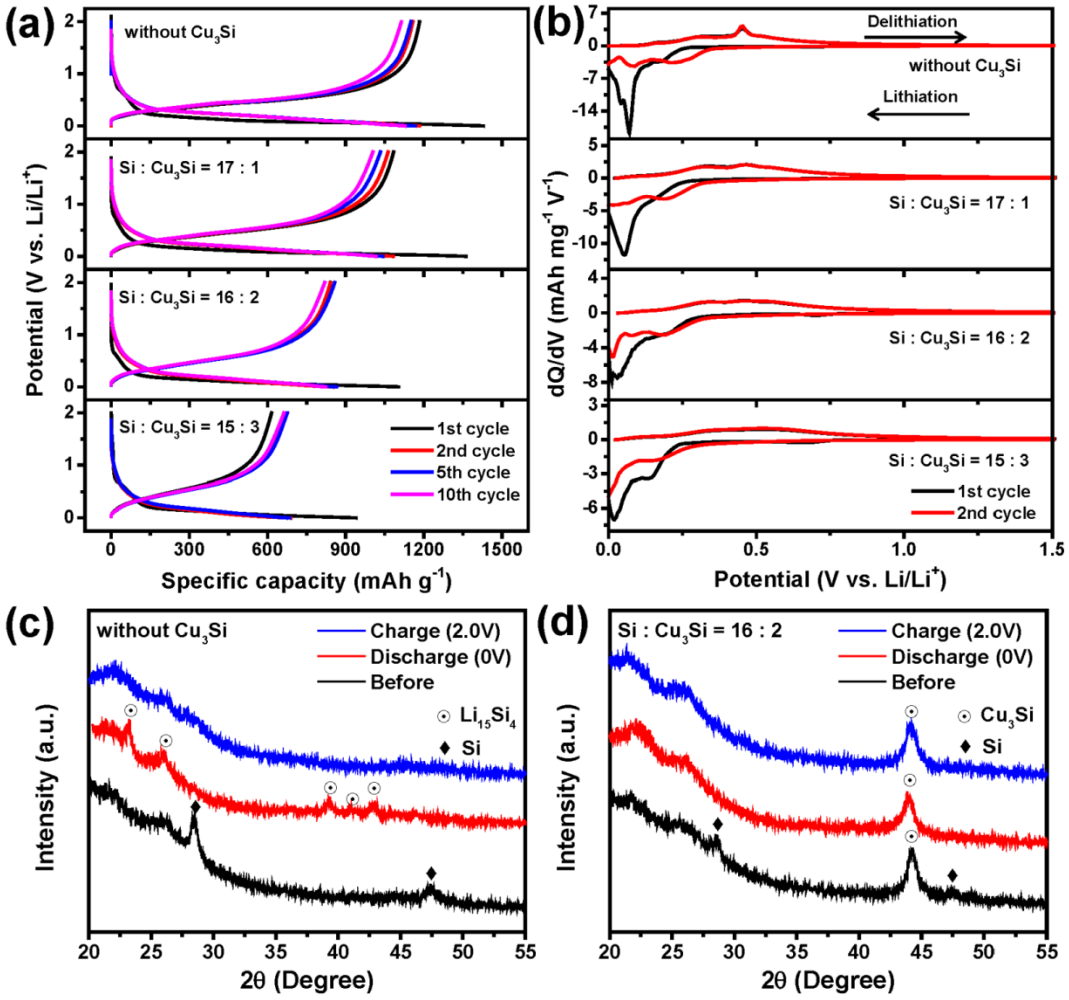

Figure 4.7. (a) Voltage profiles and (b) differential capacity plots of the carbon-coated silicon-based composite at various cycles tested within the voltage window of 0.0 – 2.0 V (vs. Li / Li^+) at a current density of 100 mA g^{-1}. The *ex situ* XRD patterns at various states of charge of the composites with (c) Si : Cu_3Si = 18 : 0 and (d) Si : Cu_3Si = 16 : 2.

To confirm the phase changes and structural evolutions of the composites with and without Cu_3Si during the initial cycles, *ex situ* XRD analyses were further carried out on the samples without and with Cu_3Si (Si : Cu_3Si = 16 : 2) at fully discharged (0 V vs. Li / Li^+) and fully charged (2.0 V vs. Li / Li^+) states. Figure 4.7c shows that the sample without Cu_3Si has only crystalline silicon peaks before cycling. These peaks are no longer detected and several diffraction peaks corresponding to $Li_{15}Si_4$ appear at the end of discharge (0 V). When charged to 2 V, there are no observable peaks in the XRD pattern, demonstrating that amorphous silicon is formed upon charging. These observations are in good agreement with the aforementioned DCP analysis. In the case of the composite with Cu_3Si (Si : Cu_3Si = 16 : 2) (Figure 4.7d), however, the characteristic peaks of $Li_{15}Si_4$ are not observed even at full lithiation (0 V) and the Cu_3Si peaks remain unchanged during cycling. This further demonstrates that the presence of Cu_3Si suppresses the formation of $Li_{15}Si_4$ due to the buffering effect against volume change, eventually enhancing the cycling stability of silicon anode.

The cyclability of the carbon-coated silicon-based composites tested at a current density of 200 mA g^{-1} is illustrated in Figure 4.8a. The composite without Cu_3Si shows poor cycle performance compared to the samples containing Cu_3Si due to the low powder conductivity, large structural changes, and mechanical stress induced by the $Li_{15}Si_4$ formation during cycling. The reversible capacity gradually decreases with cycling and the composite retains only ~ 53% of the initial capacity after 200 cycles. On the other hand, the cyclabilities of the composites with Cu_3Si become improved with the increase in the Cu_3Si content in the composites. The best performance is obtained for the sample with Cu_3Si (Si : Cu_3Si = 16 : 2) in terms of the reversible capacity, initial Coulombic efficiency, and capacity retention. It delivers a first reversible capacity of 841 mA h g^{-1} with a reasonably high initial Coulombic efficiency of ~ 76 % and maintains the capacity

over 704 mA h g^{-1} even after 200 cycles, which is > 83.7% of its initial capacity. The rate performance of the carbon-coated silicon-based composites was also compared at various current densities of 200 mA g^{-1} to 3.2 A g^{-1} (Figure 4.8b). While the sample without Cu_3Si shows the highest reversible capacity of ~ 1176 mA h g^{-1} at 200 mA g^{-1}, a severe capacity drop is observed at a current density of as high as 1.6 A g^{-1} and it only delivers a charge capacity of ~ 320 mA h g^{-1} at 3.2 A g^{-1}, indicating the low rate capability of the composite without Cu_3Si. However, the charge capacities of the sample with Cu_3Si (Si : Cu_3Si = 16 : 2) are ~ 840, 820, 810, 800, and 780 mA h g^{-1}, respectively, at current densities of 200, 400, 800, 1600, and 3200 mA g^{-1}, demonstrating the remarkably enhanced rate performance of the composite with Cu_3Si (Si : Cu_3Si = 16 : 2). When the current density is decreased back to 200 mA g^{-1}, it still exhibits a reversible capacity of ~ 830 mA h g^{-1}, indicating that nearly 100 % of capacity can be restored.

The significant enhancement in cycle and rate performances is primarily achieved by the successful formation of Cu_3Si that could improve the structural stability and provide high ionic/electronic conductivity. Besides, the incorporation of nanosized silicon particles into the amorphous Al_2O_3 buffer matrix, which is electrochemically stable and inactive toward lithium, leads to an improved stability of the interfaces between the composite particles and the electrolyte. The carbon coating layers further endows high conductivity and prevents silicon particles from generating unstable SEI on the surface of the composite materials. Therefore, the realization of the nanostructured composite with multifunctional phases leads to an accommodation of the large volume changes of the active materials and prevents mechanical failure of the electrodes by restraining the formation of the $Li_{15}Si_4$ phase, enhancing the ionic transport during cycling by providing the short diffusion pathways for lithium ions and imparting high chemical and electrochemical stability during repeated cycling. Furthermore, the

enhanced conductivity of the composites with Cu_3Si could be confirmed by the EIS studies (Figure 4.9). Although the samples without and with Cu_3Si (Si : Cu_3Si = 16 : 2) exhibit similar charge-transfer resistances (the diameter of the semicircle) after 10 cycles, the composite with Cu_3Si (Si : Cu_3Si = 16 : 2) shows a much lower charge-transfer resistance after 200 cycles, compared to the composite without Cu_3Si. This further supports that the Cu_3Si addition helps maintaining a high conductivity of the composite particles over electrochemical cycling.

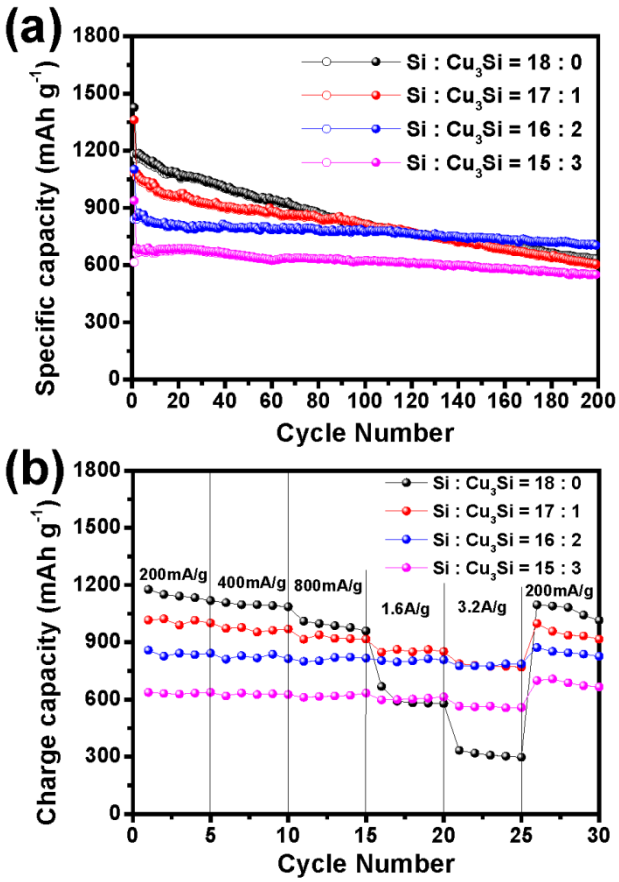

Figure 4.8. Comparison of the (a) cycle performance and (b) rate capability of the carbon-coated silicon-based composites with and without conductive Cu_3Si. The specific capacity was calculated based on the total mass of the composite materials.

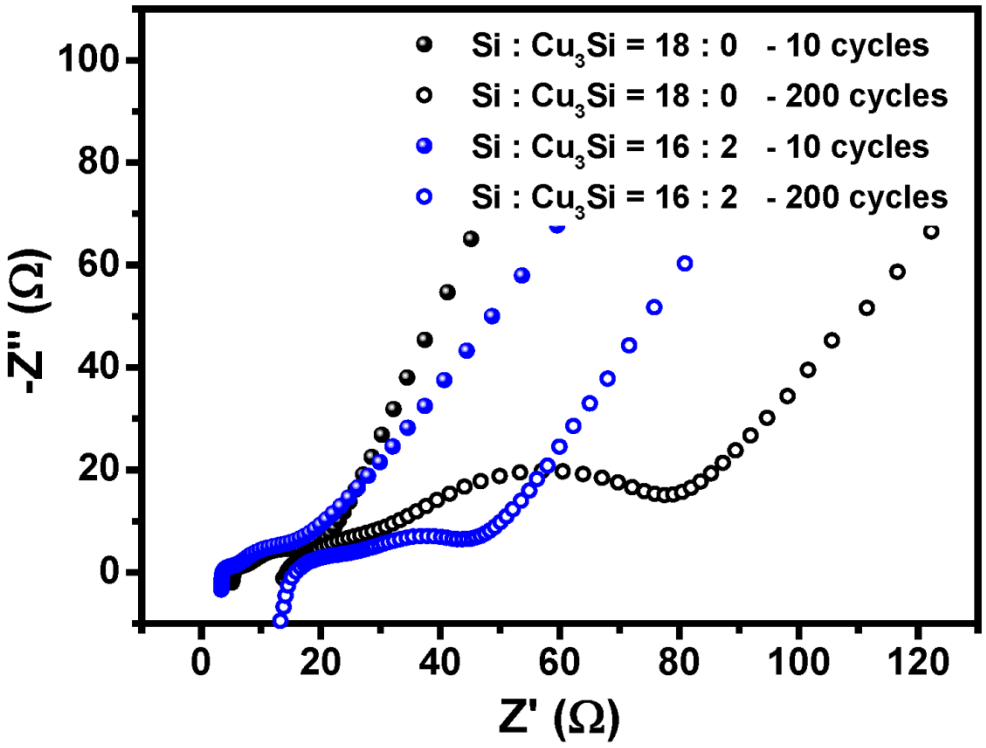

Figure 4.9. Comparison of the Nyquist plots for the carbon-coated silicon-based composites without and with Cu_3Si (Si : Cu_3Si = 16 : 2) after 10 and 200 cycles.

Full-cell performance was also assessed by assembling CR2032 coin cells with the carbon-coated silicon-based composite anode (Si : Cu_3Si = 16 : 2) and a commercial spinel lithium manganese oxide ($LiMn_2O_4$) cathode. The spinel cathode shows a reversible capacity of ~ 100 mA h g^{-1} with stable cyclability in a half cell test (Figure 4.10). For the full-cell test, the ratio of the anode and cathode capacities (N/P ratio) was adjusted at ~ 1.2 and the cells were tested at a current density of 12 mA g^{-1} for initial five formation cycles and then cycled at 60 mA g^{-1} (equivalent to 0.5C rate based on the mass of the cathode material) between the cut-off potentials of 2.5 – 4.3 V (vs. Li/Li^+). Before the full cell operation, the pre-lithiation process was conducted for the composite anode,

which is known as a simple and effective method to compensate for the first cycle irreversible capacity loss of the electrode materials.[22, 111, 112] In this study, the composite anode was electrochemically discharged to 0.2 V in a lithium half-cell and reassembled with the spinel cathode. The voltage profiles in Figure 4.11a show two sloping regions in the range of 3.7 – 4.2 V upon discharging and 3.3 – 3.9 V during charging, indicating that the average voltage of the spinel lithium manganese oxide / partially-lithiated silicon composite cell is comparable to that of commercial $LiCoO_2$ / graphite cell (~ 3.6 V). The reversible capacity was as high as ~ 95 mA h g^{-1} (based on the mass of the cathode material), which is > 95% of its capacity delivered in a lithium half cell, with a high initial Coulombic efficiency of ~ 86.3 %. In addition, the full-cell exhibits relatively good capacity retention of ~ 77.2 % as shown in Figure 4.11b, delivering a reversible capacity of ~ 70 mA h g^{-1} after 50 cycles even at a high current density of 60 mA g^{-1} (0.5 C). These reasonably good electrochemical characteristics in the real full-cell configuration demonstrate that the carbon-coated silicon-based composite can be regarded as a promising anode for high-performance lithium-ion batteries.

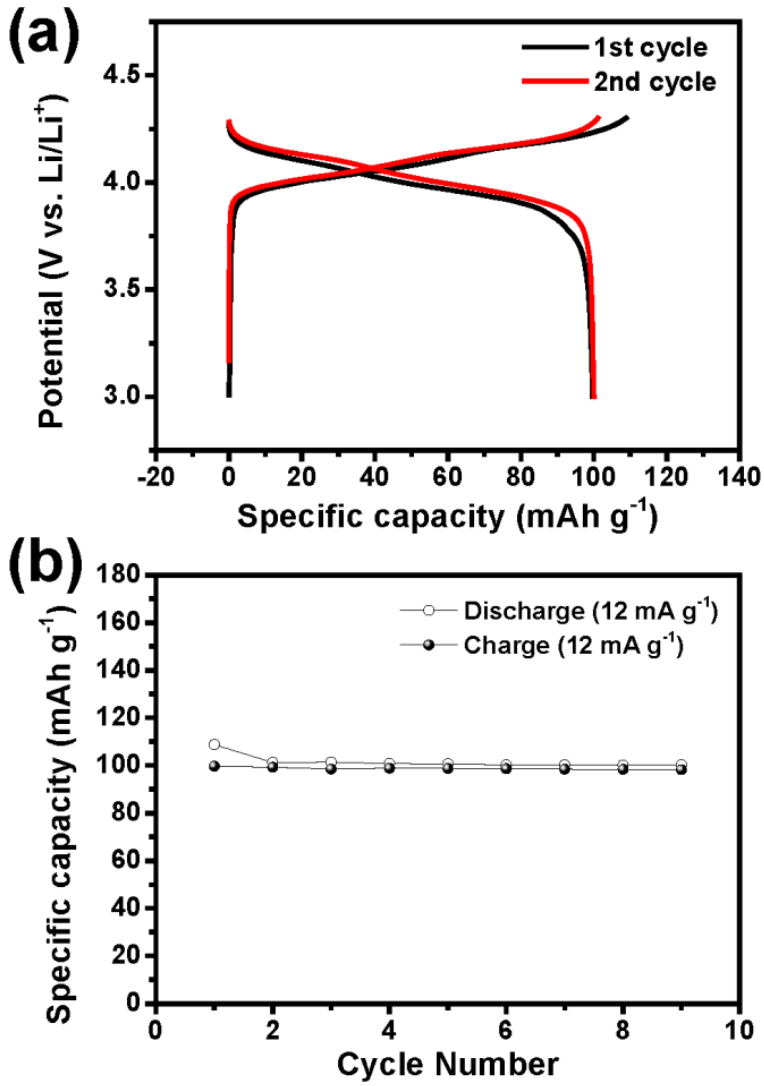

Figure 4.10. Voltage profiles and (b) cycle performance of the spinel lithium manganese oxide cathode tested within a voltage window of 3.0 – 4.3 V (vs. Li / Li^+). The specific capacity was calculated based on the mass of the cathode material.

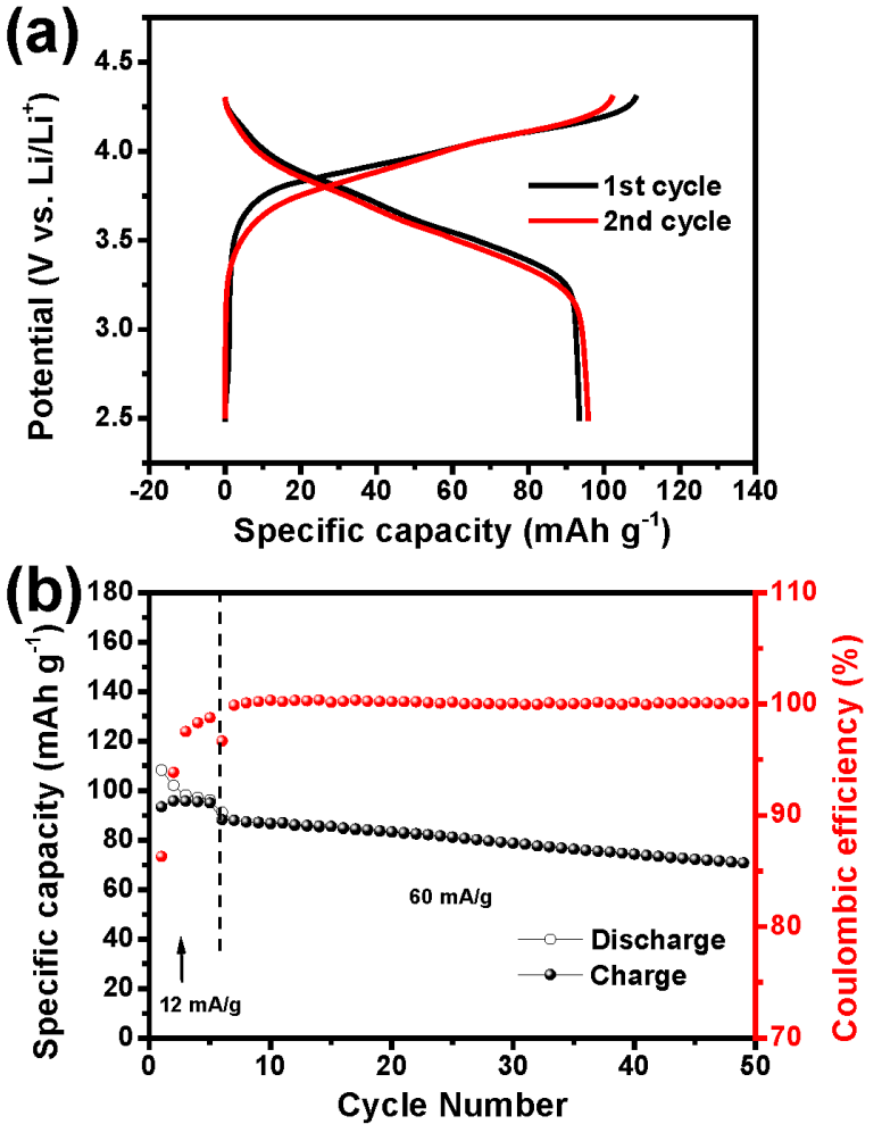

Figure 4.11. (a) Voltage profiles at initial two cycles and (b) cycle performance of the spinel lithium manganese oxide / partially-lithiated silicon composite (x= 0.66) full cell tested within a voltage window of 2.5 – 4.3 V (vs. Li / Li^+). The specific capacity was calculated based on the mass of the cathode material.

4.4. CONCLUSION

Carbon-coated silicon-based composites with a conductive Cu_3Si phase have been prepared by a facile, low-cost, environmentally benign HEMM process and demonstrated as a potential anode for lithium-ion batteries. The realization of the unique carbon-coated composite nanostructure composed of multifunctional phases including active silicon, conductive Cu_3Si, and highly stable Al_2O_3 leads to high tap density (> 1.0 g cm^{-3}) comparable to that of graphite and a remarkable electrochemical properties in terms of a high reversible capacity of ~ 841 mA h g^{-1} (based on the total weight of the composite), superior cycling stability over 200 cycles, and an excellent rate capability. In this composite structure, the conductive Cu_3Si phase contributes to high conductivity and structural stability by suppressing the formation of $Li_{15}Si_4$ that could cause a large volume change. Simultaneously, the well-intermixed Cu_3Si/Al_2O_3 phase acts as a robust inactive conducting matrix that keeps particle connectivity and provides enhanced electrochemical stability during cycling. Furthermore, the successful formation of nano-sized silicon embedded in the carbon-coated composite allows fast electronic transport and facile ionic diffusion, resulting in rapid charge-discharge capability. The simple and low-cost synthesis method combined with good electrochemical performance achieved in full-cell configuration demonstrates the significant advantages of the carbon-coated silicon-based composites with conductive Cu_3Si as an anode material for high-performance lithium-ion batteries.

Chapter 5: High-Performance Zn–TiC–C Nanocomposite Alloy Anode with Exceptional Cycle Life for Lithium-Ion Batteries†

5.1. INTRODUCTION

As mentioned in Chapter 1, elemental Zn is one of the alternative lithium-alloy based materials. Although it has several advantages as an anode material for lithium-ion batteries, poor cycle and rate performance caused by the volume expansion and particle agglomeration issues during electrochemical cycling make it less favorable candidate. Several recent studies have proven that the introduction of a combined TiC and conductive carbon (TiC + C) buffer is beneficial to improve electrochemical performance of various lithium-alloying active materials.[72-75, 113] Due to the highly conductive, mechanically robust, and electrochemically stable nature of the TiC phase, it can be used as a structure-reinforcing buffer matrix against large volume change during electrochemical cycling in the nanocomposite alloy anode systems.

In this study, we report a strategy of achieving unexpectedly enhanced electrochemical performance of Zn–TiC–C nanocomposite anode by a simple and facile incorporation of Zn nanoparticles into the multifunctional conductive buffer matrix composed of nanocrystalline TiC and carbon. It is obvious that the TiC buffer is much more effective for the volume expansion issue of Zn anode due to the fact that Zn undergoes the relatively smaller volume expansion of ~ 98% (LiZn) during lithiation compared to Si ($Li_{15}Si_4$: ~ 280%), Sn ($Li_{22}Sn_5$: ~ 244%), and Sb (Li_3Sb: ~ 147%). Moreover, the addition of conductive carbon provides further increase in conductivity by maintaining an interparticle electronic transport pathway and good particle aggregation-

† S. -O. Kim and A. Manthiram, "High-performance Zn–TiC–C nanocomposite alloy anode with exceptional cycle life for lithium-ion batteries." *ACS Appl. Mater. Interfaces* **2015**, 7, 14801.
S. –O. Kim carried out the experimental work. A. Manthiram supervised the project. All participated in the preparation of the manuscript.

mitigating effect during prolonged cycling. As a result, the synergistic effects of the conductive TiC + C matrix could lead to dramatic improvement of electrochemical properties by enhancing electrical conductivity, mechanical integrity, and structural stability.

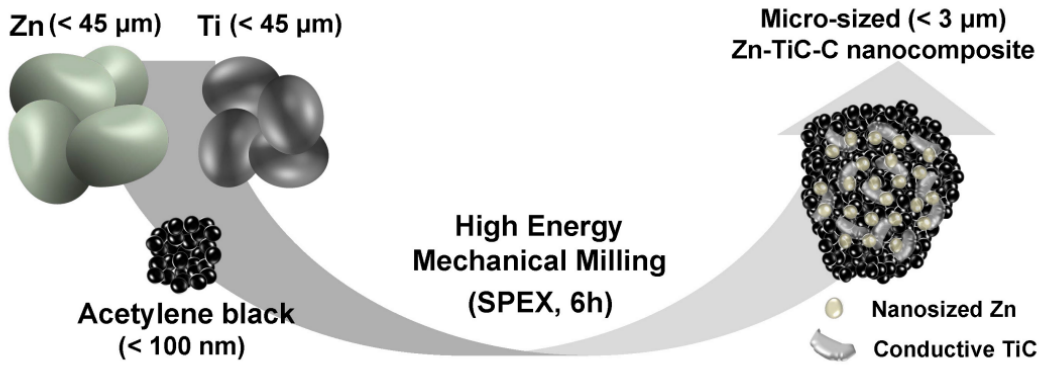

Figure 5.1. Schematic diagram of the preparation of the Zn–TiC–C nanocomposite.

5.2. EXPERIMENTAL

5.2.1. Sample Preparation

The Zn–TiC–C nanocomposite was prepared by the high-energy mechanical milling (HEMM) process with a SPEX 8000M machine. Figure 5.1 shows the schematic diagram of the synthetic route. The precursors used were Zn (98+%, Acros Organics), Ti (99.99%, –325 mesh, Alfa Aesar), and acetylene black carbon (–200 mesh, Alfa Aesar) powders. Elemental Zn and Ti powders were mixed with an atomic ratio of 1 : 1 and an appropriate amount of carbon powders were added to obtain the Zn–TiC–C nanocomposite with a mass ratio of 7 : 3 (Zn–TiC : C). Then, the mixture was placed in a hardened stainless steel vial (80 cm^3) with hardened steel balls and sealed under an Ar atmosphere. The total amount of powder was 2.0 g and a ball-to-powder weight ratio was

fixed at 20 : 1. The HEMM was conducted for 6 h at room temperature. During the HEMM process, the conductive TiC phase is generated by reaction 5.1 below:

$$Zn + Ti + C \rightarrow Zn–TiC–C \text{ nanocomposite} \quad (5.1)$$

The Zn–TiC–C nanocomposite was collected and stored in a vacuum desiccator to minimize surface oxidation. For comparison, a Zn–C composite was prepared by the same method described above, without the addition of elemental Ti powder. The weight ratio of Zn and C was 7 : 3.

5.2.2. Sample Characterization

The structural properties of the Zn-based composites were investigated with a Philips X-ray diffractometer with Cu Kα (λ = 1.5418 Å) radiation and Kratos X-ray photoelectron spectroscopy (XPS). The powder morphology and the detailed microstructure of the Zn–TiC–C nanocomposite was observed with a JEOL JSM–5610 scanning electron microscopy (SEM) equipped with energy dispersive X-ray spectroscopy (EDS), JEOL 2010F high resolution transmission electron microscopy (HRTEM), and Hitachi S–5500 scanning transmission electron microscopy (STEM). A Quantachrome AT–4 Autotap machine was used to obtain the tap density of the samples.

5.2.3. Electrochemical Measurements

The electrodes were prepared by mixing slurries containing 70 wt. % active material (Zn-based composites), 15 wt. % Super P conducting agent, and 15 wt. % polyvinylidene fluoride (PVdF) binder in n-methyl pyrrolidinone (NMP), then coating onto a Cu foil current collector (thickness = 10 μm). After drying in a vacuum oven at 120 oC for 8 h and pressing, the disk electrodes were used to fabricate the CR2032 type coin cells for electrochemical tests. The test cells were assembled in an Ar-filled glove box including a polypropylene (Celgard 2500) separator and a Li foil counter electrode.

The electrolyte used was 1 M $LiPF_6$ dissolved in ethylene carbonate (EC) / diethyl carbonate (DEC) (50 : 50 vol. %). The electrodes used had a typical loading mass of ~ 1.5 mg cm^{-2}.

The charge-discharge experiment was performed at a constant current density of 100 mA g^{-1} within a voltage range of 0.0 – 2.0 V (vs. Li / Li^+) with an Arbin battery tester. Rate capability test was conducted at various current densities from 100 mA g^{-1} to 5 A g^{-1}. The specific capacity was obtained based on the total weight of the active materials including Zn, TiC, and carbon in the electrode. Li was inserted when discharging and extracted during charging steps. An impedance/gain-phase analyzer (Solartron SI 1260) combined with an electrochemical interface (Solartron SI 1286) was used for electrochemical impedance spectroscopy (EIS) measurements, with an AC amplitude of 5 mV within the frequency range of 100 kHz to 0.1 Hz.

5.3. RESULTS AND DISCUSSION

5.3.1. Structure and Morphology

Figure 5.2 gives XRD pattern of the Zn–TiC–C nanocomposite. The broad diffraction peaks corresponding to TiC (JCPDS No. 74-7035, cubic, space group: Fm–3m, a = 4.315 Å) can be clearly observed with the weak Zn peaks (JCPDS No. 78-7021, hexagonal, space group: P63/mmc, a = 2.6591 and c = 4.8868 Å), revealing the presence of conductive TiC phase along with nanosized Zn in the composite. The successful formation of conductive TiC phase is in good agreement with our previous reports on Sn- and Sb-based composite materials.[74, 113] No other peaks were detected, indicating the absence of any of the Zn–Ti and Zn–C binary phases. Compared with the pure Zn precursor and the Zn–C composite (Figure 5.3), the average crystallite size of Zn in the Zn–TiC–C nanocomposite is less than ~ 11 nm as evident from the further weakening

and broadening of Zn diffraction peaks. The decrease in the crystallite size of Zn particle results from the successive deformation induced by HEMM with the TiC phase, which is extremely hard and strong.[77, 114]

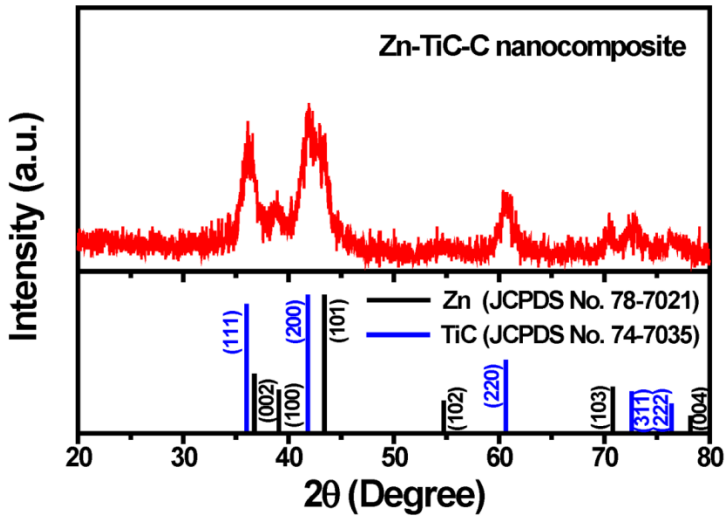

Figure 5.2. XRD pattern of the Zn–TiC–C nanocomposite.

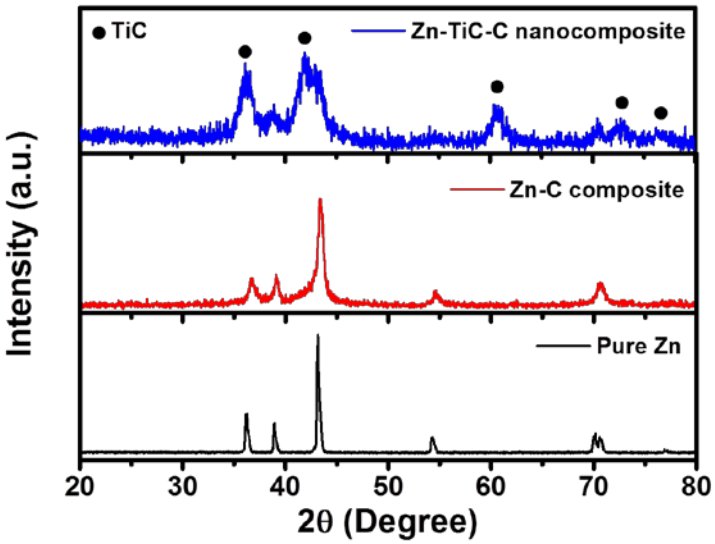

Figure 5.3. Comparison of the XRD patterns of pure Zn, Zn–C composite, and Zn–TiC–C nanocomposite prepared by HEMM for 6 h.

XPS measurement was conducted to characterize the binding energies of the as-synthesized Zn–TiC–C nanocomposite. The obtained XPS spectra and the corresponding curve fitting results for each element (Zn, Ti, and carbon) are given in Figure 5.4. The signal from Zn is deconvoluted into two peaks located at ~ 1044.8 and ~ 1021.7 eV, respectively, from Zn $2p_{1/2}$ and Zn $2p_{3/2}$ as depicted in the Zn 2p spectrum, confirming that Zn does not react with either Ti or carbon during HEMM.[115] In the Ti 2p binding energy spectrum, there are two peaks from Ti $2p_{1/2}$ and Ti $2p_{3/2}$ appearing at the binding energies of ~ 461.0 and ~ 455.0 eV, which are higher than those from metallic Ti 2p peaks (~ 459.8 and ~ 453.9 eV). This indicates, in connection with a weak C 1s peak positioned at ~ 281.7 eV assigned to carbide, the formation of the TiC phase in the resulting nanocomposite powders.[113, 116] Two additional broad peaks located at ~ 463.6 and ~ 457.9 eV, with a binding energy difference (ΔE) of 5.7 eV, could be identified as TiO_2,[117, 118] possibly formed by air exposure.[119, 120] However, the absence of TiO_2 peaks in the XRD pattern (Figure 5.2) suggests that TiO_2 exists as a thin passivation layer only on the surface of the Zn–TiC–C nanocomposite and the amount of formed TiO_2 is negligible.[121] In addition, three peaks at ~ 288.3 (C=O), ~ 285.4 (C–C, sp^3), and ~ 284.5 eV (C=C, sp^2) in the C 1s spectrum can be explained by the excess amount of carbon that remains unchanged after HEMM.[122, 123] Based on the XRD pattern and the XPS spectra discussed above, the Zn–TiC–C nanocomposite is expected to be composed of nanosized Zn, nano- or weakly crystalline TiC, and amorphous carbon phases.

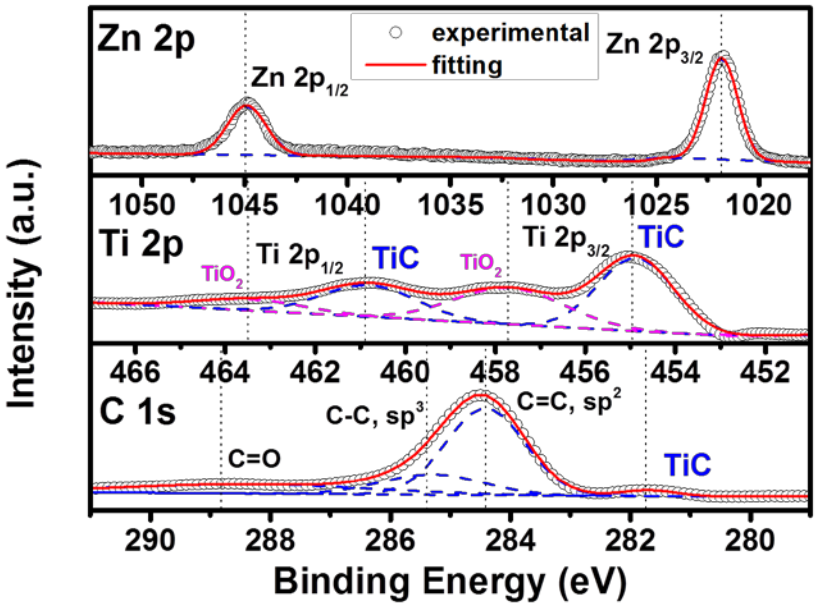

Figure 5.4. XPS spectra in the regions of Zn 2p, Ti 2p, and C 1s of the Zn–TiC–C nanocomposite.

Powder morphology, microstructure, and elemental distribution of the Zn–TiC–C nanocomposite were analyzed by SEM, HRTEM, and STEM. Figure 5.5a shows the SEM image of the Zn–TiC–C nanocomposite. The particle sizes of the Zn–TiC–C nanocomposite are generally in the range of a few micrometers, which is much smaller than that of elemental Zn and the Zn–C composite (Figure 5.6). The significant reduction in the particle size further confirms that the generation of the Zn–TiC–C nanocomposite is caused by the continuous fracture and welding during the HEMM process.[110] Moreover, these particles are thought to be formed by aggregation of nano-sized composite particles. The SEM/EDS result (Figure 5.5b) shows that the amounts of Zn, TiC, and carbon in the Zn–TiC–C nanocomposite were, respectively, estimated to be ~ 34.2, ~ 28.6, and ~ 37.2 wt. %.

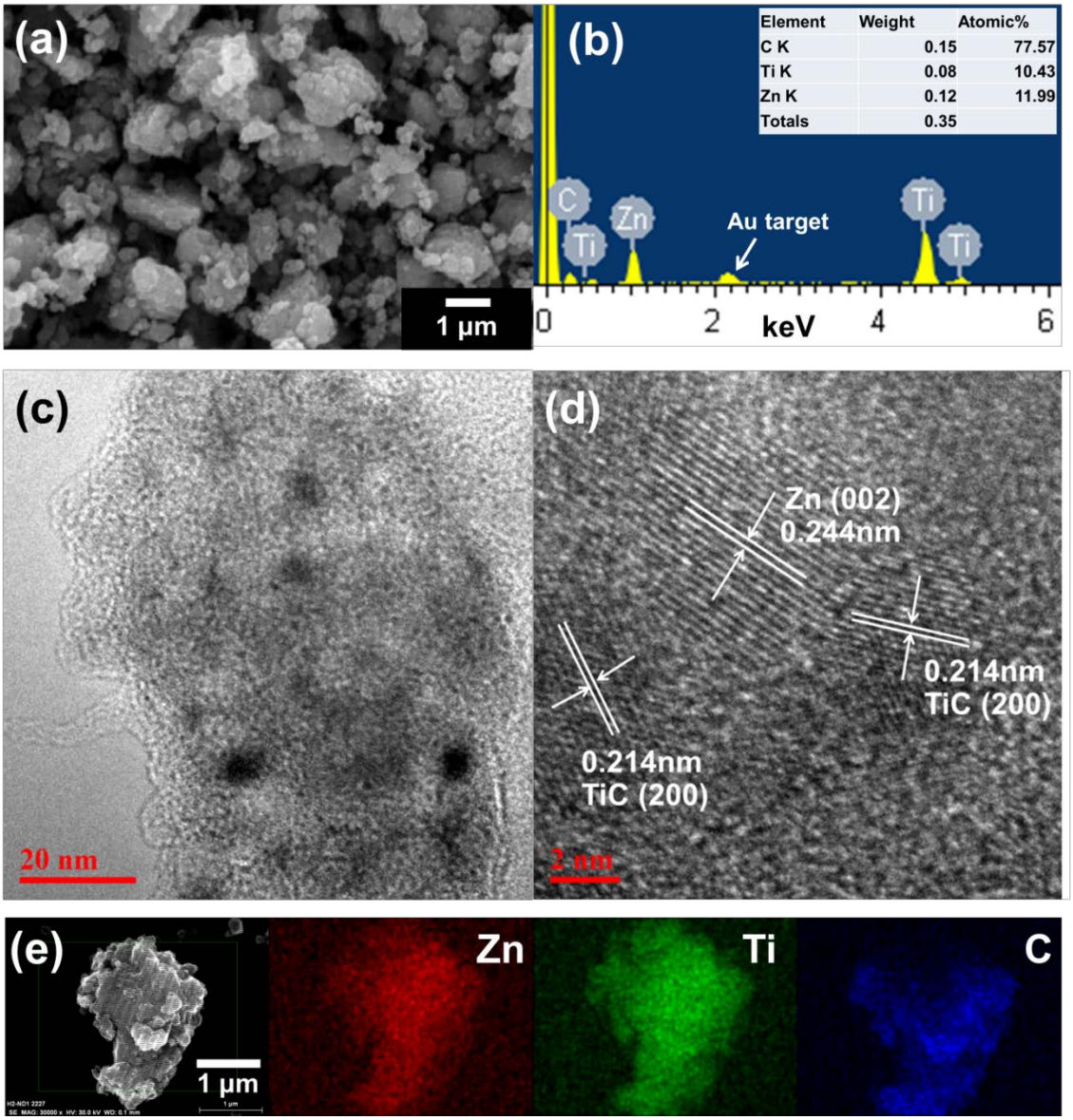

Figure 5.5. (a) SEM image, (b) EDS spectrum, (c) TEM, (d) HR-TEM, and (e) STEM images of the Zn–TiC–C nanocomposite. In STEM, the corresponding EDS mapping images of each element are indicated (Zn: Red, Ti: Green, and carbon: Blue).

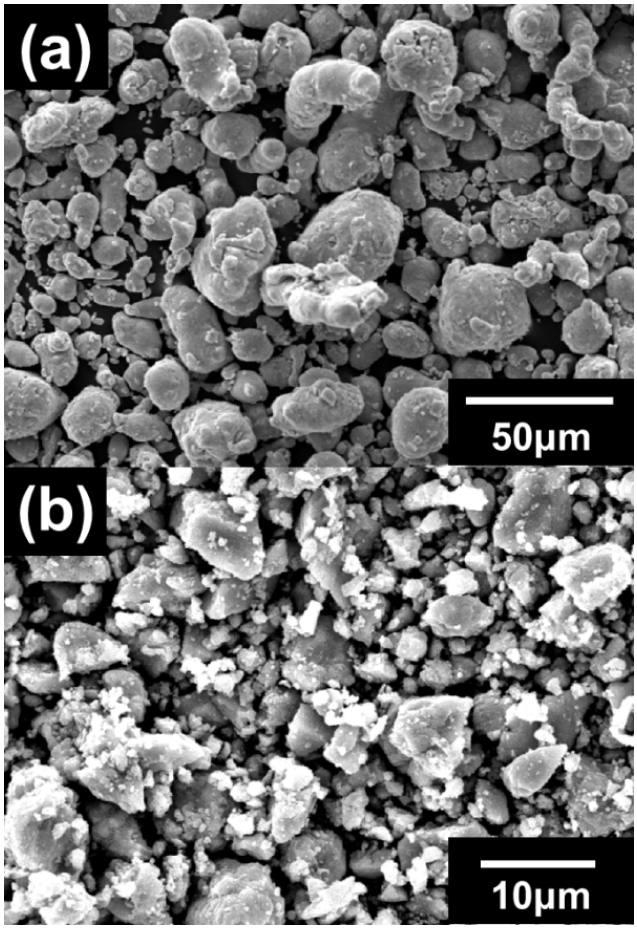

Figure 5.6. SEM images of (a) pure Zn and (b) Zn–C composite.

The TEM and HRTEM images presented in Figure 5.5c and d reveal the detailed microstructure of the Zn–TiC–C nanocomposite. It is obvious that the composite particles are comprised of nanocrystallites (darker area) embedded in an amorphous matrix (brighter area). The crystallite size is estimated to be less than 10 nm, consistent with the XRD analysis as discussed above. These nanocrystallites can be indexed by lattice fringe analysis of the HRTEM image. It is clearly seen that there are two different interplanar spacings that correspond to (002) plane (d = ~ 0.244 nm) of metallic Zn and (200) plane (d = ~ 0.214 nm) of conductive TiC phase. Furthermore, the STEM and corresponding

elemental mapping images in Figure 5.5e confirm the homogeneous distribution of Zn, TiC, and carbon in the nanocomposite particles. This powder morphology is considered to be quite advantageous because the enhanced powder conductivity as well as the strong buffering effect against large volume changes could be provided by the well-mixed TiC + C matrix in the nanostructured composite.

5.3.2. Electrochemical Characterization

Galvanostatic charge and discharge experiments were performed within a voltage range of 0.0 – 2.0 V (vs. Li / Li^+) in order to assess the electrochemical performance of the Zn-based electrodes. Figure 5.7a and b represent the voltage profiles of the Zn–C composite and Zn–TiC–C nanocomposite electrodes at a current density of 100 mA g^{-1}. The Zn–C composite electrode shows first discharge (lithiation) and charge (delithiation) capacities of, respectively, 1011 and 515 mA h g^{-1}. The corresponding Coulombic efficiency is very low (~ 51.0%), which is comparable to the case of pure Zn (~ 51.8%) (Figure 5.8a). In contrast, the first lithiation and delithiation capacities of the Zn–TiC–C nanocomposite electrode are, respectively, 641 and 402 mA h g^{-1}, with a higher initial Coulombic efficiency of ~ 62.7%. Considering that TiC is electrochemically inactive toward Li,[72, 76, 78] the initial capacity loss is mainly caused by the irreversible reactions of Zn with Li. Therefore, the Zn–TiC–C nanocomposite is expected to exhibit the improved reversibility because the introduction of the conductive TiC phase reduces the percentage of Zn in the composite. After the first cycle, although the Zn–C composite exhibits a gradual decrease in reversible capacity during the initial 50 cycles, an excellent capacity retention can be observed for the Zn–TiC–C nanocomposite, as indicated by the fact that the voltage profile patterns remain quite similar over 500 cycles.

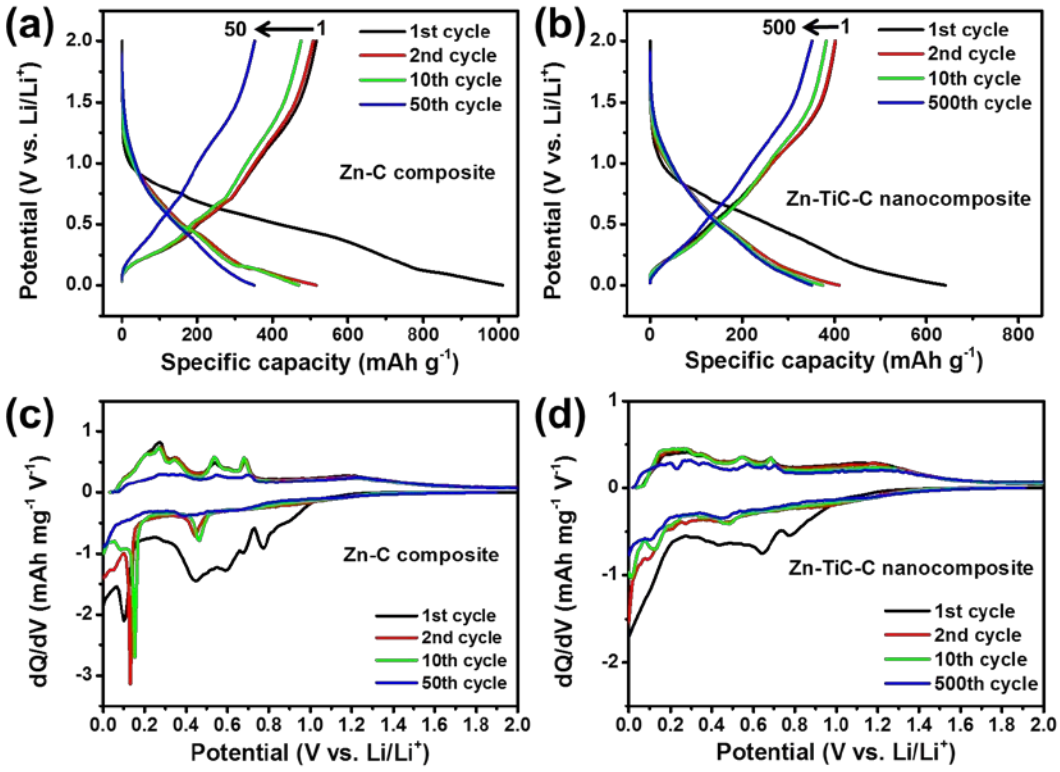

Figure 5.7. Voltage profiles of (a) Zn–C composite and (b) Zn–TiC–C nanocomposite and differential capacity plots of (c) Zn–C composite and (d) Zn–TiC–C nanocomposite at various cycles within a voltage window of 0.0 – 2.0 V (vs. Li / Li^+) in 1 M $LiPF_6$ dissolved in EC / DEC (50 : 50 vol. %) electrolyte.

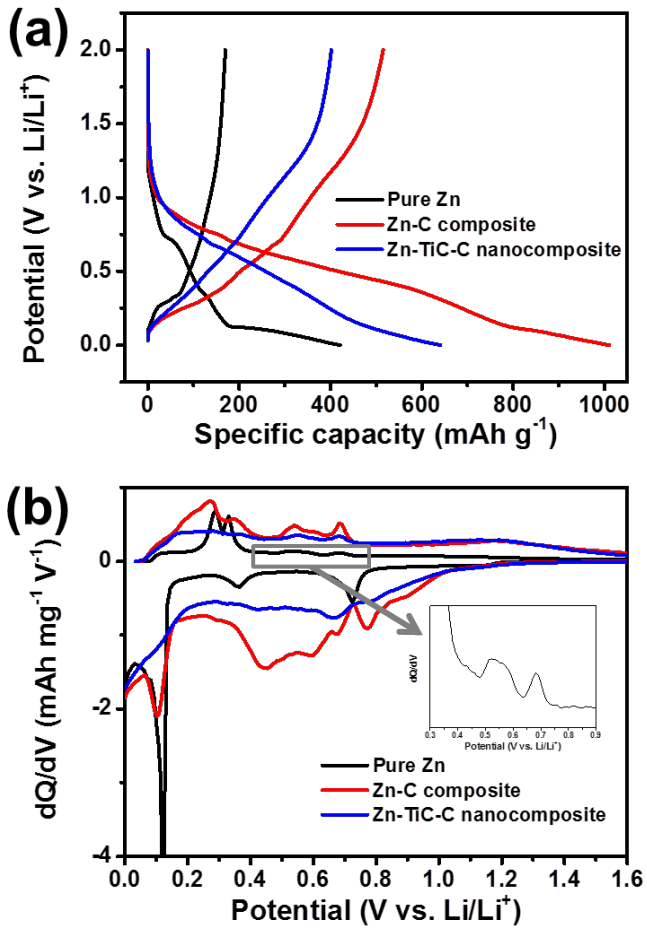

Figure 5.8. Comparison of the (a) voltage profiles and (b) differential capacity plots of pure Zn, Zn–C, and Zn–TiC–C nanocomposite electrodes at the first cycle. The electrochemical tests were conducted at current densities of 50 mA g^{-1} (for pure Zn electrode) and 100 mA g^{-1} (for Zn–C and Zn–TiC–C nanocomposite electrodes) within a voltage window of 0.0 – 2.0 V (vs. Li / Li^+) in 1 M $LiPF_6$ dissolved in EC/DEC (50 : 50 vol. %) electrolyte.

To better understand the reaction mechanism of Zn with Li in the Zn–TiC–C nanocomposite, the differential capacity plots (DCPs) of the Zn-based electrodes at various cycle numbers are presented in Figure 5.7c and d. The DCP curve of the pure Zn electrode (Figure 5.8b) is used to investigate electrochemical reactions between Zn and Li. During the first discharge process, it displays three peaks at ~ 0.7, ~ 0.4, and ~ 0.12

V, which are associated with, respectively, the formation of SEI layer on the surface of Zn, eventually forming the LiZn phase ($Zn \rightarrow LiZn_4 \rightarrow LiZn$).[35, 37] Upon first charge, four reaction peaks are seen at ~ 0.28, ~ 0.33, ~ 0.55, and ~ 0.68 V, which are indicative of the successive delithiation processes from LiZn to Zn ($LiZn \rightarrow Li_2Zn_3 \rightarrow LiZn_2 \rightarrow LiZn_4 \rightarrow Zn$).[37] As shown in Figure 5.7c, although these peaks are not clearly observed for the Zn–C composite electrode in the first discharge step, the presence of four peaks during charging confirms the occurrence of the abovementioned Li–Zn reactions. The large and broad peaks (0.3 ~ 1.0 V) are arising from the irreversible reaction of Li with the excess amount of carbon and this is expected to mainly contribute to the large capacity loss in the first cycle, in conjunction with the SEI formation.[75, 113] The Zn–C composite shows the Li–Zn reaction peaks at ~ 0.4 and ~ 0.12 V from the second cycle, but they no longer appear after 50 cycles, indicating the poor reversibility and low electrochemical stability of the active Zn in the Zn–C composite. This is believed to be ascribed to the aggregation of Zn particles during repeated cycling that is vulnerable to particle crumbing and the ensuing electrode degradation, analogous to the other Li-alloying materials such as Sn and Sb.[75, 89, 113, 124] In the case of the Zn–TiC–C nanocomposite (Figure 5.7d), all the Li–Zn alloying and dealloying reaction peaks are also observable. Nevertheless, the DCP profiles are rather smooth and show much broader reaction peaks, revealing the generation of Zn nanocrystllites in the Zn–TiC–C nanocomposite as a result of the HEMM process. Moreover, the active Zn nanoparticles in the Zn–TiC–C nanocomposite still undergo reversible reaction with Li even after 500 cycles. These results demonstrate the effectiveness of TiC + C conductive matrix for the improvement of electrochemical properties by suppressing particle agglomeration and enabling high utilization of the Zn active particles.

Figure 5.9 illustrates and compares the cycle performance of the Zn-based electrodes at a current density of 100 mA g^{-1}. Table 5.1 summarizes electrochemical data of the Zn-based electrodes, including the first discharge and charge capacities, initial Coulombic efficiency, and capacity retention after certain cycles. The pure Zn shows much lower specific capacity compared to its theoretical value (~ 410 mA h g^{-1}), which might be caused by the large particle size that could hinder a full lithiation process into metallic Zn particles at a relatively higher current density of 100 mA g^{-1}. The Zn–C composite exhibits significantly higher initial Li insertion and extraction capacities. This is mainly due to the formation of nanosized Zn dispersed in carbon matrix that could facilitate lithiation/delithiation processes by providing good electronic pathway among the composite particles. A reversible capacity of > 450 mA h g^{-1} is maintained up to 40 cycles, but it gradually decreases to less than ~ 340 mA h g^{-1} after 60 cycles. On the other hand, it is remarkable to note that the Zn–TiC–C nanocomposite electrode delivers stable reversible capacity of as high as 360 mA h g^{-1} and it retains ~ 318 mA h g^{-1} over 800 cycles, indicating the excellent cycle performance with a high capacity retention of ~ 79.2%. Since the TiC phase does not react with Li, it could remain uniformly distributed in the composite even after continuous electrochemical cycling. Consequently, the TiC phase keeps not only acting effectively as a reinforcing matrix that mitigates the volume change of the Zn active material but also providing high conductivity throughout the composite in combination with excess carbon, resulting in significantly enhanced cycling stability of the Zn–TiC–C nanocomposite. Considering that the reversible capacity of amorphous carbon is ~ 480 mA h g^{-1} (Figure 5.10), the capacity contribution from Zn is estimated to be ~ 410 mA h g^{-1} (LiZn), which is almost the same as its theoretical value.[37] Such a high utilization of Zn active particles (~ 100%) is probably due to the nanocomposite architecture composed of a homogeneous dispersion of Zn nanoparticles

within the combined highly conductive TiC + C matrix. Therefore, we could conclude that the introduction of TiC + C matrix leads to high conductivity and high reversibility of Zn anode as well as the mechanical buffering effect to alleviate the large volume changes upon extended cycling.

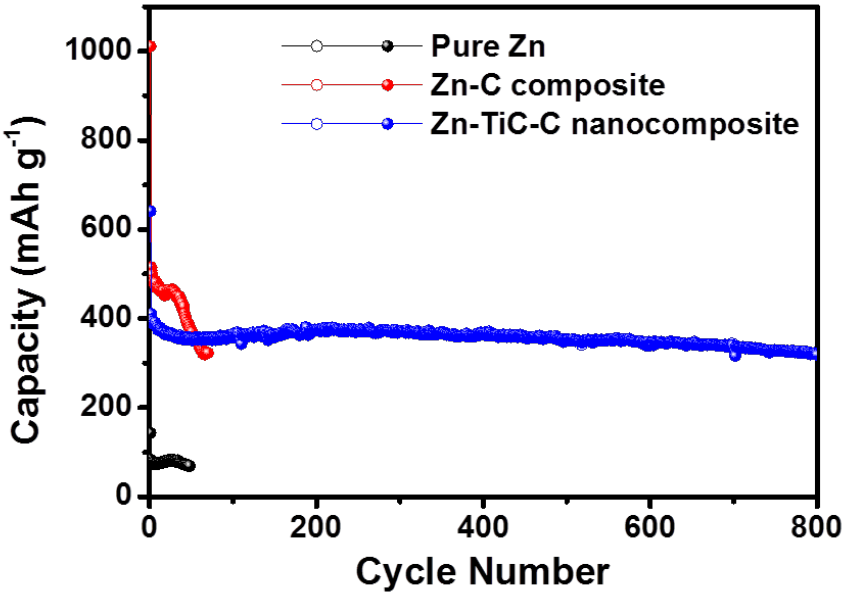

Figure 5.9. Cycle performance of the pure Zn, Zn–C, and Zn–TiC–C nanocomposite electrodes. The specific capacity was calculated based on the total mass of active materials.

Table 5.1. Electrochemical data of the Zn-based electrodes.

Electrode	1st discharge capacity (mA h g^{-1})	1st charge capacity (mA h g^{-1})	1st Coulombic efficiency (%)	Capacity retention (n^{th}/1st charge capacity) (%)
Pure Zn	143	74	51.9	92.1 (n = 50)
Zn–C composite	1011	515	51.0	65.4 (n = 60)
Zn–TiC–C nanocomposite	641	402	62.7	79.2 (n = 800)

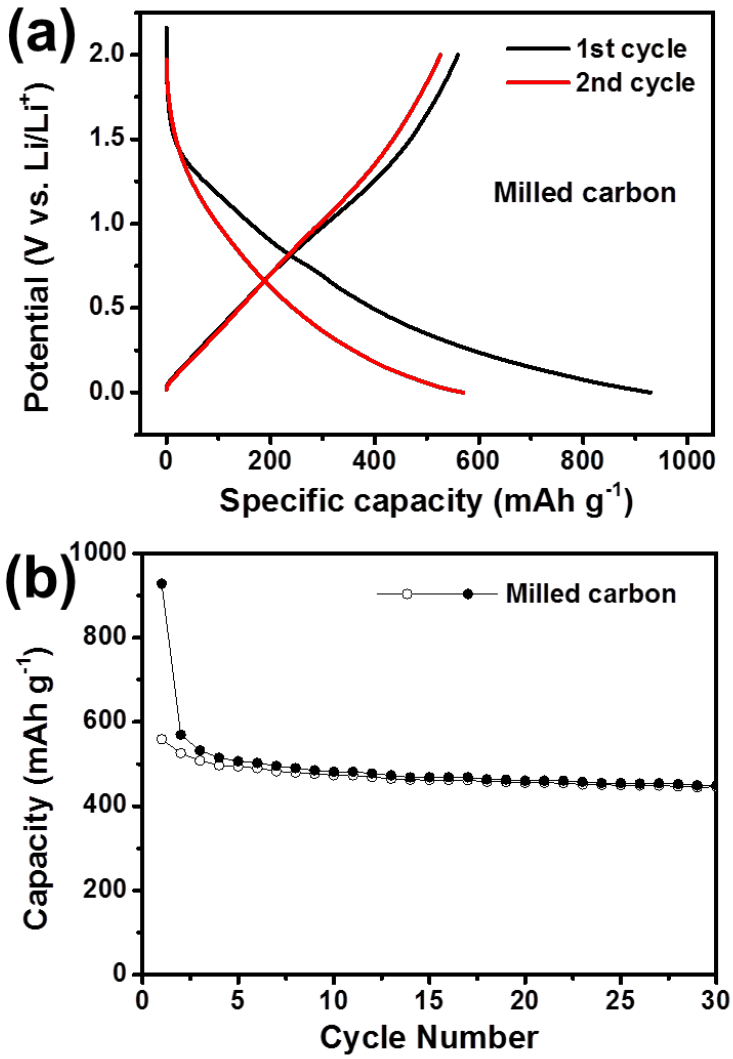

Figure 5.10. (a) Voltage profiles and (b) cycle performance of the milled carbon (acetylene black) electrode. Electrochemical tests were conducted at a current density of 100 mA g^{-1} within a voltage window of 0.0 – 2.0 V (vs. Li / Li^+) in 1 M $LiPF_6$ dissolved in EC/DEC (50 : 50 vol. %) electrolyte.

The EIS studies (Figure 5.11) further support the enhancement in the conductivity of the Zn–TiC–C nanocomposite during the electrochemical test. Figure 5.12 shows the curve fitting results and each resistance value is summarized in Table 5.2. The difference in the charge-transfer resistance values between the Zn–C (47.2 Ω mg) and Zn–TiC–C nanocomposites (31.3 Ω mg) is rather small after the first cycle. However, the Zn–TiC–C nanocomposite (52.3 Ω mg) shows significantly lower charge-transfer resistance compared to the Zn–C composite (174.9 Ω mg) after 50 cycles, resulting from the maintenance of good electron transport path between active particles by suppressing or preventing the electrode pulverization.

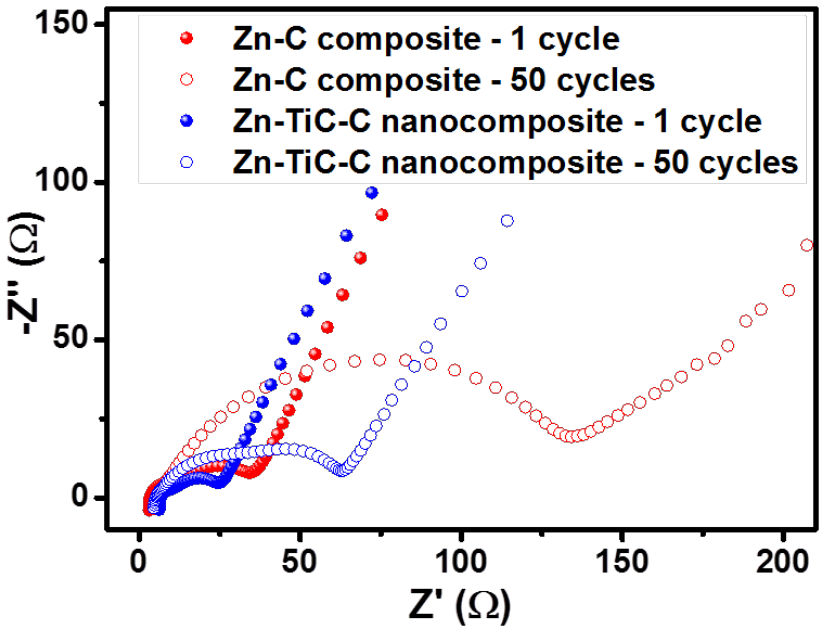

Figure 5.11. Nyquist plots of the Zn–C and Zn–TiC–C nanocomposite electrodes after 1 and 50 cycles.

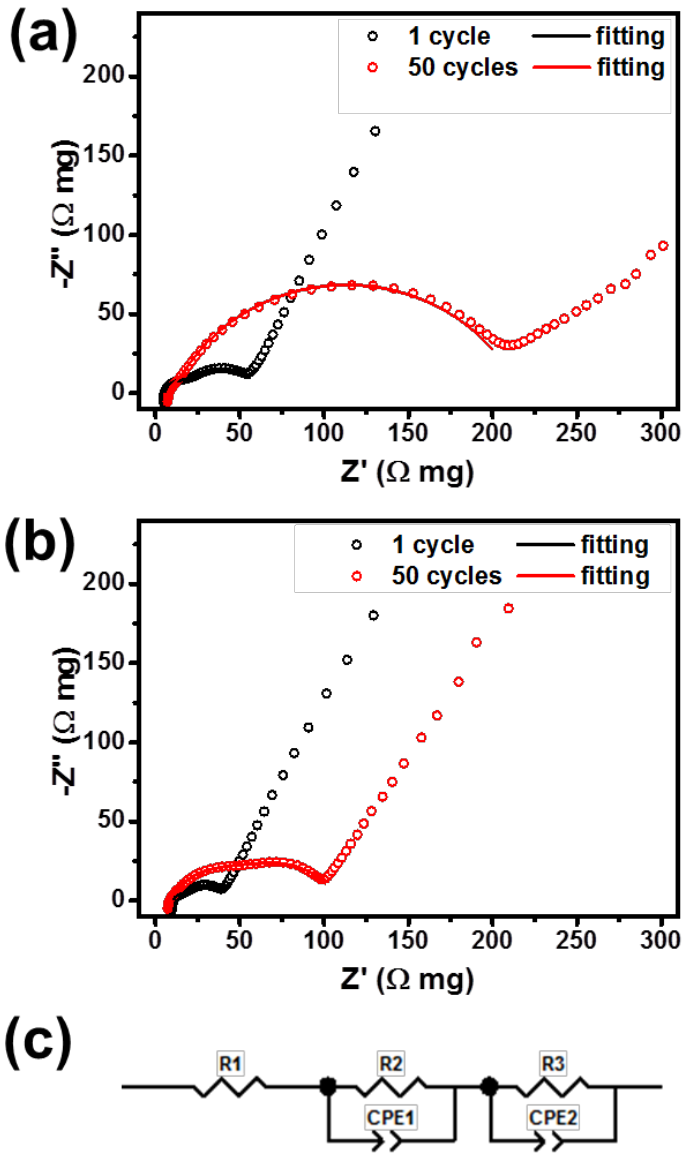

Figure 5.12. Impedance spectra and curve fitting results for the (a) Zn–C and (b) Zn–TiC–C nanocomposites. (c) Simplified equivalent circuit used for the curve fitting. (R1: Electrolyte resistance, R2: Interfacial resistance, CPE1: Constant phase element of interface, R3: Charge transfer resistance, CPE2: Constant phase element of charge transfer reaction)

Table 5.2. Resistance component values of the Zn-based composite electrodes upon cycling.

Electrode	Component	Resistance (Ω mg)	
		at 1st cycle	at 50th cycle
Zn–C composite	R_s	5.5	7.9
	R_{int}	9.8	61.4
	R_{ct}	47.2	174.9
Zn–TiC–C nanocomposite	R_s	10.5	8.3
	R_{int}	3.6	46.2
	R_{ct}	31.3	52.3

Figure 5.13 shows the variation of the volumetric capacity and corresponding Coulombic efficiency of the Zn–TiC–C nanocomposite electrode as a function of cycle numbers. It is generally known that graphite has a low tap density of ~ 1.0 g cm^{-3},[75, 89] leading to a low volumetric capacity that needs to be improved. With a high tap density of ~ 1.3 g cm^{-3}, the Zn–TiC–C nanocomposite electrode displays a stable volumetric capacity of ~ 468 mAh cm^{-3}, which is ~ 1.35 times higher than that of graphite. The Coulombic efficiency quickly increases to 99.9% by the 5th cycle and maintains an average value of ~ 99.95% through 800 cycles. Consequently, the Zn–TiC–C nanocomposite shows superior cycle performance and outperforms commercial graphite in terms of volumetric capacity that is > 413 mAh cm^{-3} even after 800 cycles. In addition, electrochemical characterization is further performed at various current densities from 100 mA g^{-1} (0.25C) to 5 A g^{-1} (12.5C) (1C = 400 mA g^{-1}) to evaluate the effects of the TiC + C buffer on the rate capability of the Zn–TiC–C nanocomposite. As can be seen in Figure 5.14, the Zn–TiC–C nanocomposite electrode exhibits excellent rate performance, with specific charge capacities of ~ 400, ~ 365, ~ 345, and ~ 322 mA h g^{-1}, respectively, at current densities of 0.25, 1.25, 2.5, and 7.5C rates. It is surprising that it retains a high

specific capacity of ~ 300 mA h g^{-1} at very high current densities of as high as 12.5C, which is ~ 75% of its capacity at 0.25C rate. This result further suggests the facile Li-ion transport properties of the Zn active particles through the short diffusion path, which could be obtained by the confinement of nanosized Zn particles in the combined nanostructured TiC + C dispersing matrix that can prevent small Zn particles from aggregating into large Zn clusters even after repeated fast charge and discharge cycling.

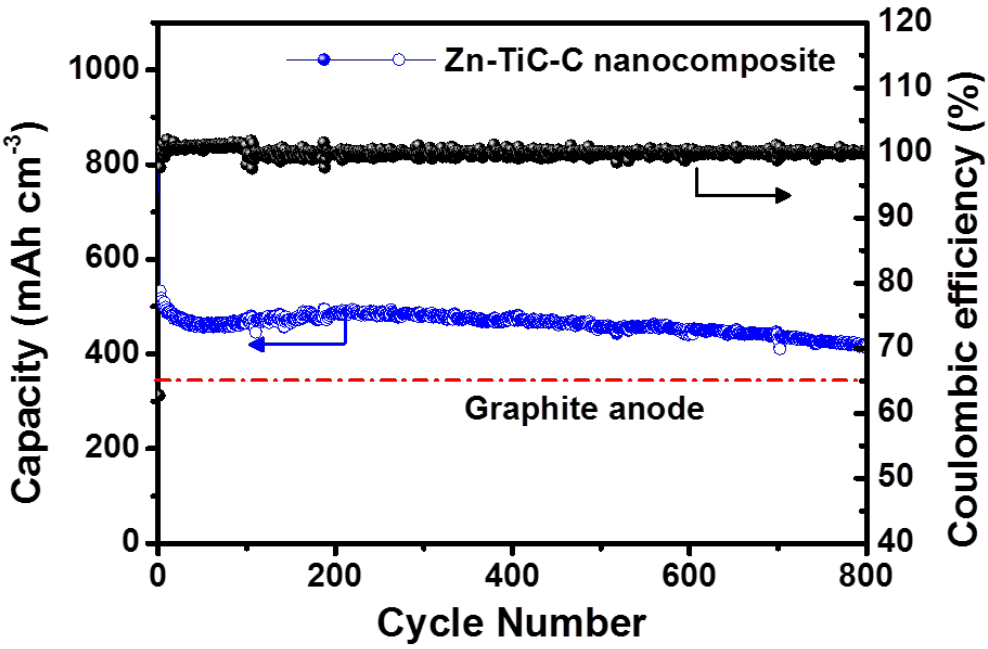

Figure 5.13. Variation of the volumetric capacity and corresponding Coulombic efficiency as a function of cycle number.

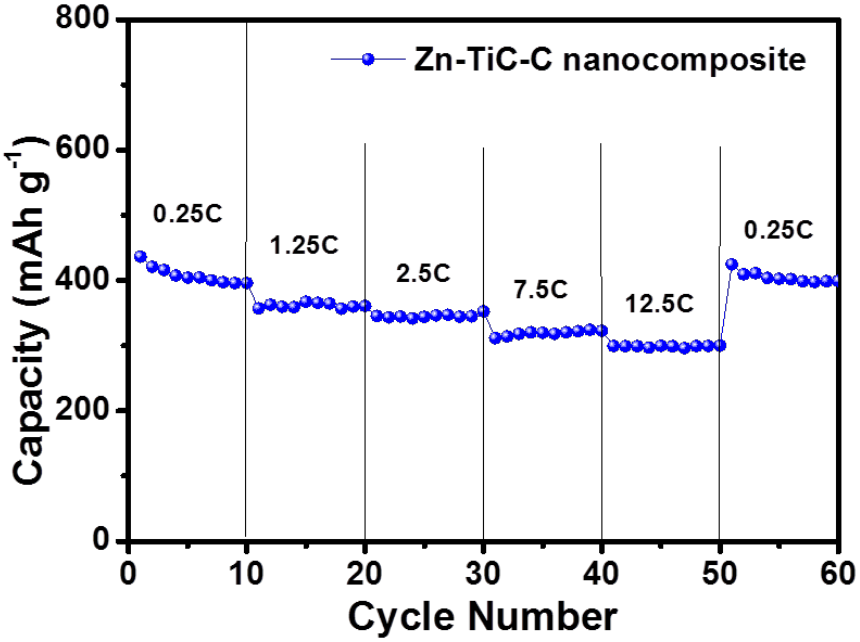

Figure 5.14. Rate capability of the Zn–TiC–C nanocomposite electrode at various current densities (1 C = 400 mA g^{-1}). Note that the specific capacity and tap density of graphite in (c) are assumed to be, respectively, 350 mAh g^{-1} and 1.0 g cm^{-3}.

5.4. CONCLUSION

We have successfully synthesized the Zn–TiC–C nanocomposite through a low cost, facile, high yield, and environmentally friendly HEMM process. The simple application of the well-blended TiC and carbon conductive matrix into Zn anode demonstrates superior electrochemical performance in terms of a stable reversible capacity of ~ 318 mA h g^{-1} with exceptionally long cycle life of over 800 cycles and high rate capability up to 12.5C rate. This dramatic performance improvement is mainly attributed to the realization of a novel nanostructured composite composed of Zn nanoparticles uniformly embedded within the TiC + C matrix. The conductive TiC + C buffer in the nanostructured Zn–TiC–C composite offers high electronic conductivity,

structural reinforcement, and durable dispersing matrix that could overcome several problems associated with Zn anode such as particle growth, electrode pulverization, and huge volume change occurring during repeated cycling. Overall, we believe that the Zn–TiC–C nanocomposite has a great potential to be employed as an alternative anode materials in lithium-ion batteries and our simple and practical strategy can also be applied to explore various other nanocomposite materials for lithium-ion batteries as well as sodium-ion batteries.

Chapter 6: Facile Synthesis and Enhanced Sodium-Storage Performance of Chemically Bonded CuP_2/C Hybrid Anode†

6.1. INTRODUCTION

Elemental phosphorus and metal phosphide systems have attracted significant attention as promising anode materials for sodium-ion batteries. Although phosphorus has the highest theoretical capacity of 2596 mA h g^{-1} compared to other possible candidates, it also has problems such as the large volume variation during cycling and low conductivity issues, analogous to the silicon anode discussed in Chapters 3 and 4. As mentioned in Chapter 1, the preparation of various phosphorus-carbon composite and metal phosphide systems have demonstrated the performance improvement to some extent.

In this regard, a combination of the above strategies would be promising and could be used as an effective way to explore and realize high-performance alloy-based anode materials for sodium-ion batteries. Nevertheless, only a few studies of metal phosphide – carbon composites have been reported to date. Xiao et al. showed that the Sn_4P_3/C composite anode delivers an initial reversible capacity of ~ 650 mA h g^{-1} at 100 mA g^{-1} with a good capacity retention of ~ 86% over 150 cycles,[125] demonstrating the effectiveness of the combined approach for the enhancement of reversible sodium-storage performance. In addition, Zhao et al. reported that the carbon-coated CuP_2 composite exhibits a specific capacity of ~ 500 mA h g^{-1}, based on reversible conversion of CuP_2 during cycling.[126] However, the poor long-term cycling stability caused by the detachment of carbon coating layers during cycling still needs to be overcome.

---

† S. -O. Kim and A. Manthiram, "Facile synthesis and enhanced sodium-storage performance of chemically bonded CuP_2/C hybrid anode." *Chem. Commun.* **2016**, 52, 4337.
S. -O. Kim carried out the experimental work. A. Manthiram supervised the project. All participated in the preparation of the manuscript.

Several recent studies have suggested that introduction of stable P–C or P–O–C chemical bonds to the phosphorus-based anode systems leads to improved electrochemical performance for lithium- and sodium-ion storage.[43, 127-129] These chemical bonds are also believed to prevent electrode pulverization by restraining the volume expansion of phosphorus particles and provide good electronic conductive pathway by maintaining an interparticle connection even after extended cycling. Herein, we report a rapid synthesis of a CuP_2/C hybrid material by a one-step mechanochemical reaction employing high-energy mechanical milling (HEMM) and its enhanced reversible sodium-storage performance. We demonstrate that the carbon hybrid network, which is chemically bonded to the active CuP_2, plays a crucial role as a durable embedding matrix that enhances electrode conductivity, accommodates large volume changes, and preserves the mechanical integrity of the active materials during repeated cycling. The CuP_2/C hybrid electrode exhibits a high reversible capacity of ~ 450 mA h g^{-1} with a high tap density of ~ 1.2 g cm^{-3}, outstanding cycling stability (with ~ 95% capacity retention over 100 cycles), and good rate capability, making it a promising anode candidate for sodium-ion batteries.

6.2. EXPERIMENTAL

6.2.1. Sample Preparation

The CuP_2/C hybrid sample was synthesized by a simple one-step high energy mechanical milling (HEMM) method. Commercial red phosphorus (98+%, Alfa Aesar), copper (99%, 45 μm, Acros Organics), and acetylene black carbon (–200 mesh, Alfa Aesar) powders were used as raw materials for the synthesis without further treatment. Elemental red phosphorus and copper powders were mixed with a molar ratio of 2 : 1 and further blended with different amounts of acetylene black carbon (10, 20, and 30 wt. %).

The mixture was placed in a hardened stainless steel vial (80 cm^3) with hardened steel balls and sealed in an argon-filled glovebox followed by HEMM at a rotation rate of 1060 rpm for 3 h at room temperature with a SPEX 8000M machine. The total mass of the powder was 2.0 g and a ball-to-powder weight ratio was fixed at 20 : 1. The obtained powder samples were stored in a vacuum desiccator in order to minimize surface oxidation. Since preliminary electrochemical study showed that the optimum carbon content in the hybrid sample is 20 wt. % (Figure 6.1), all the data presented hereafter refer to CuP_2/C hybrid with 20 wt. % carbon. For a comparison, pure CuP_2 was also prepared without acetylene black carbon by the same procedure described above. Then, CuP_2 was simply mixed with 20 wt. % of carbon by hand grinding to obtain the CuP_2/C composite in order to check the effect of P–O–C bonding on the electrochemical performance of the CuP_2/C hybrid.

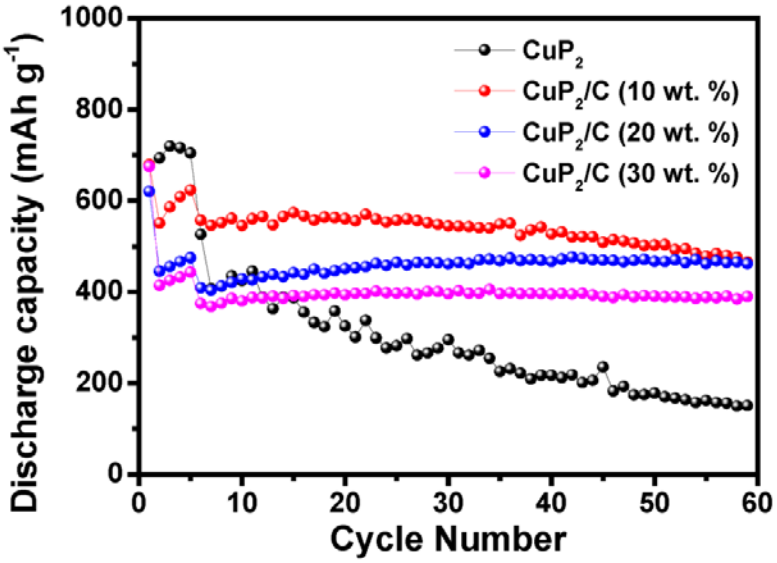

Figure 6.1. Cycle performance of pure CuP_2 and CuP_2/C hybrids with different amounts of carbon at a current density of 200 mA g^{-1} within a voltage range of 0.0 – 1.5 V (vs. Na / Na^+). The cells were tested at 50 mA g^{-1} for the initial 5 cycles for activation.

6.2.2. Sample Characterization

The structural characterizations of the samples were carried out with X-ray diffraction (XRD: Rigaku MiniFlex 600) with Cu Kα (λ = 1.54059 Å) radiation, X-ray photoelectron spectroscopy (XPS: Kratos Analytical), and Fourier transform infrared spectroscopy (FTIR: Thermo Scientific Nicolet iS5). Scanning electron microscopy (SEM: JEOL JSM–5610) with energy dispersive X-ray spectroscopy (EDS), scanning transmission electron microscopy (STEM: Hitachi S–5500), and transmission electron microscopy (TEM: JEOL 2010F) were used to analyze the surface morphology and elemental distribution of the powder samples. The carbon content was estimated by thermogravimetric analysis (TGA: Netzsch STA449 F3 Jupiter) and the tap density of the samples was determined with a Quantachrome AT–4 Autotap machine.

6.2.3. Electrochemical Measurements

The electrodes were fabricated by depositing slurries containing 70 wt. % active material, 15 wt. % conducting agent (Super P), and 15 wt. % poly(acrylic) acid (PAA) binder (MW ~250,000, 35 wt. % in water, Aldrich) onto a copper foil current collector, followed by drying in a vacuum oven at 120 ^{o}C for over 8 h. Then, the electrodes were cut into disks with an area of 1.13 cm^2. The typical loading mass of the active materials was ~ 2.0 mg cm^{-2}. The CR2032 coin cells were fabricated inside an argon-filled glove box by employing polypropylene (Celgard 2500) separator and sodium foil counter/reference electrode. The electrolyte used was 1.0 M $NaClO_4$ in a mixture of ethylene carbonate (EC) and diethyl carbonate (DEC) (1 : 1 v/v) with the addition of 5 vol. % of fluoroethylene carbonate (FEC) additive. Galvanostatic cycling tests were performed with a battery testing system (Arbin BT–2000) within a voltage range of 0.0 – 1.5 V (vs. Na / Na^+). Electrochemical impedance spectroscopy (EIS) experiments were carried out with an impedance/gain-phase analyzer (Solartron SI 1260A) combined with

an electrochemical interface (Solartron SI 1287A) with the ac amplitude of 5 mV over a frequency range from 100 kHz to 0.1 Hz. For the *ex situ* XRD and SEM analyses, the electrodes were collected by disassembling the test cells in the argon-filled glove box, rinsing with DEC several times, and drying at room temperature.

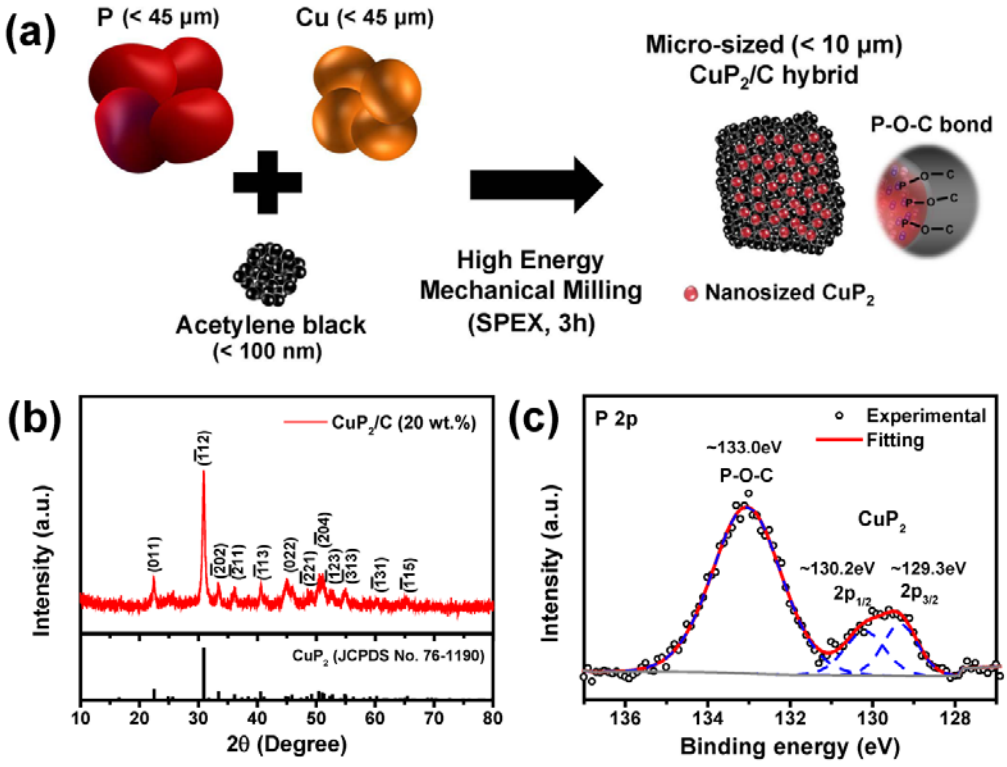

Figure 6.2. (a) Schematic diagram illustrating the synthesis, (b) XRD pattern, and (c) XPS P 2p spectrum of the CuP_2/C hybrid.

6.3. Results and Discussion

6.3.1. Structure and Morphology

Figure 6.2a illustrates the preparation of the CuP_2/C hybrid material by the HEMM process. Structural characterization was conducted XRD and XPS. The XRD pattern of the CuP_2/C hybrid (Figure 6.2b) shows that all the diffraction peaks could be

indexed to the crystalline CuP_2 phase (JCPDS No. 76-1190, monoclinic, S.G. = P21/c), indicating the successful generation of CuP_2 after 3 h of milling with no side reactions. The CuP_2/C hybrid shows considerably broader peaks with lower intensity than the pure CuP_2 phase (Figure 6.3), suggesting that the CuP_2 in the CuP_2/C hybrid has a significantly reduced average crystallite size.

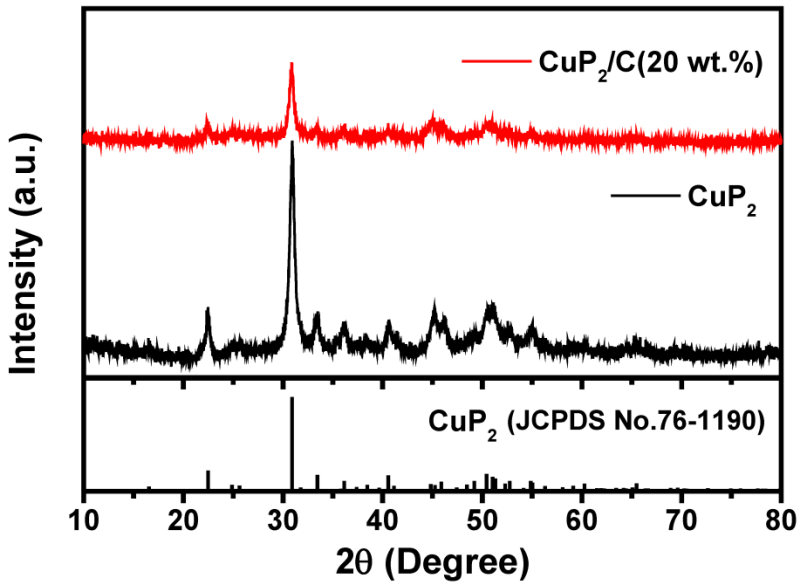

Figure 6.3. Comparison of XRD patterns of pure CuP_2 and CuP_2/C hybrid synthesized by HEMM for 3 h.

The XPS P 2p spectrum of the as-prepared CuP_2/C hybrid sample (Figure 6.2c) contains two broad peaks that can be deconvoluted into three components located at ~ 133.0, ~ 130.2, and ~ 129.3 eV. The two peaks at ~ 130.2 and ~ 129.3 eV correspond, respectively, to the P $2p_{1/2}$ and P $2p_{3/2}$ regions of the CuP_2 phase; these peaks are shifted to lower binding energies compared to elemental phosphorus (P $2p_{3/2}$: ~ 129.9 eV).[43] This is in good agreement with the previous reports of other metal phosphide systems.[67,

[68] In addition, the peak at ~ 133.0 eV is indicative of the presence of strong P–O–C chemical bonds in the CuP_2/C hybrid, which is located at significantly lower binding energy than the peak corresponding to phosphates.[64] The P–O–C bond is possibly formed during the high-energy milling process by the chemical reaction of carbon with a thin native oxide layer on the surface of the phosphorus particles (Figure 6.4a).[39] This observation can be further confirmed by Fourier transform infrared spectroscopy (FTIR) (Figure 6.4b). While the hand-mixed CuP_2/C composite shows only P=O and P–O bonds, a sharp peak occurring at ~ 1008 cm^{-1} associated with the P–O–C bonds is clearly observed for the ball-milled CuP_2/C hybrid.[128, 129] The successful formation of the P–O–C bond is expected to provide improved electrochemical reversibility and cycling stability for the CuP_2/C hybrid electrode. The actual amount of carbon in the hybrid was estimated to be ~21.9 wt. % from thermogravimetric analysis (Figure 6.5), which is almost the same as the amount of carbon used to make the hybrid sample (20 wt. %).

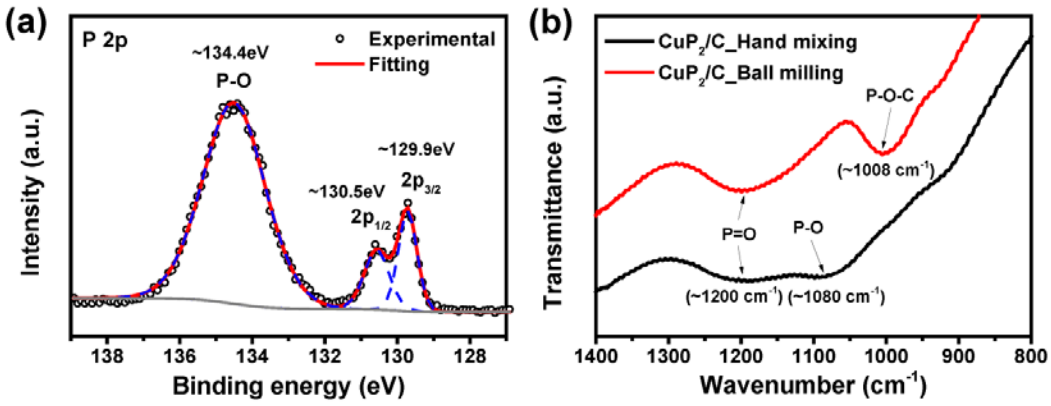

Figure 6.4. (a) XPS P 2p spectrum of elemental phosphorus. (b) Comparison of the FTIR spectra of the hand-mixed CuP_2/C (20 wt. % carbon) composite and ball-milled CuP_2/C (20 wt. % carbon) hybrid.

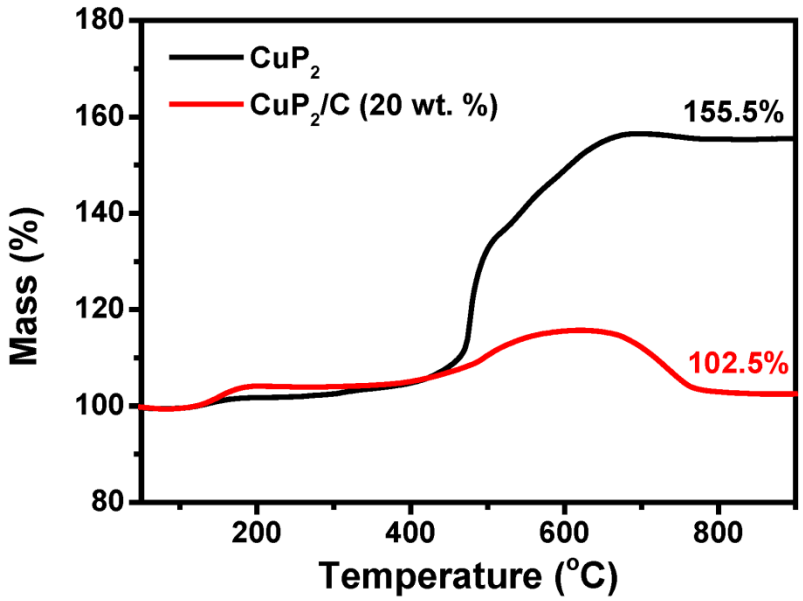

Figure 6.5. TGA curves of pure CuP_2 and the CuP_2/C (20 wt. % carbon) hybrid.

SEM, TEM, and STEM were employed to observe the particle size, microstructure, and elemental distribution of the CuP_2/C hybrid. The SEM image of the CuP_2/C hybrid shown in Figure 6.6a reveals that the particle size of the carbon hybrid sample is less than ~ 10 μm, which is much smaller than that of pure CuP_2 (Figure 6.7). It is obvious that micro-sized particles increase particle tap density and thereby improve the volumetric capacity, which is critical for practical applications.[66, 108] The tap density of the CuP_2/C hybrid is estimated to be ~ 1.2 g cm^{-3}, which is considerably higher than that of hard carbon materials (0.50 ~ 0.81 g cm^{-3}).[130, 131]

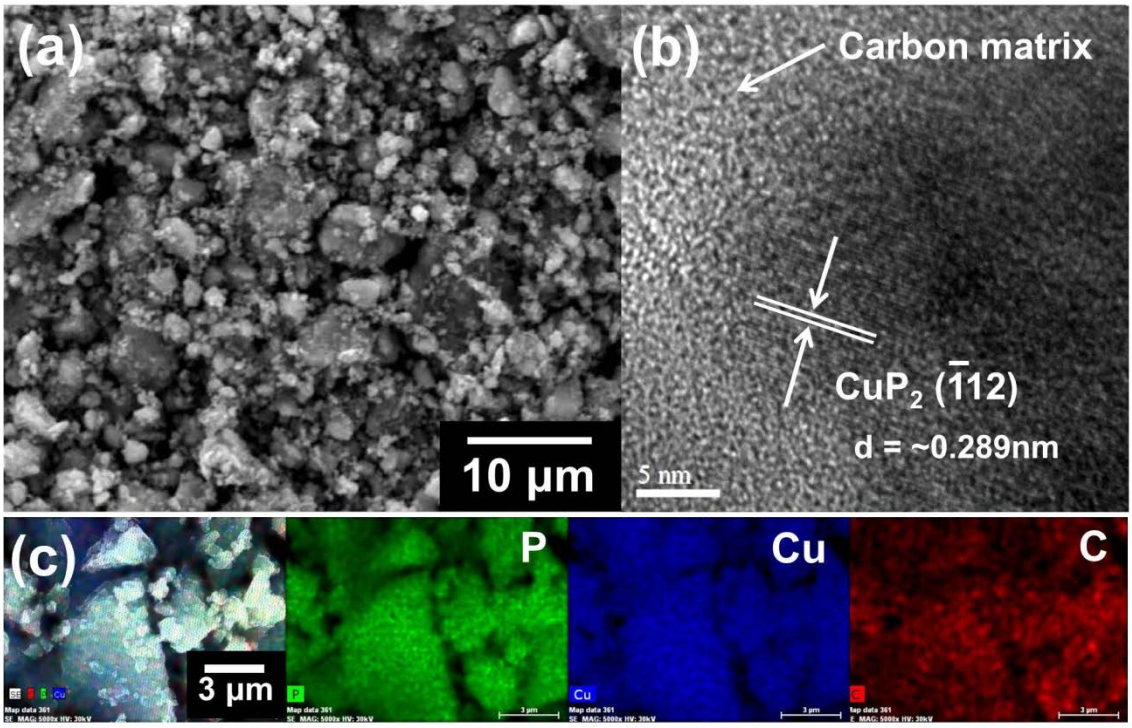

Figure 6.6. (a) SEM, (b) HR-TEM, and (c) STEM and corresponding elemental mapping images (P: green, Cu: blue, and C: red) of the CuP_2/C hybrid.

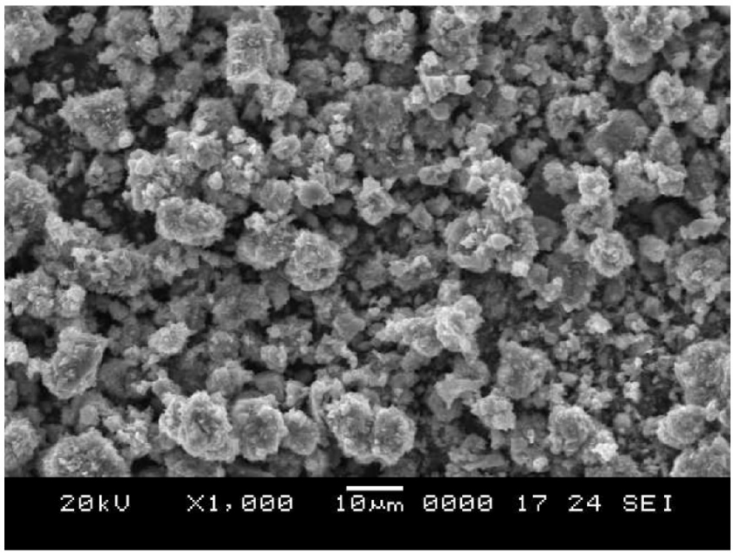

Figure 6.7. SEM image of pure CuP_2 synthesized by HEMM for 3 h.

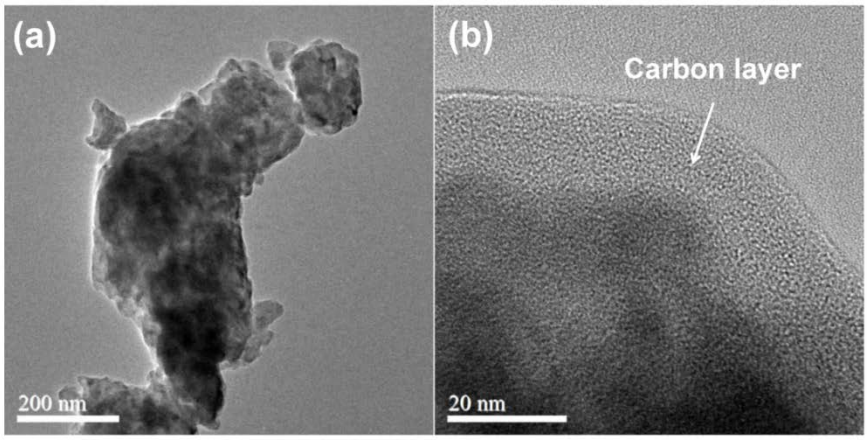

Figure 6.8. (a) Low- and (b) high-magnification TEM images of the CuP_2/C hybrid.

The TEM images (Figure 6.8) show that the hybrid particle is composed of aggregated nanoclusters that are well-encapsulated by a conductive carbon layer. The lattice fringes of crystallites with an interplanar spacing of ~ 0.289 nm are clearly observed in the high-resolution TEM image in Figure 6.6b, and are attributed to the $(1\bar{1}2)$ plane of the CuP_2 phase. This observation further confirms the generation of nanosized CuP_2 particles during HEMM, corroborating the XRD and XPS results discussed above. It is worth mentioning that the use of carbon in the HEMM process suppresses particle growth and agglomeration by embedding the active material in the carbon matrix;[74, 132] the observed particle size of CuP_2 was restricted to a few tens of nanometers. Consequently, enhancement in electrochemical activity can be anticipated due to the formation of nanosized CuP_2 that is well-dispersed in the conductive network, which reduces the diffusion distance and facilitates electron / ion transfer between active particles. The STEM and elemental mapping images (Figure 6.6c) display the homogeneous distribution of each element in the sample powder, indicating that the carbon hybrid matrix effectively provides improved particle conductivity and acts as a

mechanical buffer against the huge volume changes occurring during sodiation/desodiation.

6.3.2. Electrochemical Characterization

The electrochemical tests were carried out galvanostatically with a CuP_2/C hybrid working electrode and a sodium counter/reference electrode to evaluate the sodium-storage performance. Figure 6.9a and b show the voltage profiles and differential capacity plots (DCPs) of the CuP_2/C hybrid electrode at various cycles, tested within a voltage range of 0 – 1.5 V (vs. Na / Na^+) at a current density of 50 mA g^{-1}. The initial discharge and charge capacities of the CuP_2/C hybrid electrode are, respectively, 611 and 396 mA h g^{-1}; these capacity values and current density are calculated based on the total mass of the hybrid material including carbon. The initial Coulombic efficiency is ~ 65%, which is lower than that of pure CuP_2 electrode (~ 77%, Figure 6.10a), possibly due to the reduced particle size that causes large irreversible capacity loss associated with the formation of SEI layer during the first discharge process[133] and the low initial Coulombic efficiency of the milled acetylene black (~ 38%, Figure 6.10b) used for the conductive hybrid network. Both sodium insertion and extraction capacities increased in subsequent cycle, indicating that the sodiation reaction of CuP_2 requires an initial activation for breaking the Cu – P chemical bond. In contrast to the large polarization observed for the pure CuP_2 electrode from the 10th cycle (Figure 6.10a), the CuP_2/C hybrid anode maintains a sloping profile with consistency up to 50 cycles, confirming the enhanced electrochemical reversibility.

The DCPs in Figure 6.9b show the electrochemical reactions of the CuP_2/C hybrid during sodiation and desodiation. All the main cathodic and anodic peaks are located at the same potentials, as with pure CuP_2 (Figure 6.10c). The small and broad peaks at 1.0 – 0.5 V are an indication of the formation of the SEI layer during the first discharge

process.[64, 134] Two more peaks are clearly observed at ~ 0.3 and ~ 0.05 V when discharged further to 0 V, and there are two broad peaks appearing at ~ 0.55 and ~ 0.8 V during the following charge process. It should be noted that only the extracted phosphorus contributes to the sodium storage capacity of CuP_2 since the metallic copper is not reactive toward sodium. Therefore, all four peaks can be attributed to the successive conversion reactions between sodium and phosphorus (Na_xP, x = 0 – 3), which is in good agreement with the literature.[62, 70, 135]

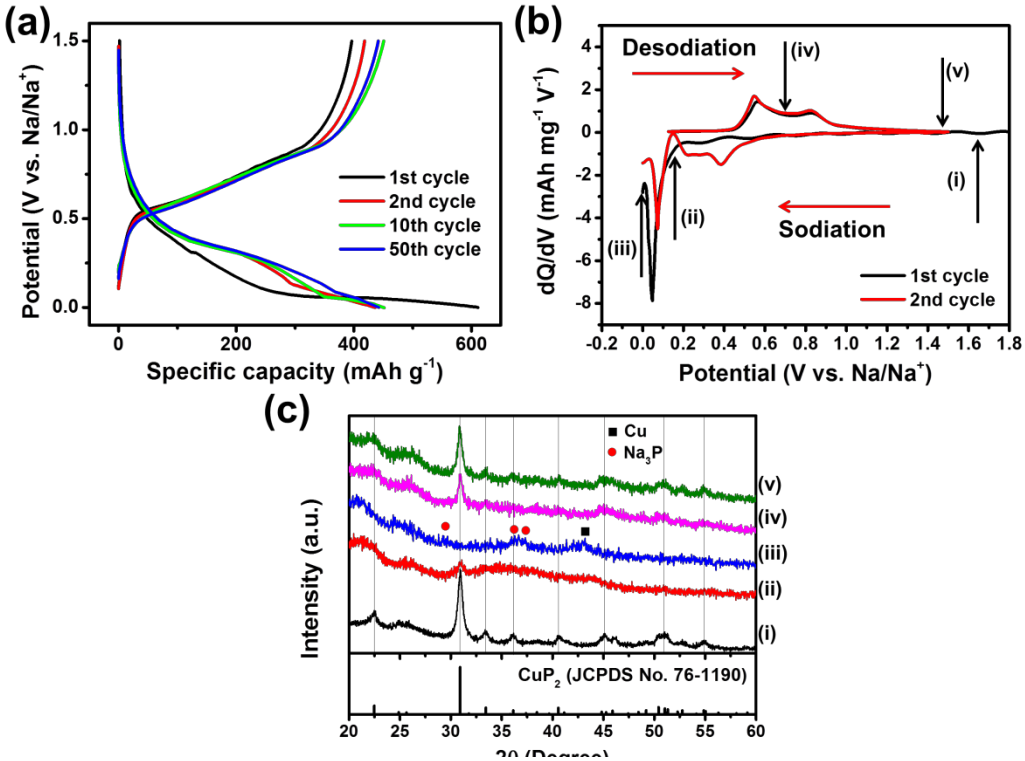

Figure 6.9. (a) Voltage profiles, (b) differential capacity plots (DCPs) at various cycles, and (c) ex situ XRD patterns at various states of charge indicated in (b) of the CuP_2/C hybrid: (i) OCV, (ii) 0.2 V, (iii) 0 V, (iv) 0.7 V, and (v) 1.5 V.

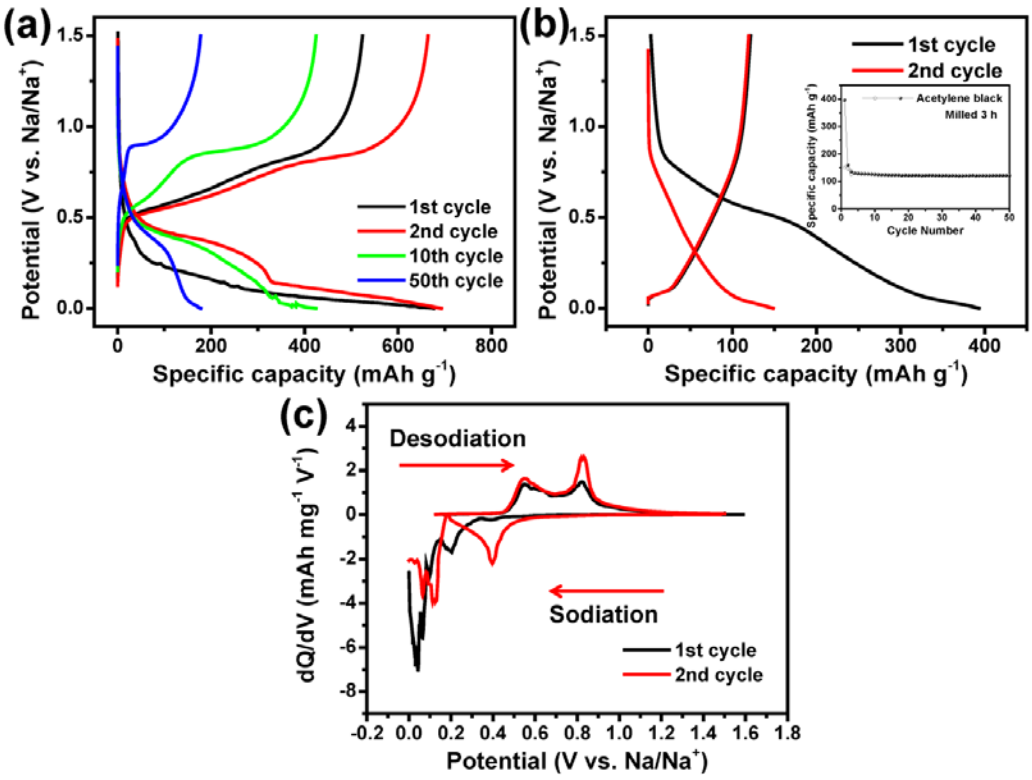

Figure 6.10. Voltage profiles of the (a) pure CuP_2 and (b) milled acetylene black electrodes at various cycle numbers. The inset in (b) shows the cycle performance of the milled acetylene black. (c) DCPs of the pure CuP_2 electrode at initial two cycles.

In order to further elucidate the reaction mechanism of CuP_2, the phase change during the first sodiation and desodiation cycle was investigated by *ex situ* XRD at different states of charge (indicated in Figure 6.9b). As shown in Figure 6.9c, all the characteristic peaks match well with those of crystalline CuP_2 phase before sodiation. When discharged to 0.2 V, the CuP_2 diffraction peaks become broadened and the peak intensity is lowered, suggesting the formation of amorphous Na_xP intermediates resulting from the sodiation reaction of phosphorus extracted by the dissociation of the CuP_2 phase. Furthermore, although the CuP_2 peaks are no longer detected at full sodiation (0

V), four small and broad peaks have evolved simultaneously, which can be assigned to Na_3P and copper metal. Upon charging to 0.7 V, these peaks disappear and the CuP_2 peaks gradually reappear. In addition, the CuP_2 peaks continue to grow and become significant when fully charged to 1.5 V, indicating that the CuP_2 phase can be reversibly restored during the desodiation process. Therefore, based on the *ex situ* XRD results, the sodiation and desodiation mechanism of CuP_2 can be summarized as below:

$$\text{Discharge:} \quad CuP_2 + 6\,Na^+ + 6\,e^- \rightarrow 2\,Na_3P + Cu \qquad (6.1)$$

$$\text{Charge:} \quad 2\,Na_3P + Cu \rightarrow CuP_2 + 6\,Na^+ + 6\,e^- \qquad (6.2)$$

Cycle performance of the pure CuP_2 and CuP_2/C hybrid electrodes are compared in Figure 6.11. Half cells were tested at 50 mA g^{-1} for the initial 5 cycles for activation and then at 200 mA g^{-1} in the subsequent cycles. The pure CuP_2 electrode exhibits poor cyclability with a rapid capacity drop after 5 cycles. However, the CuP_2/C hybrid electrode delivers a high specific capacity of ~ 450 mA h g^{-1} with excellent capacity retention over 100 cycles. Its reversible capacity is maintained at > 430 mA h g^{-1} even after 100 cycles, retaining ~ 95.5% of its capacity at the 5th cycle. To check the effect of P–O–C bonding on the electrochemical performance, cycling test of the hand-mixed CuP_2/C composite electrode was also performed under the same conditions (Figure 6.12). Due to higher carbon content, the hand-mixed CuP_2/C composite electrode shows better cyclability up to 50 cycles than the pure CuP_2 electrode. However, compared to the hybrid electrode, severe capacity fade is observed with the hand-mixed CuP_2/C composite electrode from 10th cycle and its reversible capacity is ~ 320 mA h g^{-1} after 50 cycles, maintaining only ~ 64.1% of its capacity at the 5th cycle. Therefore, it can be

concluded that both the P–O–C chemical bond and the carbon conductive buffer contribute to the improved electrochemical performance of the CuP_2/C hybrid electrode.

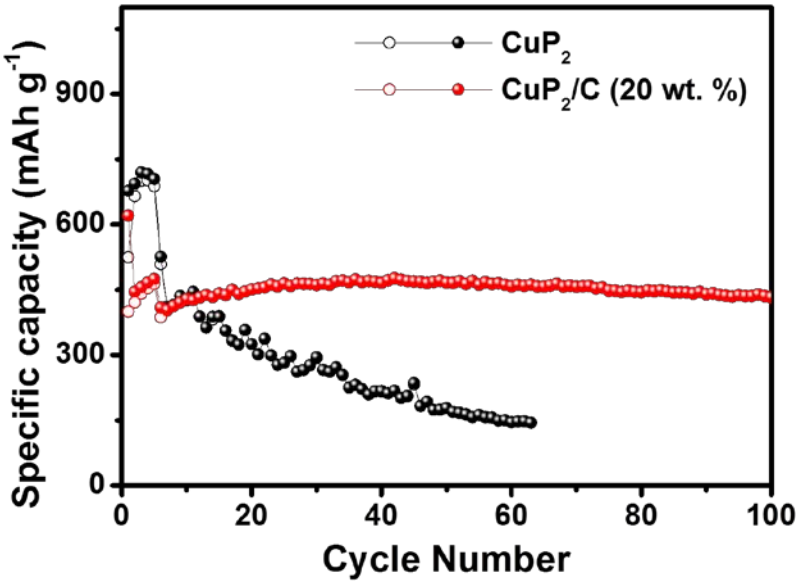

Figure 6.11. Comparison of the cycle performance of the pure CuP_2 and CuP_2/C hybrid electrodes. The specific capacity was presented based on the total mass of the hybrid material including carbon.

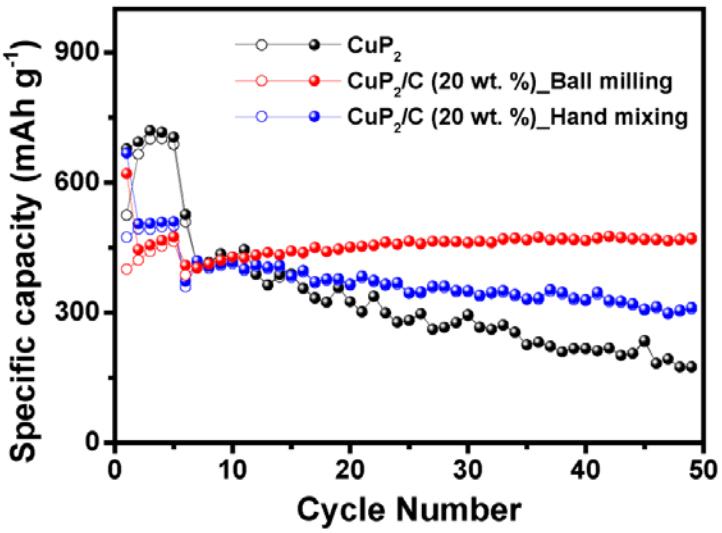

Figure 6.12. Comparison of the cycle performances of pure CuP_2, hand-mixed CuP_2/C composite, and ball-milled CuP_2/C hybrid electrodes at a current density of 200 mA g^{-1}. The cells were tested at 50 mA g^{-1} for the initial 5 cycles for activation.

EIS was conducted to further examine the origin of the significantly enhanced electrochemical performance of the CuP_2/C hybrid electrode (Figure 6.13). According to the curve fitting results using a simplified equivalent circuit (Figure 6.14), all the resistance components exhibit similar values in both electrodes after 5 cycles as summarized in Table 6.1. However, while the pure CuP_2 electrode shows significantly increased interfacial (34.0 Ω) and charge-transfer resistances (84.8 Ω) after 50 cycles, both the interfacial and charge-transfer resistance of the CuP_2/C hybrid remain almost unchanged, and are measured to be, respectively, 6.8 and 35.3 Ω. Therefore, the dramatic improvement in the electrochemical performance is believed to be mainly associated with (i) the successful formation of the P–O–C chemical bonding that results in a strong attachment of the carbon matrix to the active CuP_2 particles, thereby maintaining good

electrical conduction pathway in the hybrid particles and (ii) the realization of the nanoscale hybrid network by incorporating nanosized CuP_2 particles into the carbon matrix that could eventually lead to fast sodiation/desodiation processes. Moreover, the conductive carbon buffer is electrochemically stable, as evident from the changes in the electrode surface morphology before and after 50 cycles (Figure 6.15), thereby endowing enhanced interfacial stability to the CuP_2 particles upon repeated cycling. This could be further verified by the *ex situ* SEM analyses of the pure CuP_2 and CuP_2/C hybrid electrodes after 50 cycles. While the pure CuP_2 electrode shows severe loss of active materials after 50 cycles, the CuP_2/C hybrid electrode keeps a smooth surface during repeated cycling, suggesting improved mechanical integrity of the active materials (Figure 6.16).

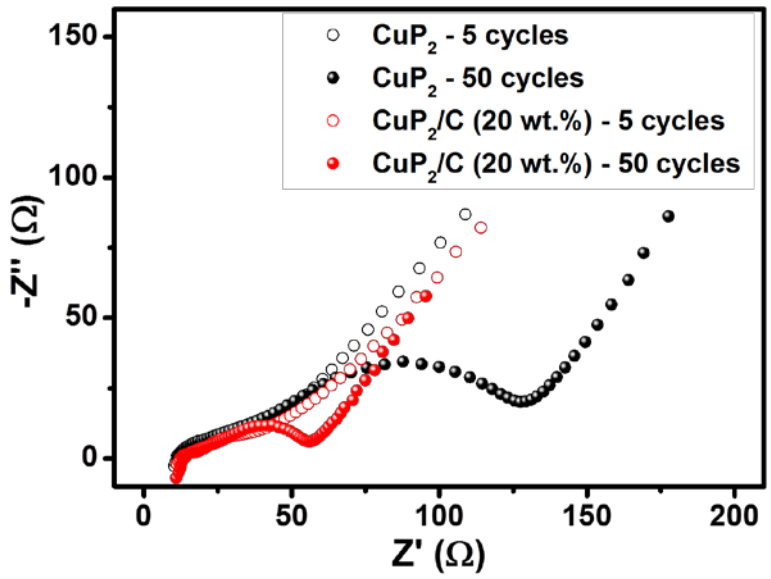

Figure 6.13. Comparison of impedance spectra of the pure CuP_2 and CuP_2/C hybrid electrodes after 5 and 50 cycles.

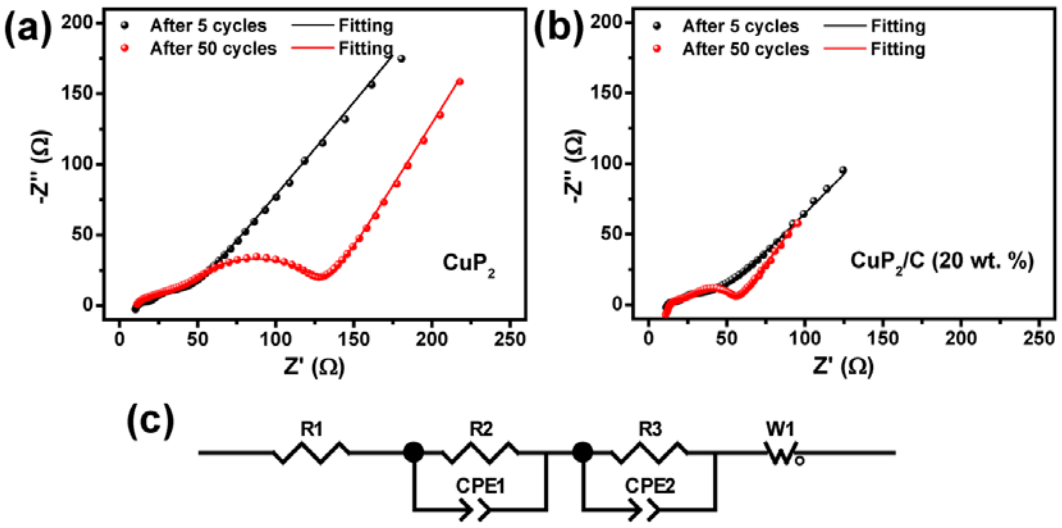

Figure 6.14. Impedance spectra and curve fitting results for the (a) pure CuP_2 and (b) CuP_2/C hybrid electrodes after 5 and 50 cycles. (c) Simplified equivalent circuit used for the curve fitting.

Table 6.1. Variations of the resistance component values of the CuP_2 and CuP_2/C hybrid electrodes (R1(R_s): Electrolyte resistance, W1: Warburg impedance, R2 (R_{int}): Interfacial resistance, CPE1: Constant phase element of interface, R3 (R_{ct}): Charge transfer resistance, CPE2: Constant phase element of charge transfer reaction)

Electrode	Component	Resistance (Ω)	
		at 5 cycles	at 50 cycles
CuP_2	R_s	11.8	9.9
	R_{int}	5.0	34.0
	R_{ct}	25.7	84.8
CuP_2/C (20 wt.%) hybrid	R_s	12.4	14.2
	R_{int}	3.0	6.8
	R_{ct}	29.1	35.3

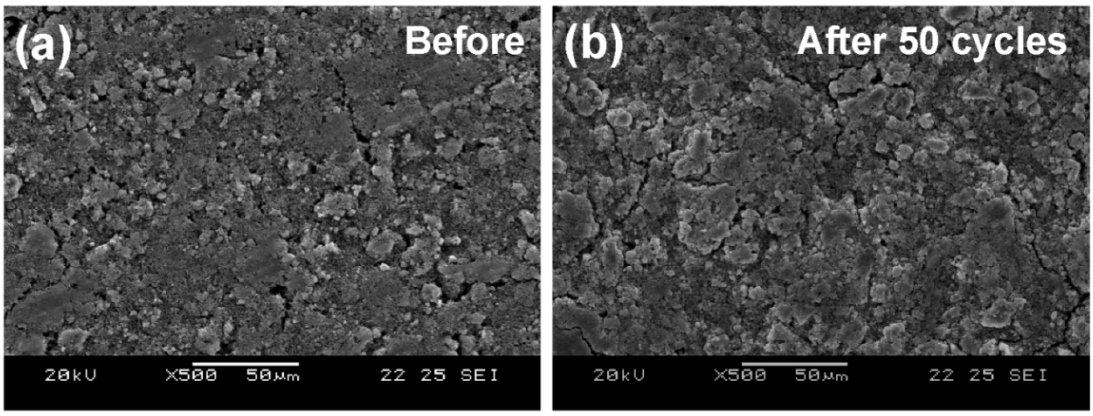

Figure 6.15. Changes in the electrode surface morphologies of the milled acetylene black electrodes (a) before and (b) after 50 cycles.

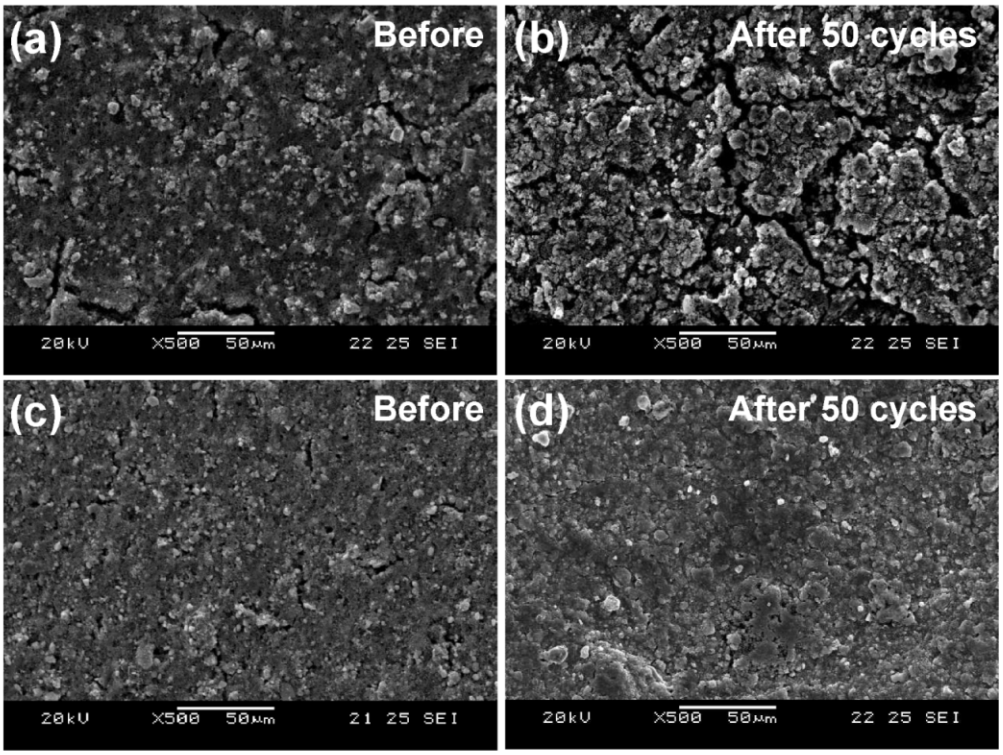

Figure 6.16. Changes in the electrode surface morphologies of the (a and b) pure CuP_2 and (c and d) CuP_2/C hybrid electrodes before and after 50 cycles.

With the aid of these features, the rate capability of the hybrid electrode could also be significantly improved compared to that of pure CuP_2 as shown in Figure 6.17. The CuP_2/C hybrid electrode delivers desodiation capacities of ~ 481, ~ 469, ~ 443, ~ 390, ~ 308 mA h g^{-1}, respectively, at current densities of 50, 100, 200, 400, and 800 mA g^{-1}. When the current density is decreased to 50 mA g^{-1} after 50 cycles, a reversible capacity of ~ 481 mA h g^{-1} can be recovered, illustrating excellent rate performance. Long-term cycle performance was also compared at higher current densities (Figure 6.18). The CuP_2/C hybrid electrode still maintains stable reversible capacities of ~ 321 mA h g^{-1} at 500 mA g^{-1} and ~ 183 mA h g^{-1} at 1000 mA g^{-1} after 100 cycles with high Coulombic efficiency values of > 99.6%, demonstrating the superior high-rate cyclability of the hybrid electrode.

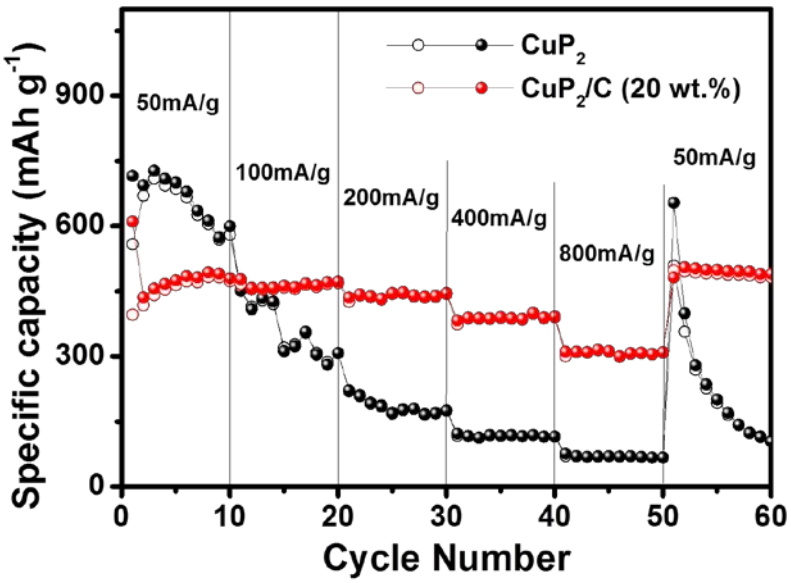

Figure 6.17. Comparison of the rate capability of the pure CuP_2 and CuP_2/C hybrid electrodes. The specific capacity was presented based on the total mass of the hybrid material including carbon.

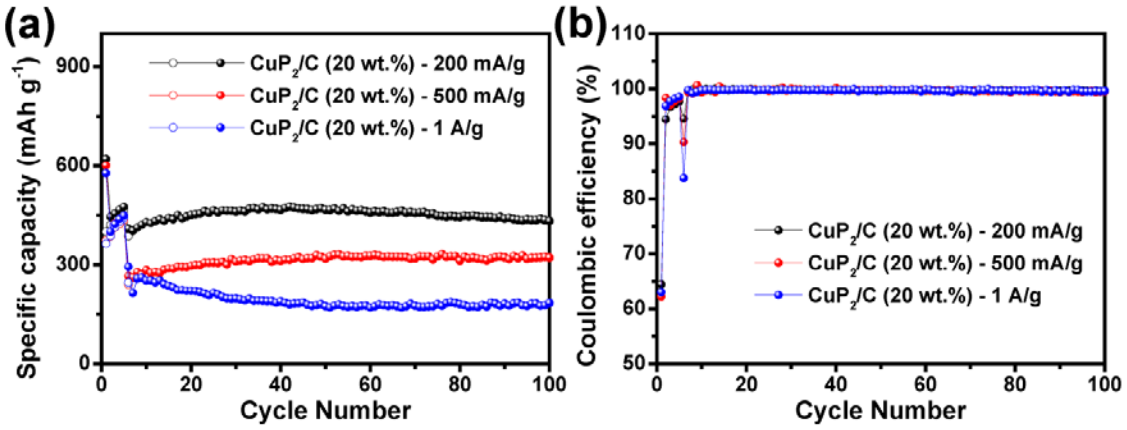

Figure 6.18. Comparison of the (a) cycle performance and (b) corresponding coulombic efficiency of the CuP_2/C hybrid electrodes at various current densities. The cells were tested at 50 mA g^{-1} for the initial 5 cycles for activation.

6.4. CONCLUSION

In summary, phase-pure crystalline CuP_2 and its carbon hybrid (CuP_2/C) have been successfully synthesized by a facile, scalable, and inexpensive mechanical-milling process. By virtue of the unique hybrid architecture composed of nanoscale CuP_2 particles homogeneously dispersed in the conductive carbon network with stable P–O–C chemical bonding, the hybrid electrode not only has a high tap density of ~ 1.2 g cm^{-3}, but also demonstrates superior sodium-storage performance in terms of a high reversible capacity of > 450 mA h g^{-1} at 50 mA g^{-1} with nearly 100% capacity retention up to 100 cycles and a good rate capability with 64% desodiation capacity delivered at 800 mA g^{-1}. The CuP_2/C hybrid can, therefore, be regarded as a promising anode material for sodium-ion batteries and our simple and practical synthetic strategy could also be utilized to design and develop other hybrid anode systems for energy-storage devices.

Chapter 7: High-Performance Red Phosphorus-based P–TiP_2–C Nanocomposite Anode for Lithium-Ion and Sodium-Ion Storage

7.1. INTRODUCTION

With ever-increasing global demand for energy, development of low-cost and high-energy power sources has greatly accelerated in recent years. Among the various energy-storage devices, lithium-ion batteries with a high energy density and long cycle life have played a critical role in utilizing a variety of portable electronics and electric vehicles.[136, 137] While numerous efforts have been devoted to replace graphite with high-capacity alloy-based anode materials, the successful replacement has been hindered by the volume change issues of these alloy anodes occurring during cycling.

In the midst of research for high-performance lithium-ion batteries, sodium-ion batteries have attracted significant attention as a possible alternative to current lithium-ion batteries due to the low cost and natural abundance of sodium sources.[50, 138] Although some progress has been made in improving their electrochemical properties, the larger size of sodium ion (1.02 Å) compared to that of lithium ion (0.76 Å) aggravates the problems associated with sodium insertion/extraction including huge volume change and sluggish sodium-ion diffusion kinetics,[41] which hinder the successful utilization of these candidates.

Elemental phosphorus is of great interest as it shows high theoretical capacity of 2595 mA h g^{-1} in both lithium- and sodium-ion batteries, based on the formation of Li_3P and Na_3P.[38, 39, 63, 139] However, as mentioned in Chapter 1, large volume change and low conductivity issues are required to be overcome in order for phosphorus to be a viable anode material. Two main approaches were introduced as promising ways to improve electrochemical performance of phosphorus-based composites: the carbon composite and metal phosphide systems. Specifically, the carbon composites can not only accommodate

huge volume expansion during cycling, but also provide high powder conductivity, resulting in improved lithium- and sodium-ion storage performance. All of these phosphorus-carbon composites are, however, unsatisfactory for practical applications because they generally require the use of large amounts of carbon (> 30 wt. %) in order to achieve reasonably good cycling stability and rate capability, resulting in low initial Coulombic efficiency and low tap density of the composite materials. Hence, the use of a non-carbonaceous matrix combined with carbonaceous counterpart is considered to be an effective way of addressing the aforementioned problems by reducing the carbon content in the composite.

Herein, we report, for the first time, a phosphorus-based composite (hereafter referred to as "P–TiP_2–C composite") containing a non-carbonaceous structure-reinforcing buffer matrix and its electrochemical behaviors as an anode for lithium- and sodium-ion batteries. Crystalline TiP_2 phase is used as the buffer material because of its ease of synthesis and higher conductivity than phosphorus itself. The facile and simple introduction of crystalline TiP_2 into red phosphorus anode offers a strong buffering effect to mitigate the large volume change upon cycling as well as enhanced powder conductivity. This leads to a significantly improved electrochemical performance of the P–TiP_2–C composite in terms of a high reversible capacity with long cycling stability, high initial Coulombic efficiency, and good rate capability

7.2. EXPERIMENTAL

7.2.1. Sample Preparation

The P–TiP_2–C composites were prepared via a high-energy mechanical milling (HEMM) method with a planetary ball mill apparatus (Pulverisette 5, Fritsch). The precursors used for the synthesis were red phosphorus (98+%, Alfa Aesar), titanium

(99.99%, –325 mesh, Alfa Aesar), and acetylene black carbon (–200 mesh, Alfa Aesar) powders. Stoichiometric amounts of titanium and red phosphorus (atomic ratios of 1 : x, where x = 3, 4, 5, and 6) were first mixed with 20 wt. % of carbon. Then, the mixture was placed in a hardened stainless steel vial (80 cm^3) with hardened steel balls (ball-to-powder weight ratio was 35 : 1) and sealed in an argon-filled glove box. The HEMM was conducted at a rotation speed of 500 rpm for 24 h at room temperature. The mechanochemical reaction occurring during the one-step HEMM process is the formation of conductive TiP_2 as shown below:

$$Ti + x\ P + C \rightarrow TiP_2 + (x - 2)\ P + C \qquad (7.1)$$

The final products were collected, ground, and stored in the glove box to minimize surface oxidation. Based on preliminary electrochemical tests in both lithium- and sodium-ion batteries (Figure 7.1), the optimum mixing ratio of titanium and red phosphorus was found to be 1 : 4 (x = 4 in reaction (7.1) above) in terms of the capacity retention. Therefore, all the data analyzed and discussed here refer to the P–TiP_2–C composite with x = 4 unless otherwise specified. For a comparison, a phosphorus–carbon (P–C) composite (weight ratio of 8 : 2) and pure TiP_2 (x = 2 in equation (7.1) above) were also prepared under the same condition.

7.2.2. Sample Characterization

Powder X-ray diffraction (XRD) measurement was carried out with a Rigaku X-ray diffractometer (MiniFlex 600) with Cu Kα (λ = 1.54059 Å) radiation. The chemical states of the as-synthesized phosphorus-based composites (P–C and P–TiP_2–C) were investigated with a Kratos X-ray photoelectron spectrometer. A Quantachrome AT–4 Autotap machine was used to estimate the tap density of the composite samples. Scanning electron microscopy - energy dispersive X-ray spectroscopy (SEM-EDS, JEOL

JSM–5610), high resolution transmission electron microscopy (HRTEM, JEOL 2010F), and scanning transmission electron microscopy (STEM, Hitachi S–5500) were utilized to observe the microstructure and particle morphology of the composite samples.

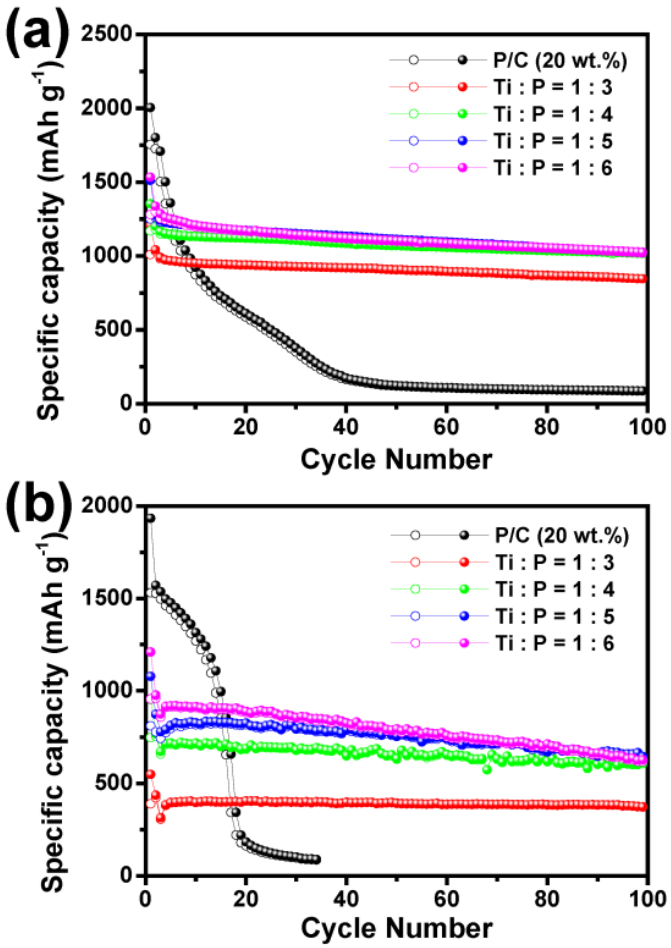

Figure 7.1. Comparison of cycle performance of the phosphorus-based composites tested in (a) lithium half cells at a current density of 200 mA g^{-1} within a voltage range of 0.0 – 2.0V (vs. Li / Li^+) and (b) sodium half cells at a current density of 200 mA g^{-1} within a voltage range of 0.0 – 1.5V (vs. Na / Na^+).

7.2.3. Electrochemical Measurements

The electrodes were prepared by mixing slurries containing 70 wt. % active material, 15 wt. % Super P, and 15 wt. % poly(acrylic) acid (PAA) binder (average MW ~250,000, Aldrich) dissolved in distilled water, coating onto a copper foil substrate, then drying in a vacuum oven at 120 ^{o}C for 8 h. The electrodes were punched into disks (diameter of 1.2 cm) with a typical active material loading of 1.5 ~ 2.0 mg cm^{-2}. CR2032 type coin cells were assembled in the argon-filled glove box with a polypropylene (Celgard 2500) separator and a lithium- or sodium-metal counter electrode. The electrolytes used for lithium-ion and sodium-ion battery tests were, respectively, 1 M $LiPF_6$ and 1 M $NaClO_4$ dissolved in ethylene carbonate (EC) / diethyl carbonate (DEC) (50 : 50 vol. %) with the addition of 5 vol. % of fluoroethylene carbonate (FEC) additive. The galvanostatic charge-discharge experiment was performed with an Arbin battery cycler within a voltage range of 0.0 – 2.0 V (vs. Li / Li^+) for lithium-ion battery and 0.0 – 1.5 V (vs. Na / Na^+) for sodium-ion battery tests. The specific capacity was calculated based on the total weight of the active materials including phosphorus, TiP_2, and carbon in the electrode. Electrochemical impedance spectroscopy (EIS) was performed with an impedance/gain-phase analyzer (Solartron SI 1260) connected with an electrochemical interface (Solartron SI 1286). The EIS curves were obtained with ac amplitude of 5 mV over the frequency range from 100 kHz to 0.1 Hz.

7.3. RESULTS AND DISCUSSION

7.3.1. Structure and Morphology

Figure 7.2 compares the XRD patterns of the commercial red phosphorus, P–TiP_2–C composite, and pure TiP_2. Red phosphorus has an amorphous network and, therefore, shows three broad peaks centered at ~ 15.8, ~ 33.8, and ~ 58^{o}. The XRD

pattern of pure TiP_2 obtained by ball milling for 24 h showed several sharp peaks corresponding to crystalline TiP_2 (JCPDS No. 73-1835, orthorhombic, space group: P*nma*) without the Ti peaks, indicating the complete formation of conductive TiP_2 phase among the various Ti–P binary phases during ball milling. In the case of P–TiP_2–C composite, all the sharp diffraction peaks matched well with the crystalline TiP_2 phase. The presence of a broad peak appeared at ~ 15.8^o revealed that red phosphorus retained its amorphous form even after the HEMM. The samples prepared with the different Ti : P mixing ratios also showed exactly the same characteristic XRD patterns as shown in Figure 7.3. The only difference that can be observed is the intensity of the broad peak at ~ 15.8^o, which increases with the increasing amount of amorphous red phosphorus in the composites.

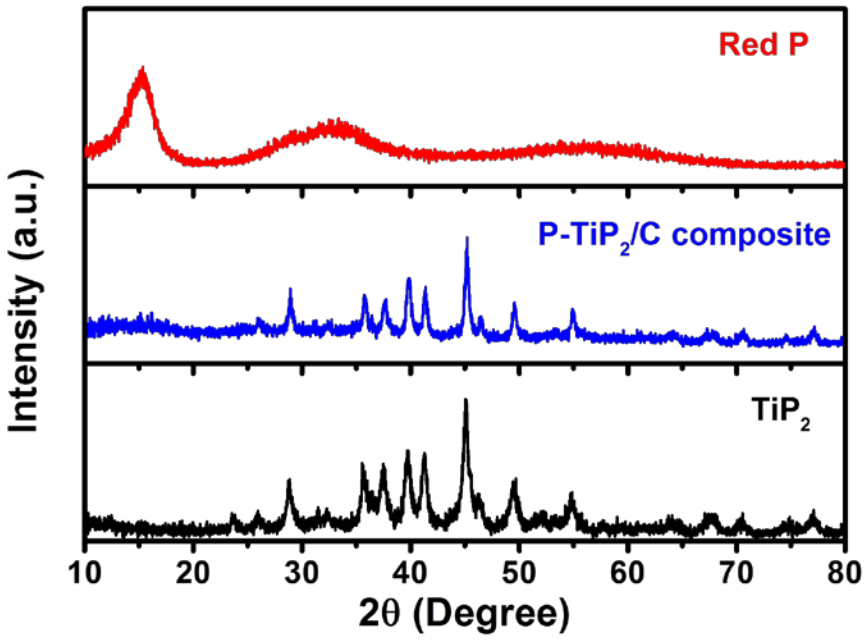

Figure 7.2. XRD patterns of the red phosphorus, P–TiP_2–C composite, and pure TiP_2.

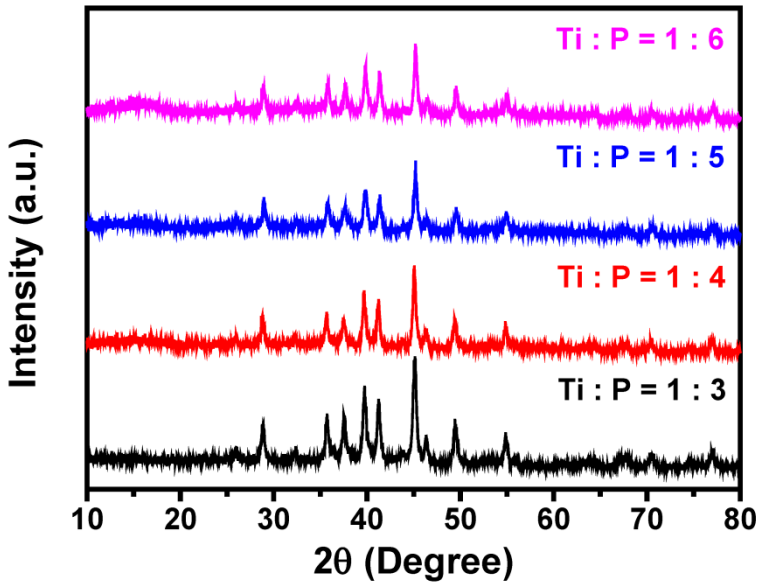

Figure 7.3. XRD patterns of the phosphorus-based composites with different amounts of conductive TiP_2.

XPS measurement was carried out with the P–C and P–TiP_2–C composites to further confirm the presence of Ti–P chemical bonding during ball milling (Figure 7.4). Both samples exhibit identical spectra except for the Ti 2p region in the XPS survey spectra (Figure 7.5a). The P 2p spectrum of the P–TiP_2–C composite can be deconvoluted into three peaks (Figure 7.4a). The first two binding energies at ~ 129.8 and ~ 130.7 eV correspond to, respectively, P $2p_{3/2}$ and P $2p_{1/2}$ of pure phosphorus and, therefore, indicative of the presence of amorphous red phosphorus in the composite.[64] Interestingly, no other peaks related to TiP_2 phase are detected when compared with the P 2p spectrum of the P–C composite (Figure 7.5b). It is believed that the P $2p_{3/2}$ and P $2p_{1/2}$ peaks of TiP_2 are almost overlapped with those of pure phosphorus. The third peak at ~ 134.5 eV is attributed to the phosphates possibly formed on the surface of the particles by air exposure,[64, 140] which is also observable for the P–C composite. The Ti $2p_{3/2}$ spectrum in Figure 7.4b shows two separate peaks appearing at ~ 460.8 and ~ 458.9 eV that are

identified as, respectively, Ti–P and Ti–O chemical bonds.[141] In addition, there are three peaks at ~ 286.3 (C–O), ~ 285.3 (C–C, sp^3), and ~ 284.5 eV (C=C, sp^2) shown in the C 1s spectrum of the P–TiP_2–C composite (Figure 7.5c) without any peaks corresponding to TiC, which suggests that the acetylene black carbon remained intact after the HEMM. Combined XRD and XPS results are suggestive of the coexistence of amorphous phosphorus and crystalline TiP_2 along with acetylene black carbon in the micro-sized phosphorus-based composite.

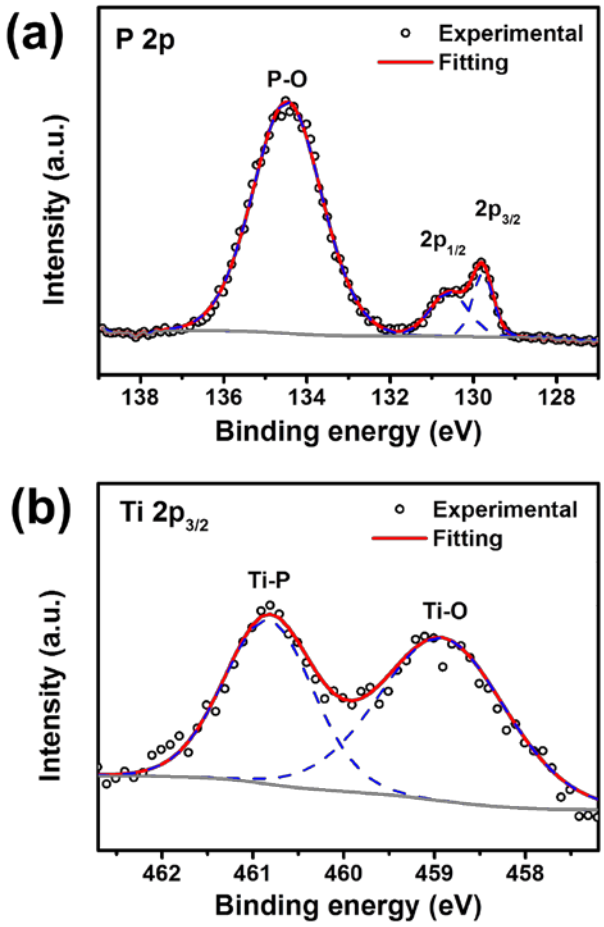

Figure 7.4. XPS spectra in the regions of (b) P 2p and (c) Ti $2p_{3/2}$ of the P–TiP_2–C composite.

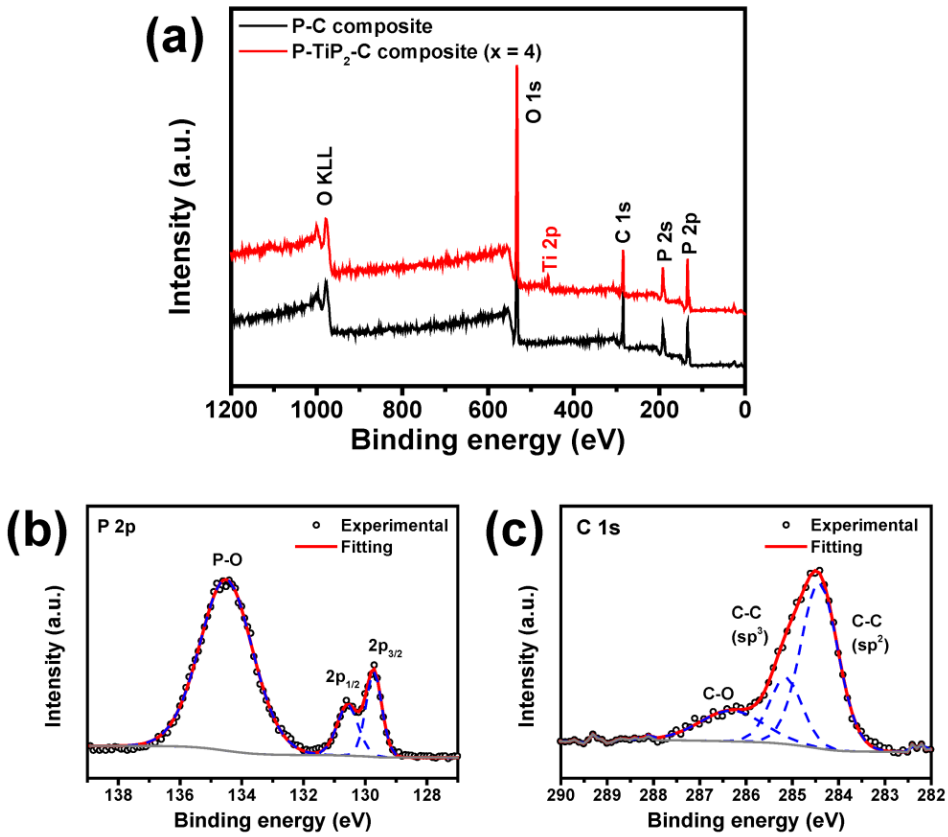

Figure 7.5. (a) XPS survey spectra of the P–C and P–TiP_2–C composites. XPS peak fitting results of (b) P 2p spectrum in the P–C composite and (c) C 1s spectrum in the P–TiP_2–C composite.

The particle morphology and microstructure of the P–TiP_2–C composites were characterized by SEM and HRTEM. Figure 7.6a shows a representative SEM image of the P–TiP_2–C composite. The composite particles are significantly smaller than the commercial red phosphorus (Figure 7.7), with an average particle size of less than 5 μm. The decrease in the particle size is mainly attributed to the continuous fracture and welding processes during HEMM,[110] and is expected to improve the electrochemical reversibility and rate capability when used as an anode in lithium- and sodium-ion batteries.

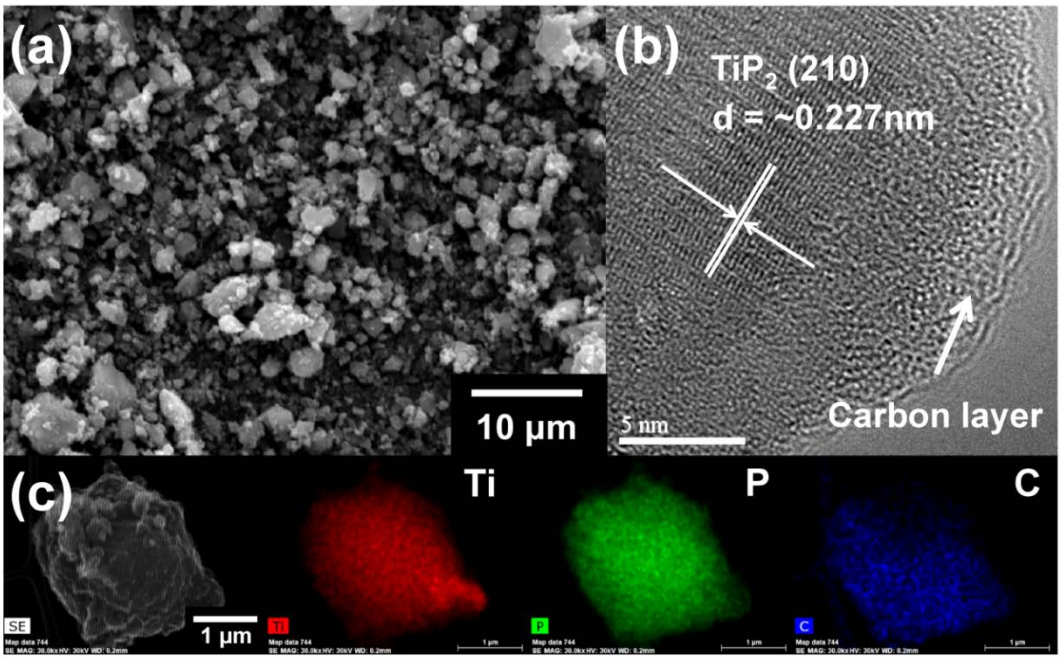

Figure 7.6. (a) SEM, (b) HR-TEM, and (c) STEM images of the P–TiP_2–C composite. In STEM, the corresponding EDS mapping images of each element are indicated (titanium: red, phosphorus: green, and carbon: blue).

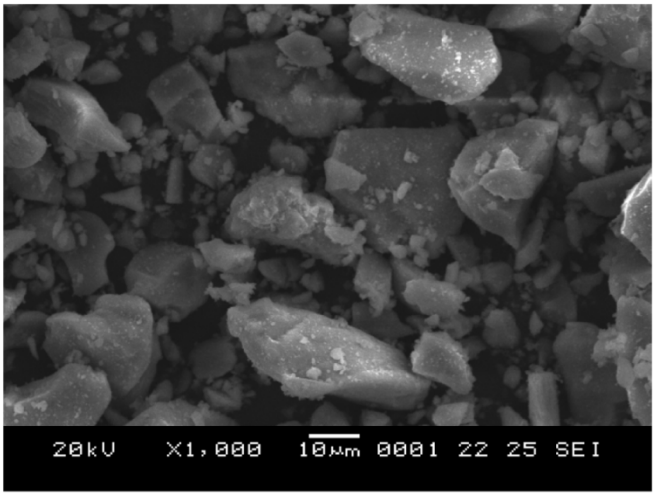

Figure 7.7. SEM image of red phosphorus precursor used for the synthesis.

Based on the SEM/EDS data (Figure 7.8), the approximate amounts of phosphorus, TiP_2, and carbon in the final products were estimated to be, respectively, ~ 28.2, ~ 51.8, and ~ 20.0 wt. %. The micro-sized nature of the P–TiP_2–C composite gives a high tap density of around 1.0 g cm^{-3}, which is comparable to that of graphite (~ 1.0 g cm^{-3})[75, 132] used in lithium-ion batteries and much higher than that of hard carbons (0.50 ~ 0.81 g cm^{-3})[41, 131] used for sodium-ion batteries. It should be noted that such a reasonably high tap density could lead to an improvement in the volumetric and areal capacities that are essential for commercialization. According to the TEM image (Figure 7.9), the micro-sized composite particles seem to consist of agglomerated nanoparticles containing amorphous phosphorus, crystalline TiP_2, and carbon. The HRTEM image presented in Figure 7.6b shows a nanocrystallite with an interplanar spacing of ~ 0.227 nm that corresponds to (210) plane of crystalline TiP_2 phase. These crystalline TiP_2 particles are well-mixed with amorphous phosphorus and further embedded in carbon layers. The STEM and corresponding EDS mapping images (Figure 7.6c) confirm that amorphous phosphorus, crystalline TiP_2, and carbon have a uniform distribution among the composite particles, which is expected to provide improved powder conductivity along with a strong buffering effect against large volume changes during cycling.

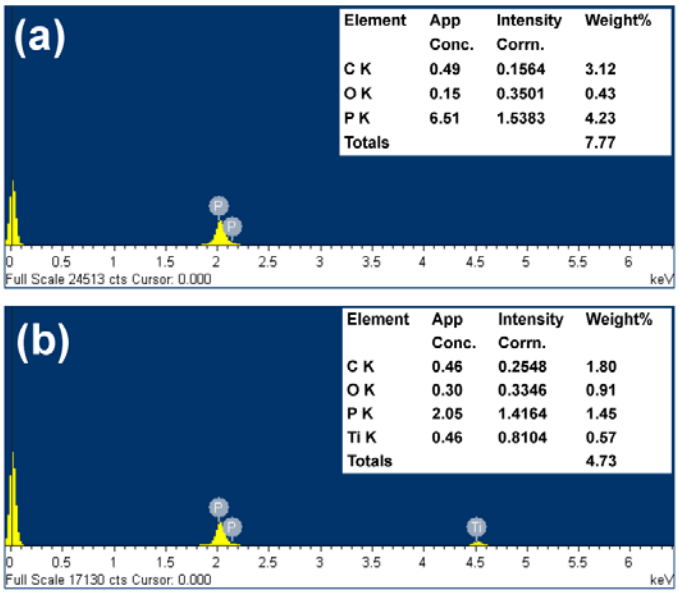

Figure 7.8. SEM/EDS results of (a) the P–C and (b) P–TiP_2–C composites.

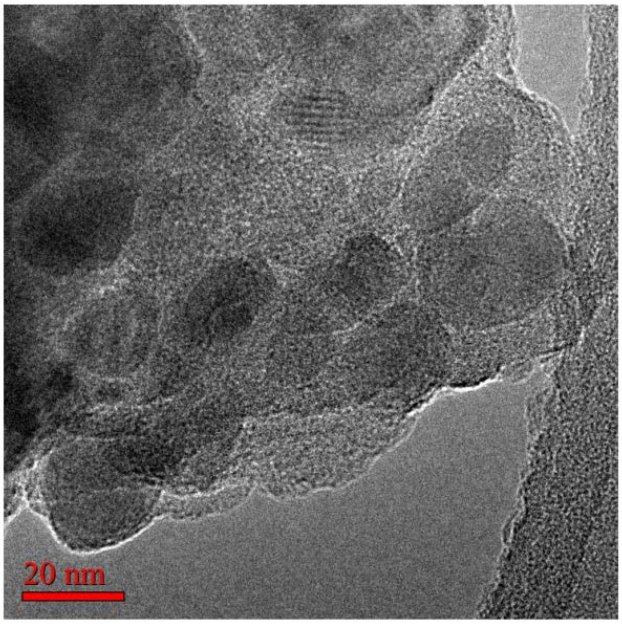

Figure 7.9. Low magnification TEM image of the P–TiP_2–C composite.

7.3.2. Electrochemical Characterization in Lithium Half Cells

To evaluate the electrochemical performance of the phosphorus-based composite anodes in lithium-ion batteries, galvanostatic charge and discharge tests were performed within a voltage range of 0.0 to 2.0 V (vs. Li / Li^+). Figure 7.10a and b show the voltage profiles of the P–C and P–TiP_2–C composites at a current density of 100 mA g^{-1}. Both electrodes exhibit two sloping profiles located at 0.5 – 0.9 V upon discharge (lithiation) step and at 1.0 – 1.2 V upon the following charge (delithiation) process, showing the typical reaction characteristics between phosphorus and lithium.[40, 43, 47] The P–C composite electrode delivers the initial discharge and charge capacities of, respectively, 2006 and 1756 mA h g^{-1} with a very high Coulombic efficiency of ~ 87.5% (Figure 7.10a). Note that these specific capacities are estimated based on the total weight of the composites. Considering that the amount of phosphorus is ~ 80 wt. % in the composite, the capacity contribution from phosphorus is estimated to be ~ 2508 mA h g^{-1}, which is almost close to the theoretical capacity of phosphorus (2595 mA h g^{-1}). However, the reversible capacity decreases rapidly on subsequent cycling and remains only at 874 mA h g^{-1} after 10 cycles. On the other hand, the P–TiP_2–C composite displays much improved cycling stability as shown in Figure 7.10b. The first lithiation and delithiation capacities are, respectively, 1296 and 1116 mA h g^{-1}, with a corresponding Coulombic efficiency of as high as ~ 86.1%. The sloping voltage profiles are well overlapped in the following cycles and it still delivers a reversible capacity of 1139 mA h g^{-1} after 10 cycles, suggesting that the presence of crystalline TiP_2 plays an important role in enhancing the electrochemical reversibility and capacity retention of red phosphorus anode.

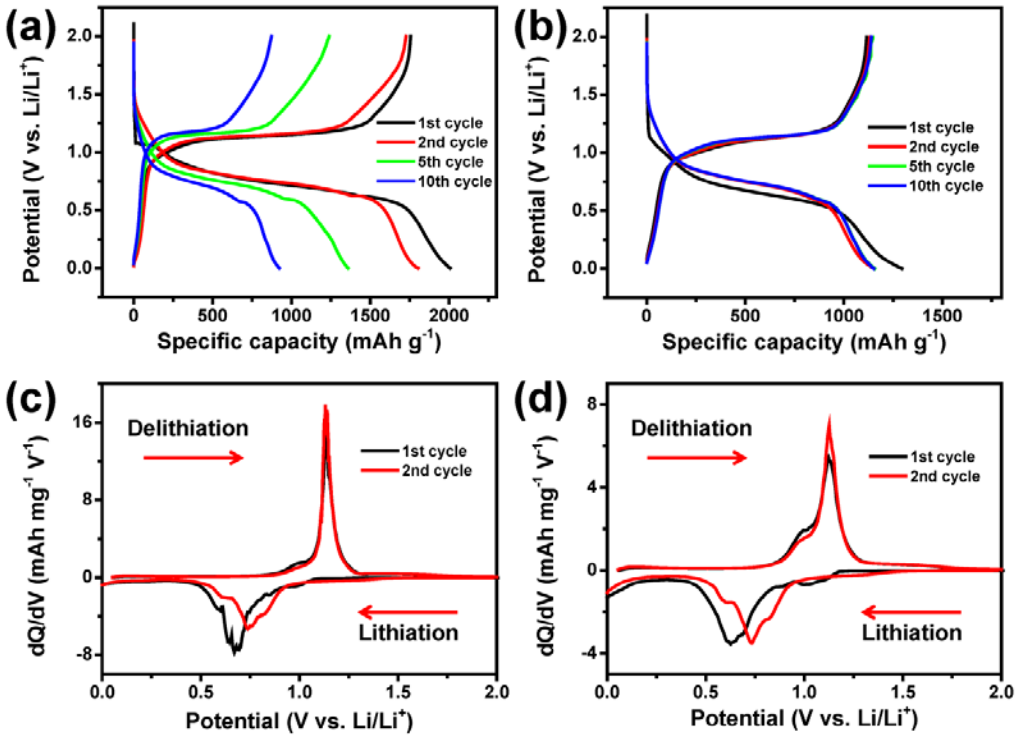

Figure 7.10. Voltage profiles of the (a) P–C and (b) P–TiP_2–C composites and differential capacity plots of the (c) P–C and (d) P–TiP_2–C composites at various cycles tested in lithium half cells (voltage window of 0.0 – 2.0 V (vs. Li / Li^+)).

To better investigate the reaction mechanism, the differential capacity plots (DCPs) of the phosphorus-based composites with and without conductive TiP_2 at initial two cycles are presented in Figure 7.10c and d. As expected from the voltage profiles in Figure 7.10a, the P–C composite shows one broad peak located in the range of 0.5 – 0.9 V during the first discharge, which is associated with the continuous lithium-ion insertion into phosphorus, forming the Li_xP binary alloys (x = 0 – 3).[39, 40, 142] Upon the first charge, a small peak centered at ~ 1.0 V and a sharp peak positioned at ~ 1.12 V are observed, corresponding to the successive delithiation reactions from the Li_xP binary alloys.[39, 40, 142]

In the subsequent cycle, the broad peak occurring during discharge shifts toward higher potential due to the reduced electrode polarization, whereas the charge process takes place at the same potential as that in the first cycle. The first cycle DCP curves of the P–TiP_2–C composite are very similar to those of the P–C composite, except that the shoulders located at ~ 0.5 V during the discharge and at ~ 1.0 V during the charge process become dominant (Figure 7.10d). This indicates that the electrochemical behaviors of the P–TiP_2–C composite are mainly due to the reactions between lithium and phosphorus in the composite. The additional peaks can be ascribed to the lithium insertion and extraction reactions of TiP_2 as confirmed by the DCP profile of the pure TiP_2 (Figure 7.11). According to the literature,[143-146] crystalline TiP_2 has electrochemical reactivity toward lithium, reversibly yielding the Li–Ti–P ternary phases (Li_xTiP_4, $x < 11$) by taking two moles of phosphorus upon repeated cycling. Therefore, amorphous phosphorus in the composite mostly participated in the lithium-phosphorus alloying reactions and the remaining phosphorus is involved in the Li–Ti–P ternary phase evolution. It is worth mentioning that the formation of the Li_xTiP_4 phases could not only contribute to the reversible capacity of the composite, but also act as the buffering matrix against large volume change associated with the lithium-phosphorus alloying reactions due to the structural stability of the Li–Ti–P ternary phases.

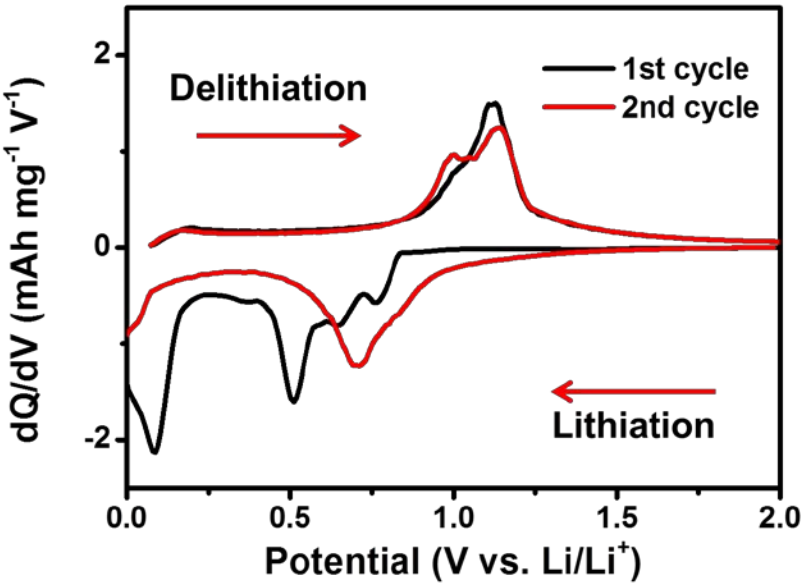

Figure 7.11. The first and second cycle DCP curves of the pure TiP_2 electrode tested in a lithium half cell.

Ex situ XRD analyses were further performed on the P–C and P–TiP_2–C composite anodes at fully lithiated (0 V vs. Li / Li^+) and fully delithiated states (2.0 V vs. Li / Li^+) in the first two cycles in order to compare the structural variation during the initial two cycles. As shown in Figure 7.12a, amorphous phosphorus in the P–C composite starts to react with lithium during discharge and is consequently converted to the fully lithiated compound (Li_3P) at the end of discharge. When charged to 2.0 V, the Li_3P peaks at ~ 23.8^o and ~ 26.8^o disappeared and there are no discernable peaks present in the XRD pattern, indicating that amorphous phosphorus can be reformed upon charging. Structural changes induced by electrochemical reactions show the same trend in the following cycle, as can be seen in Figure 7.12a. In the case of P–TiP_2–C composite (Figure 7.12b), the characteristic peaks of crystalline TiP_2 are clearly observed before the electrochemical test. However, these peaks are no longer observed at the fully discharged

state (0 V) due to the formation of the cubic Li–Ti–P ternary phases resulting from lithium insertion into the orthorhombic TiP_2.

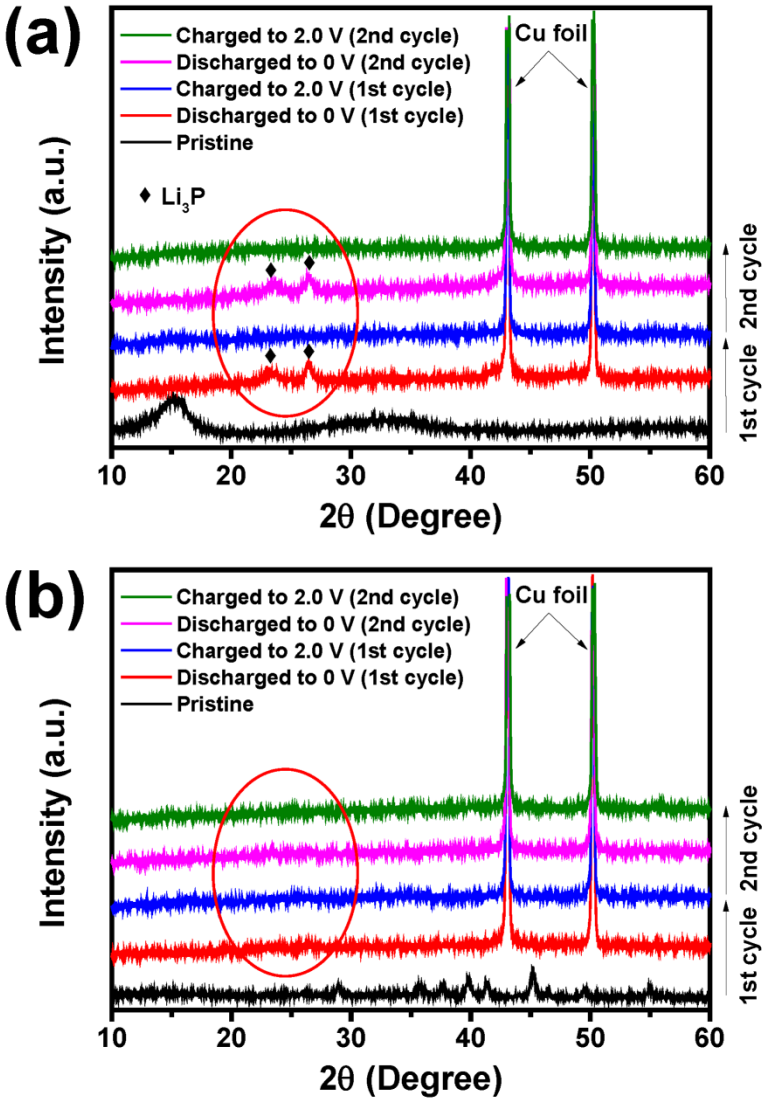

Figure 7.12. The first and second cycle DCP curves of the pure TiP_2 electrode tested in a (a) lithium half cell and (b) sodium half cell.

Although the diffraction peaks of Li–Ti–P ternary phases are not shown in Figure 7.12b, a reversible amorphization/recrystallization structural changes can be identified with pure TiP_2 electrode upon cycling (Figure 7.13), which matches well with the previous reports.[145, 146] Besides, it is interesting to note that no peaks related to Li_3P are detected in the XRD pattern even at full lithiation. This is probably because the stable Li–Ti–P ternary phase might act as a durable buffer matrix and thereby, suppressing the phase transformation of amorphous phosphorus into the fully lithiated compound (Li_3P) that causes large volume expansion (~ 300%). Similar phenomenon could also be observed with our previous study on the silicon-based composite anode.[5] The presence of inactive $NiSi_2$ buffer matrix in the composite prevents the active silicon from reaching the fully lithiated phase ($Li_{15}Si_4$). No crystalline phases appeared in the subsequent charge and discharge steps, suggesting that various amorphous Li_xP ($x < 3$) intermediates could be produced during the lithiation and delithiation processes.

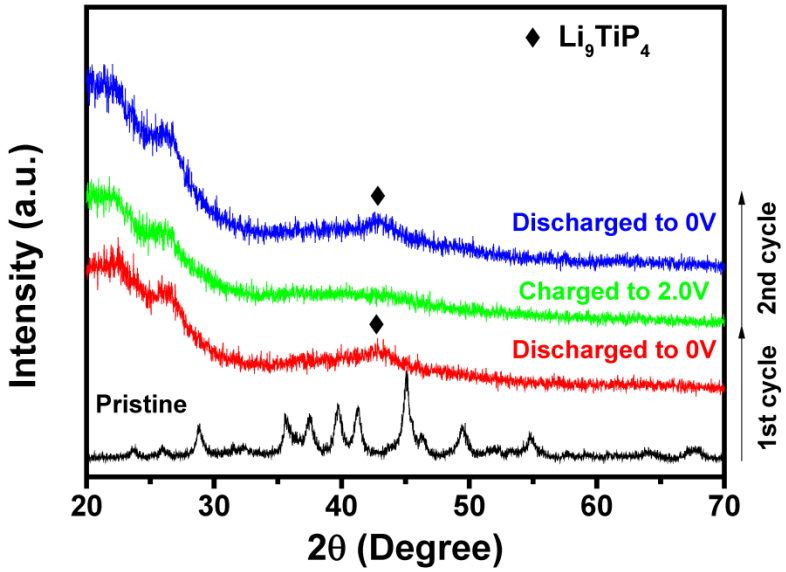

Figure 7.13. *Ex situ* XRD patterns of the pure TiP_2 electrode at various states of charge.

The cycle performance of the phosphorus-based composites is compared in Figure 7.14. All the cells were cycled within a voltage range of 0 – 2.0 V (vs. Li / Li^+) at a current density of 100 mA g^{-1} for the first two cycles for activation and then tested at 200 mA g^{-1}. The P–C composite shows poor electrochemical behavior with severe capacity fading due to the large volume change associated with the Li_3P formation. The reversible capacity was as high as 1755 mA h g^{-1} in the first cycle but it rapidly drops down to 588 mA h g^{-1} only after 20 cycles. In contrast, the P–TiP_2–C composite exhibits good electrochemical reversibility toward lithium and an excellent cycling performance with a high capacity retention of > 87.1% after 100 cycles. After 100 cycles, a reversible capacity of > 1019 mA h g^{-1} is still delivered. Such a high capacity can be achieved since both amorphous phosphorus and crystalline TiP_2 contribute to the reversible capacity of the composite, as discussed above. The significantly enhanced cyclability might be attributed to the generation of the stable cubic Li_xTiP_4 phase upon cycling that could provide structural stability to the P–TiP_2–C composite during repeated cycling. Specifically, it is known that the variation of the lithium content in the Li_xTiP_4 phase (x = 6.5 – 10.5) results in < 1 % cell volume change.[144, 146] In addition, the implementation of 5 vol. % FEC-containing electrolyte and PAA binder ensures the performance improvement as they have been regarded, respectively, as an effective electrolyte additive and binder for the phosphorus-based anode systems.[63, 139] The *ex situ* SEM images (Figure 7.15) show the changes in the electrode surface morphology of the phosphorus-based composite electrodes before and after cycling. Although the P–C composite reveals large macrocracks and electrode degradation after 30 cycles, the P–TiP_2–C composite still illustrates a smooth surface morphology even after 50 cycles, further demonstrating the effectiveness of the stable Li_xTiP_4 ternary phase on the mechanical integrity of the electrode during cycling.

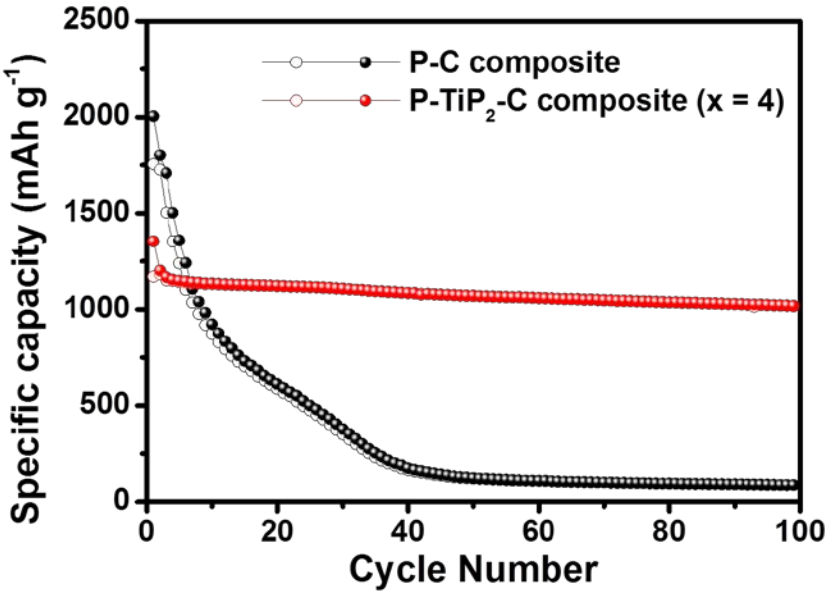

Figure 7.14. Comparison of the cycle performance of the P–C and P–TiP_2–C composite electrodes tested in lithium half cells. The specific capacity was calculated based on the total mass of the composite materials.

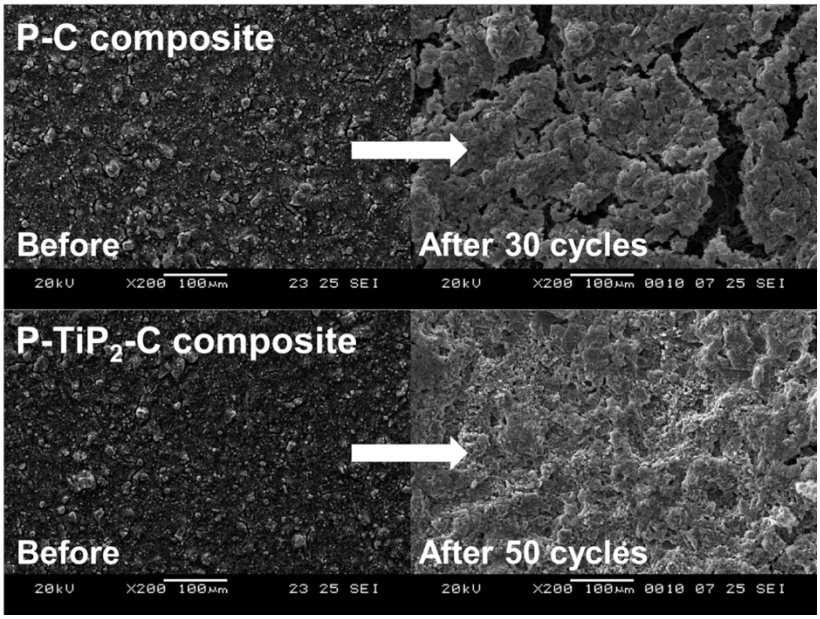

Figure 7.15. Changes in electrode surface morphologies of the P–C and P–TiP_2–C composites as a function of cycle numbers tested in lithium half cells.

The rate capability tests of the phosphorus-based composite electrodes were also performed by varying the current densities. As shown in Figure 7.16, the charge capacities of the P–C composite are ~ 1250, ~ 973, ~ 752, ~ 517, and ~ 290 mA h g^{-1}, respectively, at 200, 400, 800, 1600, and 3200 mA g^{-1}. Only the reversible capacity of ~ 672 mA h g^{-1} can be restored when the current density is lowered to 200 mA g^{-1}, exhibiting poor rate performance. However, the P–TiP_2–C composite can deliver stable delithiation capacities of ~ 1118, ~ 1064, ~ 1027, and ~ 989 mA h g^{-1}, respectively, at 200, 400, 800, and 1600 mA g^{-1}. Surprisingly, the reversible capacity still reaches 919 mA h g^{-1} even at a high rate of 3200 mA g^{-1}, and its capacity is recovered over ~ 1059 mA h g^{-1} at 200 mA g^{-1} after 50 cycles (~ 95% retention of its capacity at the 10th cycle), demonstrating an outstanding rate capability.

The dramatic enhancement of rate performance may be due to the realization of unique nanostructure composed of amorphous phosphorus homogeneously mixed with conductive TiP_2 crystallites well incorporated in the carbon matrix. With the aid of this nanostructure, it is expected that the short diffusion pathway for lithium ions could be achieved by the confinement of nano-sized phosphorus and TiP_2 active particles in durable carbon dispersing matrix, which enables facile lithium-ion transport during repeated fast charge and discharge cycling. The EIS studies (Figure 7.17) further support the enhanced conductivity of the phosphorus-based composite with the TiP_2 phase. Although the charge-transfer resistance (the diameter of the semicircle) of the P–C composite is increased quickly after 30 cycles, the Nyquist plot of the P–TiP_2–C composite after 50 cycles remained unchanged compared to that after 10 cycles.

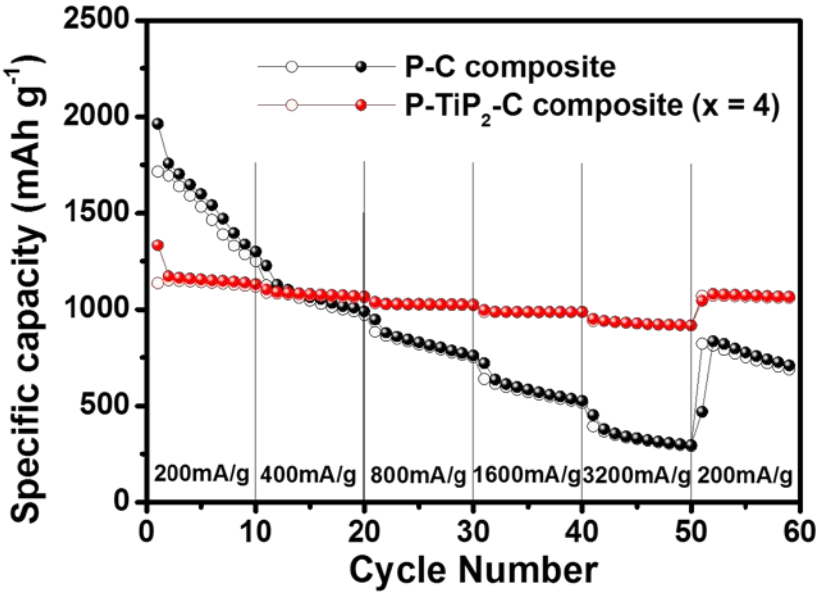

Figure 7.16. Comparison of the rate capability of the P–C and P–TiP_2–C composite electrodes tested in lithium half cells.

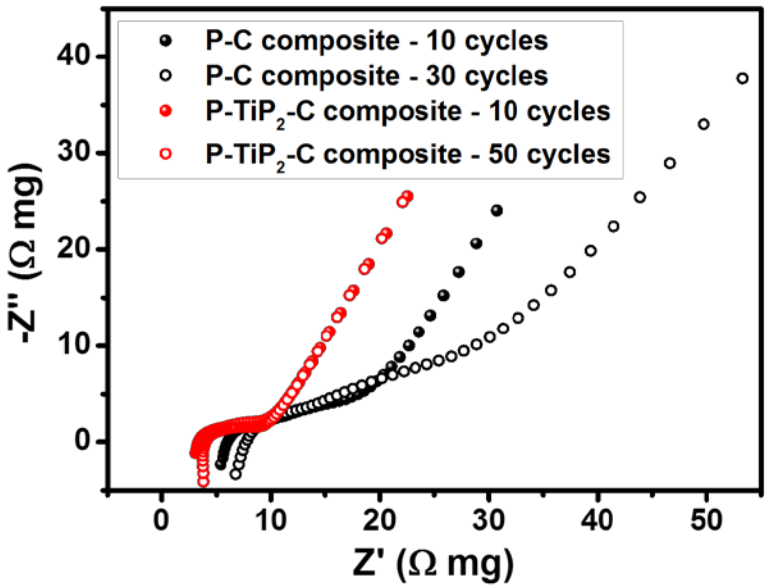

Figure 7.17. Changes in impedance spectra of the P–C and P–TiP_2–C composites as a function of cycle numbers tested in lithium half cells.

7.3.3. Electrochemical Characterization in Sodium Half Cells

The sodium-storage performance of the P–TiP_2–C composite was also assessed by galvanostatic cycling tests between 0 and 1.5 V (vs. Na / Na^+). The discharge and charge profiles of the phosphorus-based composite anodes cycled at 50 mA g^{-1} are illustrated in Figure 7.18a and b. Similar to those obtained in lithium half-cell tests (Figure 7.10a and b), the phosphorus-based composites show the well-defined two sloping profiles appearing in the range of 0.1 – 0.5 V upon sodiation and 0.4 – 0.8 V during the reverse desodiation step, indicating that the sodium-phosphorus alloying reactions are quite analogous to the lithium-phosphorus alloying reactions except that the redox potentials are ~ 0.3 V lower due to the difference in the standard electrode potentials between the Na / Na^+ and Li / Li^+ redox couples. In the case of the P–C composite (Figure 7.18a), the first sodiation and desodiation capacities are, respectively, 1993 and 1532 mA h g^{-1}, with a high Coulombic efficiency of ~ 79.2%. Despite its high initial reversible capacity and Coulombic efficiency, it exhibits severe capacity fade in 10 cycles. The P–TiP_2–C composite delivers initial sodiation and desodiation capacities of, respectively, 947 and 761 mA h g^{-1} (Figure 7.18b). The corresponding initial Coulombic efficiency still reaches ~ 80.3%, indicating that improved electrochemical reversibility could be achieved by the coexistence of conductive TiP_2 phase with amorphous carbon network in the composite. Compared to the case of the P–C composite, sloping potential profiles are well maintained up to 10 cycles with a smaller polarization, which further confirms the highly conducting nature and enhanced capacity retention of the phosphorus-based composite with the TiP_2 phase.

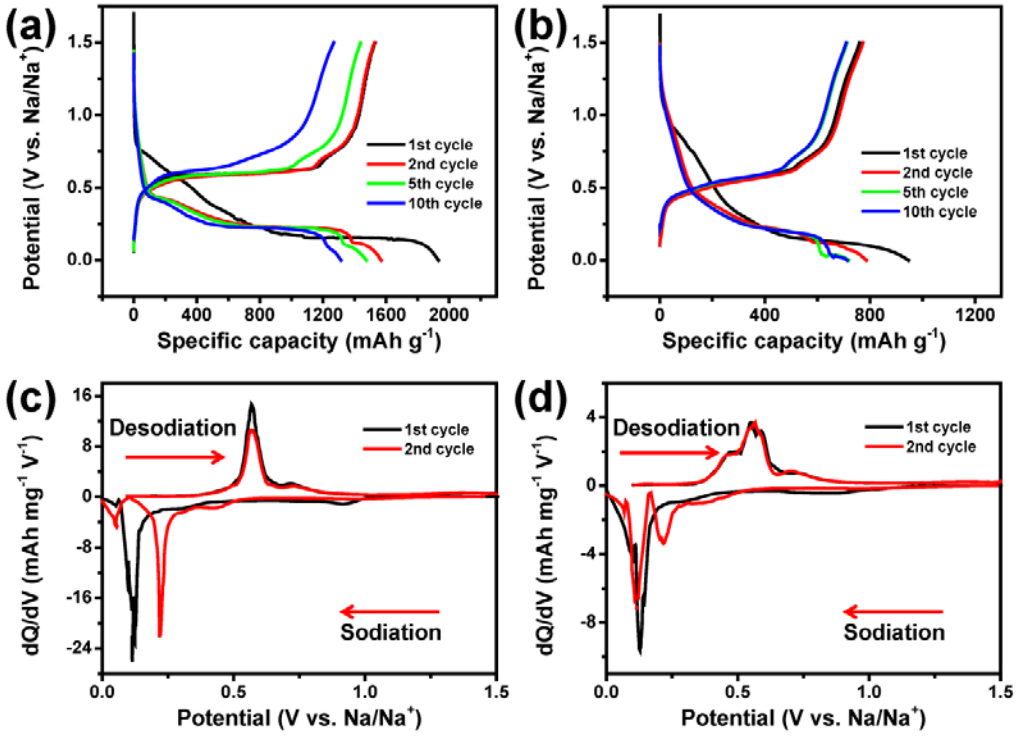

Figure 7.18. Voltage profiles of the (a) P–C and (b) P–TiP_2–C composites and differential capacity plots of the (c) P–C and (d) P–TiP_2–C composites at various cycles tested in sodium half-cells (voltage window of 0.0 – 1.5 V (vs. Na / Na^+)).

The DCP curves of the phosphorus-based composites are presented to understand the detailed reaction mechanism. As shown in Figure 7.15c, the P–C composite displays a sharp peak centered at ~ 0.11 V upon first discharge, which is an indication of the sodium-insertion reactions into phosphorus, eventually forming Na_3P phase.[40, 63, 134] During the following charge, there are a large, sharp peak located at ~ 0.56 V and a small peak at ~ 0.73 V, which are attributed to the stepwise sodium-extraction reactions. [40, 63, 134] While the first sodiation process of the P–TiP_2–C composite seems to be identical to that of the composite without TiP_2 phase (Figure 7.18d), the additional reaction peak at ~

0.47 V can be seen along with two peaks at ~ 0.56 and ~ 0.73 V in the reverse desodiation step. Nevertheless, the extra peak at ~ 0.47 V is obviously not associated with the reaction between the crystalline TiP_2 and sodium, since the TiP_2 is unreactive toward sodium (Figure 7.19), unlike toward lithium. Therefore, it is considered to be the onset of sodium dealloying reaction, which occurs at a lower potential due to the reduced polarization provided by highly conductive network composed of TiP_2 inclusions and carbon buffer as well as the formation of nano-sized amorphous phosphorus in the composite as a result of the HEMM process. In the second discharge and charge processes, broad reaction peaks are maintained, revealing that nano-sized phosphorus undergoes reversible reactions with sodium.

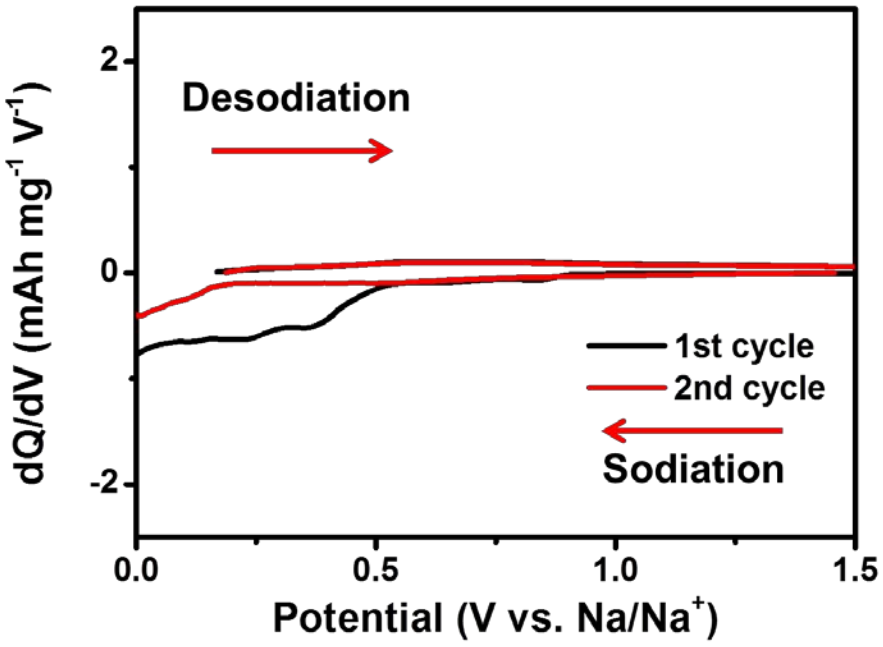

Figure 7.19. The first and second cycle DCP curves of the pure TiP_2 electrode tested in a sodium half cell.

In order to confirm the phase changes during the sodiation and desodiation processes, *ex situ* XRD was also carried out on the P–TiP_2–C composite anode. Figure 7.20 shows the *ex situ* XRD patterns at fully sodiated (0 V vs. Na / Na^+) and fully desodiated states (1.5 V vs. Na / Na^+) in the first and second cycles. All of the diffraction peaks correspond to crystalline TiP_2 phase before the sodiation process. At full sodiation (0 V), the crystalline Na_3P peaks can be observed with the crystalline TiP_2 peaks. This further confirms that there is no reactivity of TiP_2 with sodium, corroborating the DCP studies discussed above. Although the Na_3P peaks completely disappeared at full desodiation (1.5 V), the characteristic peaks of TiP_2 are still detectable, indicating the excellent structural stability during sodiation and desodiation.

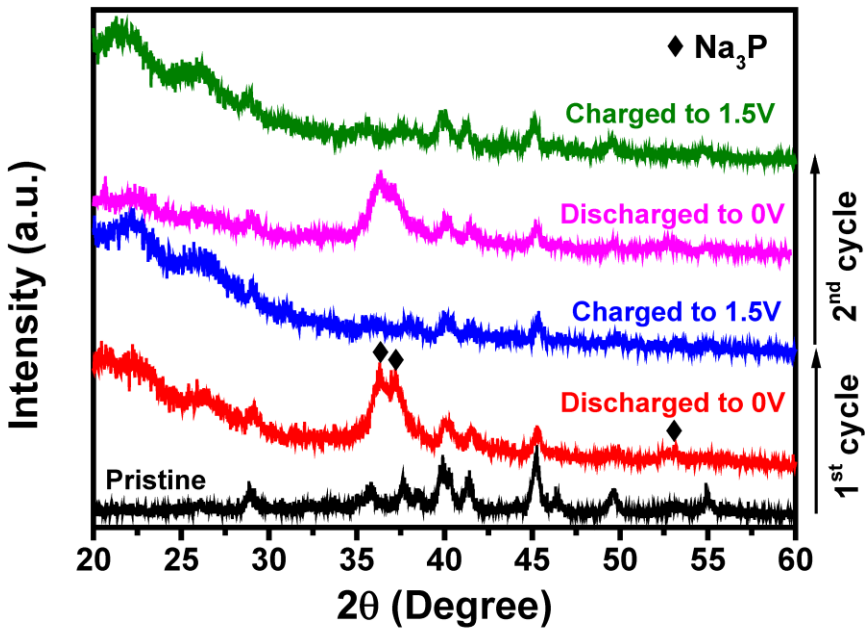

Figure 7.20. *Ex situ* XRD patterns at various states of charge of the P–TiP_2–C composite tested in sodium half cells.

The cycle performance of the phosphorus-based composites is presented in Figure 7.21. All the cells were tested at a current density of 50 mA g^{-1} for the first two cycles for activation and then cycled at 200 mA g^{-1} within a voltage window of 0 – 1.5 V (vs. Na / Na^{+}). The P–C composite anode in sodium half cells shows an initial reversible capacity of ~ 1531 mA h g^{-1}, but it drastically decreases with cycling. A reversible capacity of ~ 97 mA h g^{-1} is remained after 30 cycles, which is only ~ 6.3% of its initial capacity, indicating poor cycleability. This is mainly caused by the Na_3P formation upon sodiation that leads to large volume expansion (~ 490%) of the active material and an eventual mechanical failure and degradation of the electrode. On the other hand, it is remarkable to note that the P–TiP_2–C composite delivers a high initial reversible capacity of ~ 755 mA h g^{-1} with an excellent capacity retention (~ 80.4%) up to 100 cycles. The enhanced cycle performance is ascribed to the presence of highly stable TiP_2 inclusions uniformly mixed with amorphous phosphorus active particles. As discussed above, the TiP_2 phase could remain well-distributed among the composite particles even after repeated electrochemical cycling since the TiP_2 phase has no reactivity toward sodium. Consequently, the TiP_2 phase, in combination with carbon buffer, effectively acts as an inactive reinforcing matrix that alleviates the volume change of amorphous phosphorus and offers better particle connectivity during cycling, resulting in significantly improved cycling stability. The *ex situ* SEM analyses of the phosphorus-based composite electrodes (Figure 7.22) further confirms the beneficial role of the TiP_2 phase for cycling stability. The composite without TiP_2 shows the severe electrode pulverization after 30 cycles; however, the P–TiP_2–C composite maintains a smooth morphology without cracking, indicating enhanced mechanical stability of the active materials.

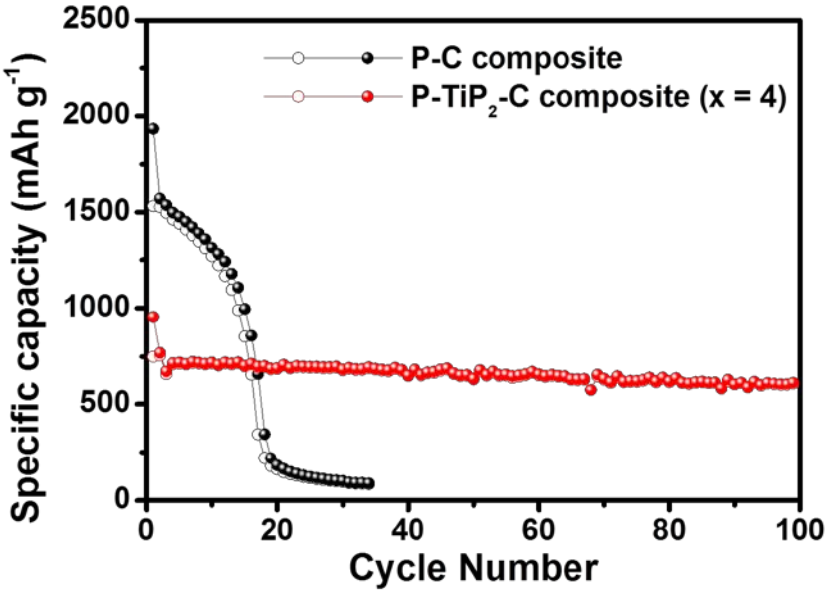

Figure 7.21. Comparison of the cycle performance the P–C and P–TiP_2–C composite electrodes tested in sodium half cells. The specific capacity was calculated based on the total mass of the composite materials.

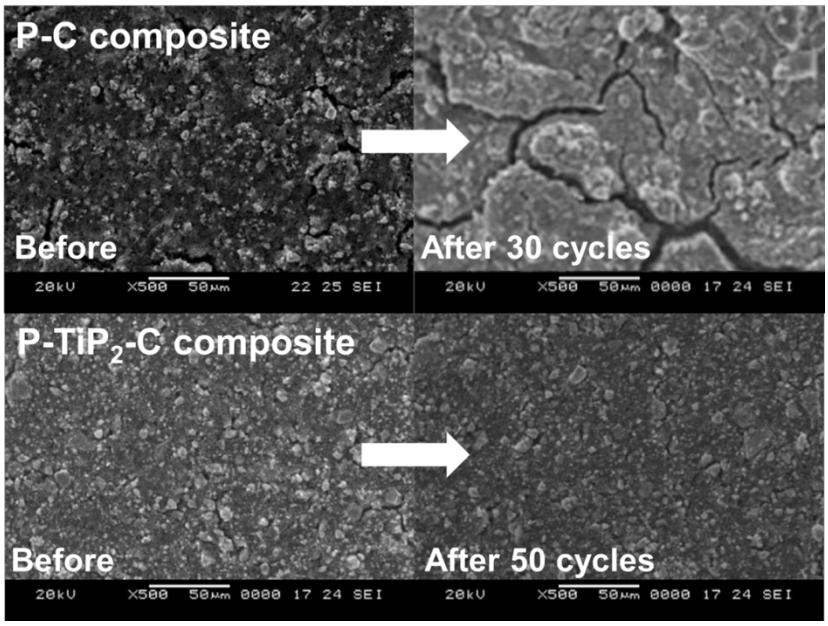

Figure 7.22. Changes in electrode surface morphologies of the P–C and P–TiP_2–C composites as a function of cycle numbers tested in sodium half cells.

The P–TiP_2–C composite exhibits much better rate capability compared to the P–C composite, as can be seen in Figure 7.23. While the desodiation capacities of the P–C composite are ~ 1430, ~ 1248, ~ 979, ~ 639, and ~ 342 mA h g^{-1}, respectively, at 50, 100, 200, 400, and 800 mA g^{-1}, the P–TiP_2–C composite delivers reversible charge capacities of ~ 770, ~ 748, ~ 698, ~ 677, and ~ 526 mA h g^{-1}, respectively, at the same current densities, illustrating much improved rate performance. This result suggests that the formation of well-mixed amorphous phosphorus and conductive TiP_2 embedded in carbon matrix could facilitate the sodiation/desodiation processes by providing good ionic diffusion and electron conducting pathways among the composite particles. This could be further verified by the EIS studies (Figure 7.24). Compared to the phosphorus-based composite without the TiP_2 phase, the P–TiP_2–C composite exhibits significantly lower charge-transfer resistance even after 50 cycles, arising from the maintenance of facile kinetics by preserving the smooth electrode morphology.

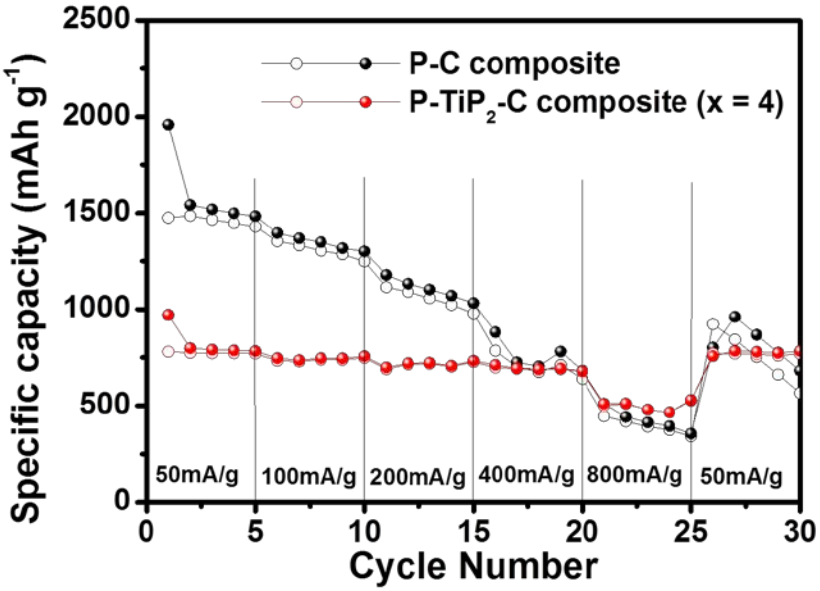

Figure 7.23. Comparison of the rate capability of the P–C and P–TiP_2–C composite electrodes tested in sodium half cells.

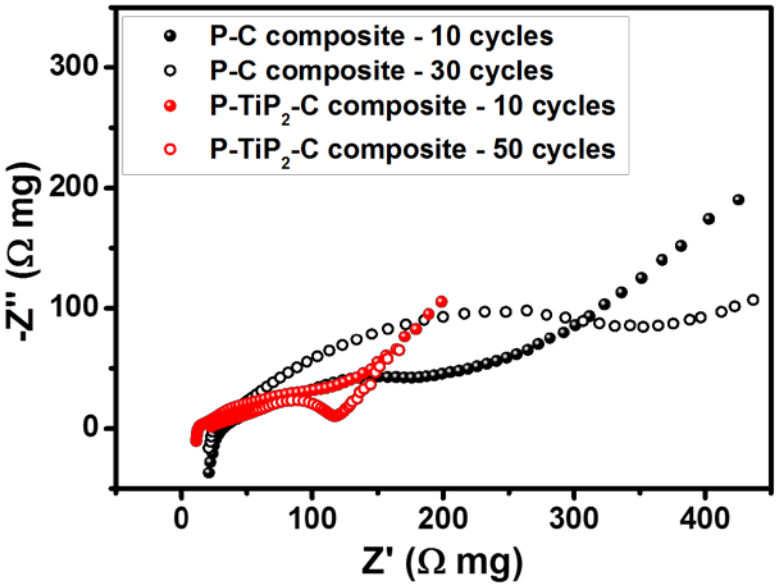

Figure 7.24. Changes in impedance spectra of the P–C and P–TiP_2–C composites as a function of cycle numbers tested in sodium half cells.

7.4. CONCLUSION

Amorphous red phosphorus-based composites with conductive TiP_2 were synthesized through a low cost, facile, eco-friendly HEMM process and employed as an anode in both lithium- and sodium-ion batteries. With a high tap density of ~ 1.0 g cm^{-3}, the P–TiP_2–C composite delivers a high reversible capacity of ~ 1116 mA h g^{-1} (based on the total mass of the composite) with an initial Coulombic efficiency of as high as 86%, outstanding cycling stability (> 87% capacity retention after 100 cycles), and good rate performance in lithium-ion cells. In sodium-ion cells, it also shows the high reversible capacity of ~ 755 mA h g^{-1} (based on the total mass of the composite) with an initial Coulombic efficiency of as high as 80%, excellent cyclability (> 80% capacity retention after 100 cycles), and good rate capability. The significant improvement in electrochemical performance is mainly attributed to the simple incorporation of

crystalline TiP_2 phase that leads to the structural reinforcement by forming stable Li_xTiP_4 active matrix upon lithiation in lithium-ion cells and provides a durable conducting inactive matrix in combination with carbon in sodium-ion cells. Moreover, the unique nanostructure composed of mixed red phosphorus and TiP_2 dispersed in the conductive carbon network further enables rapid electrode kinetics through short ionic diffusion length, buffering of the volume expansion during cycling, and maintenance of the electrochemical reversibility.

Chapter 8: Summary

The aim of this dissertation was to explore and develop low-cost and high-performance alloy anode systems for lithium- and sodium-ion batteries by employing an active/inactive composite strategy. To achieve this goal, the low-cost, simple, and scalable high-energy mechanical milling method was utilized to synthesize the composite anodes. All the composites developed in this research have capacity higher than the graphite anode currently used in commercialized cells with greatly enhanced cycle and rate performance compared to single-phase alloy anodes. In addition, the high tap density of the composites (> 1.0 g cm^{-3}) translates to improved volumetric and areal capacities, particularly important for practical applications.

In Chapter 3, a micro-sized carbon-coated silicon-based composite was developed via two-step mechanochemical reaction. Combined X-ray and microscopic studies showed that the composites are composed of agglomerated nanostructured particles with uniform distribution of crystalline silicon, $NiSi_2$, and amorphous Al_2O_3. The introduction of a two-phase well-intermixed buffer composed of conductive $NiSi_2$ and electrochemically stable Al_2O_3 gives the resultant Si-$NiSi_2$-Al_2O_3 composite a stable reversible capacity of 580 mA h g^{-1} over 200 cycles with a much higher tap density of ~ 1.34 g cm^{-3} compared to nanosized Si (~ 0.16 g cm^{-3}), demonstrating the effectiveness of incorporating the nanoscale silicon active material into a multiphase reinforcing buffer matrix. Upon cycling, the $NiSi_2$ phase not only provides enhanced electronic conductivity but also suppresses the formation of crystalline $Li_{15}Si_4$ that causes an inhomogeneous volume change. Simultaneously, amorphous Al_2O_3 plays a crucial role in maintaining particle connectivity by impeding the agglomeration of active silicon particles. The combination of these advantages with a low-cost, scalable, and environmentally benign

synthetic process make the silicon-based composite a promising alternative anode candidate for lithium-ion batteries.

In Chapter 4, with an aim to increase the practicality of silicon-based composite anode, a carbon-coated Si-Cu_3Si-Al_2O_3 nanocomposite was synthesized by substituting a low-cost copper precursor for a high-cost nickel precursor. The *in situ* incorporation of both conductive Cu_3Si and amorphous Al_2O_3 phases also results in a dramatic improvement of cyclability and rate capability. By controlling the Cu_3Si content, the composite possessing a high reversible capacity of 841 mA h g^{-1}, an excellent cyclability, and good rate performance up to 3.2 A g^{-1} in lithium half cells, while maintaining high tap density of ~ 1.2 g cm^{-3}, could be obtained, which is even superior to the composite with $NiSi_2$ studied in Chapter 3. The enhanced electrochemical performance is mainly attributed to the presence of the conductive Cu_3Si buffer phase that mitigates structural degradation and offers high conductivity. Moreover, a full cell test coupled with a commercial spinel cathode also displays a high average operating voltage of > 3.5 V, a relatively good capacity retention of ~ 77.2 % after 50 cycles with a high initial efficiency of ~ 86.3 %, further demonstrating the feasibility of commercial implementation.

Chapter 5 explored a zinc-based nanocomposite anode for lithium-ion batteries. Structural characterization reveals that the micron-sized Zn–TiC–C nanocomposite is composed of zinc nanocrystals uniformly dispersed in a multifunctional TiC and conductive carbon matrix with a tap density of 1.3 g cm^{-3}. The Zn–TiC–C nanocomposite exhibits high reversible volumetric capacity of 468 mA h cm^{-3}, excellent cyclability over 800 cycles, and good rate performance up to 12.5C. The use of TiC matrix instead of Al_2O_3 is capable of further providing improved conductivity and structural reinforcement due to the highly conductive, mechanically robust nature of the TiC phase, resulting in

enhanced electrochemical performance. In addition, the TiC + C buffer prevents the particle growth by uniformly dispersing nanosized zinc within itself during cycling, maintaining high utilization of nearly 100% and fast reaction kinetics of zinc anode.

In Chapter 6, a chemically bonded CuP_2/C hybrid was introduced as an anode for sodium-ion batteries to examine the effects of a combination of the two promising strategies, making binary metal phosphides and utilizing carbon composites, on the improvement of electrochemical performance of phosphorus anodes. The synergistic effects of the formation of a strong P–O–C bond and the stable nanoscale conducting framework were methodically analyzed. Structural, morphological, and electrochemical characterization demonstrate that the carbon hybrid network, which is chemically bonded to the active CuP_2, plays an important role as a durable embedding matrix that enhances electrode conductivity, accommodates large volume changes, and preserves the mechanical integrity of the active materials during repeated cycling.

In Chapter 7, the active/inactive matrix concept was extended to the high-capacity phosphorus-based anode for both lithium- and sodium-ion batteries. An amorphous red phosphorus-based composite with conductive TiP_2 phase synthesized via one-step mechanical milling exhibits a high reversible capacity of 1116 mA h g^{-1}, excellent cyclability, and a remarkable initial Coulombic efficiency of 86% in lithium half cells. Furthermore, it delivers an initial desodiation capacity of 755 mA h g^{-1} with a high initial Coulombic efficiency of 80% and a good capacity retention of 80% after 100 cycles in sodium half cells. The greatly improved electrochemical performance is due to the unique nanoarchitecture composed of well-blended red phosphorus and crystalline TiP_2 homogeneously embedded in a conductive carbon network. The presence of the conductive TiP_2 inclusions offers structural stability as well as high conductivity to the phosphorus-based composite particles during cycling, thereby leading to superior cycling

stability and rate capability in both lithium- and sodium-ion batteries compared to the composite without TiP_2.

Overall, the successful implementation of alloy-based anodes into lithium- and sodium-ion batteries is quite challenging, but the developed silicon-, zinc-, phosphorus-based composites in this dissertation show great performance improvements in terms of high densities, high capacities, with long cycle lives, and good rate capability, making them promising and desirable anode candidates. The combination of a low-cost, facile, scalable synthesis route and the understanding of the mechanisms of composite anodes with outstanding electrochemical performance may help to design and develop high-performance alloy-based anodes with optimized composition for next generation lithium- and sodium-ion batteries.

Appendix: List of Publications

1. I. T. Kim, S. –O. Kim, and A. Manthiram, “Effect of TiC Addition on SnSb-C Composite Anodes for Sodium-ion Batteries.” *J. Power Sources* **2014**, 269, 848–854.
2. S. –O. Kim and A. Manthiram, “A facile, low-cost synthesis of high-performance silicon-based composite anodes with high tap density for lithium-ion batteries.” *J. Mater. Chem. A* **2015**, 3, 2399–2406.
3. S. –O. Kim and A. Manthiram, “High-Performance Zn–TiC–C Nanocomposite Alloy Anode with Exceptional Cycle Life for Lithium-Ion Batteries.” *ACS Appl. Mater. Interfaces* **2015**, 7, 14801–14807.
4. E. Allcorn, S. –O. Kim, and A. Manthiram, “Thermal stability of active/inactive nanocomposite anodes based on Cu_2Sb in lithium-ion batteries.” *J. Power Sources* **2015**, 299, 501–508.
5. E. Allcorn, S. –O. Kim, and A. Manthiram, “Lithium diffusivity in antimony-based intermetallic and FeSb–TiC composite anodes as measured by GITT.” *Phys. Chem. Chem. Phys.* **2015**, 17, 28837–28843
6. S. –O. Kim and A. Manthiram, “The facile synthesis and enhanced sodium-storage performance of a chemically bonded CuP_2/C hybrid anode.” *Chem. Commun.* **2016**, 52, 4337–4340.
7. Y. Li, M. P. Paranthaman, K. Akato, A. K. Naskar, A. M. Levine, R. J. Lee, S. –O. Kim, J. Zhang, S. Dai, and A. Manthiram, “Tire-derived carbon composite anodes for sodium-ion batteries.” *J. Power Sources* **2016**, 316, 232–238.

8. S. –M. Oh, P. Oh, S. –O. Kim, and A. Manthiram, “A Low-cost, Layered $Na[Cu_{0.2}(Fe_{1/3}Mn_{2/3})_{0.8}]O_2$ Cathode Assessed in a Full Cell with a P–TiP_2–C Composite Anode for Sodium-ion Batteries.” *J. Mater. Chem. A*, under review.

9. S. –O. Kim and A. Manthiram, “High-performance red P–based P–TiP_2–C nanocomposite anode for lithium-ion and sodium-ion storage.” *Chem. Mater.*, **2016**, DOI: 10.1021/acs.chemmater.6b02482.

10. S. –O. Kim and A. Manthiram, “Low-cost carbon-coated Si–Cu_3Si–Al_2O_3 nanocomposite anodes for high-performance lithium-ion batteries.” *J. Power Sources*, under review.

11. S. –O. Kim and A. Manthiram, “Chemically Bonded CuP_2/C Hybrid as a High-Performance Anode for Lithium-Ion Batteries.” in preparation.

References

1. J. M. Tarascon and M. Armand, *Nature*, 2001, **414**, 359-367.
2. J. B. Goodenough and Y. Kim, *Chem. Mater.*, 2010, **22**, 587-603.
3. L. Smith and B. Dunn, *Science*, 2015, **350**, 918-918.
4. D. Aurbach and Y. Cohen, *J. Electrochem. Soc.*, 1996, **143**, 3525-3532.
5. W. Xu, J. Wang, F. Ding, X. Chen, E. Nasybulin, Y. Zhang and J.-G. Zhang, *Energy Environ. Sci.*, 2014, **7**, 513-537.
6. S. Panero, E. Spila and B. Scrosati, *J. Electrochem. Soc.*, 1996, **143**, L29-L30.
7. L. Zhao, Y. S. Hu, H. Li, Z. X. Wang and L. Q. Chen, *Adv. Mater.*, 2011, **23**, 1385-1388.
8. Y. Qi, H. Guo, L. G. Hector and A. Timmons, *J. Electrochem. Soc.*, 2010, **157**, A558-A566.
9. J. S. Gnanaraj, R. W. Thompson, S. N. Iaconatti, J. F. DiCarlo and K. M. Abraham, *Electrochem. Solid-State Lett.*, 2005, **8**, A128-A132.
10. S. Yoon and A. Manthiram, *Electrochim. Acta*, 2011, **56**, 3029-3035.
11. M. Winter, J. O. Besenhard, M. E. Spahr and P. Novák, *Adv. Mater.*, 1998, **10**, 725-763.
12. M. N. Obrovac and V. L. Chevrier, *Chem. Rev.*, 2014, **114**, 11444-11502.
13. N. Nitta and G. Yushin, *Part. Part. Syst. Charact.*, 2014, **31**, 317-336.
14. C. M. Park, J. H. Kim, H. Kim and H. J. Sohn, *Chem. Soc. Rev.*, 2010, **39**, 3115-3141.
15. M. N. Obrovac and L. Christensen, *Electrochem. Solid-State Lett.*, 2004, **7**, A93-A96.

16. C. Chae, H.-J. Noh, J. K. Lee, B. Scrosati and Y.-K. Sun, *Adv. Funct. Mater.*, 2014, **24**, 3036-3042.

17. C. K. Chan, H. Peng, G. Liu, K. McIlwrath, X. F. Zhang, R. A. Huggins and Y. Cui, *Nat. Nanotechnol.*, 2008, **3**, 31-35.

18. X. Li, M. Gu, S. Hu, R. Kennard, P. Yan, X. Chen, C. Wang, M. J. Sailor, J.-G. Zhang and J. Liu, *Nat. Commun.*, 2014, **5**.

19. M. Ashuri, Q. He and L. L. Shaw, *Nanoscale*, 2016, **8**, 74-103.

20. L. Pan, H. Wang, D. Gao, S. Chen, L. Tan and L. Li, *Chem. Commun.*, 2014, **50**, 5878-5880.

21. J.-H. Cho and S. T. Picraux, *Nano Lett.*, 2013, **13**, 5740-5747.

22. N. Liu, L. Hu, M. T. McDowell, A. Jackson and Y. Cui, *ACS Nano*, 2011, **5**, 6487-6493.

23. J. Wang, X. Meng, X. Fan, W. Zhang, H. Zhang and C. Wang, *ACS Nano*, 2015, **9**, 6576-6586.

24. M.-H. Park, M. G. Kim, J. Joo, K. Kim, J. Kim, S. Ahn, Y. Cui and J. Cho, *Nano Lett.*, 2009, **9**, 3844-3847.

25. Y. Chen, J. Qian, Y. Cao, H. Yang and X. Ai, *ACS Appl. Mater. Interfaces*, 2012, **4**, 3753-3758.

26. M. D. Fleischauer, R. Mar and J. R. Dahn, *J. Electrochem. Soc.*, 2007, **154**, A151-A155.

27. T. Kim, S. Park and S. M. Oh, *Electrochem. Commun.*, 2006, **8**, 1461-1467.

28. S. Zhou, X. Liu and D. Wang, *Nano Lett.*, 2010, **10**, 860-863.

29. J.-H. Kim, H. Kim and H.-J. Sohn, *Electrochem. Commun.*, 2005, **7**, 557-561.

30. M. D. Fleischauer, J. M. Topple and J. R. Dahn, *Electrochem. Solid-State Lett.*, 2005, **8**, A137-A140.

31. D. Wang, J. Yang, J. Liu, X. Li, R. Li, M. Cai, T.-K. Sham and X. Sun, *J. Mater. Chem. A*, 2014, **2**, 2306-2312.

32. H.-Y. Lee and S.-M. Lee, *Electrochem. Commun.*, 2004, **6**, 465-469.

33. M. P. Bichat, J. L. Pascal, F. Gillot and F. Favier, *J. Phys. Chem. Solids*, 2006, **67**, 1233-1237.

34. Z. Shi, M. L. Liu and J. L. Gole, *Electrochem. Solid-State Lett.*, 2000, **3**, 312-315.

35. A. Dailly, J. Ghanbaja, P. Willmann and D. Billaud, *J. Appl. Electrochem.*, 2004, **34**, 885-890.

36. C. M. Park and H. J. Sohn, *Adv. Mater.*, 2010, **22**, 47-+.

37. Y. Hwa, J. H. Sung, B. Wang, C. M. Park and H. J. Sohn, *J. Mater. Chem.*, 2012, **22**, 12767-12773.

38. C. Marino, L. Boulet, P. Gaveau, B. Fraisse and L. Monconduit, *J. Mater. Chem.*, 2012, **22**, 22713-22720.

39. L. Wang, X. He, J. Li, W. Sun, J. Gao, J. Guo and C. Jiang, *Angew. Chem. Int. Ed.*, 2012, **51**, 9034-9037.

40. W. Li, Z. Yang, M. Li, Y. Jiang, X. Wei, X. Zhong, L. Gu and Y. Yu, *Nano Lett.*, 2016, **16**, 1546-1553.

41. S.-O. Kim and A. Manthiram, *Chem. Commun.*, 2016, **52**, 4337-4340.

42. J. F. Qian, X. Y. Wu, Y. L. Cao, X. P. Ai and H. X. Yang, *Angew. Chem. Int. Ed.*, 2013, **52**, 4633-4636.

43. J. Sun, G. Y. Zheng, H. W. Lee, N. Liu, H. T. Wang, H. B. Yao, W. S. Yang and Y. Cui, *Nano Lett.*, 2014, **14**, 4573-4580.

44. A. Bai, L. Wang, J. Li, X. He, J. Wang and J. Wang, *J. Power Sources*, 2015, **289**, 100-104.

45. M.-S. Park, J.-H. Kim, Y.-N. Jo, S.-H. Oh, H. Kim and Y.-J. Kim, *J. Mater. Chem.*, 2011, **21**, 17960-17966.

46. Y. Wang, L. Tian, Z. Yao, F. Li, S. Li and S. Ye, *Electrochim. Acta*, 2015, **163**, 71-76.

47. C. M. Park and H. J. Sohn, *Adv. Mater.*, 2007, **19**, 2465-2468.

48. J. Qian, D. Qiao, X. Ai, Y. Cao and H. Yang, *Chem. Commun.*, 2012, **48**, 8931-8933.

49. N. Yabuuchi, M. Kajiyama, J. Iwatate, H. Nishikawa, S. Hitomi, R. Okuyama, R. Usui, Y. Yamada and S. Komaba, *Nat. Mater.*, 2012, **11**, 512-517.

50. V. Palomares, P. Serras, I. Villaluenga, K. B. Hueso, J. Carretero-Gonzalez and T. Rojo, *Energy Environ. Sci.*, 2012, **5**, 5884-5901.

51. D. Kundu, E. Talaie, V. Duffort and L. F. Nazar, *Angew. Chem. Int. Ed.*, 2015, **54**, 3431-3448.

52. M. M. Doeff, Y. Ma, S. J. Visco and L. C. De Jonghe, *J. Electrochem. Soc.*, 1993, **140**, L169-L170.

53. R. Alcántara, J. M. Jiménez-Mateos, P. Lavela and J. L. Tirado, *Electrochem. Commun.*, 2001, **3**, 639-642.

54. R. Alcántara, P. Lavela, G. F. Ortiz and J. L. Tirado, *Electrochem. Solid-State Lett.*, 2005, **8**, A222-A225.

55. D. A. Stevens and J. R. Dahn, *J. Electrochem. Soc.*, 2000, **147**, 1271-1273.

56. H.-G. Wang, Z. Wu , F.-L. Meng , D.-L. Ma , X.-L. Huang , L.-M. Wang and X.-B. Zhang, *ChemSusChem*, 2013, **6**, 56-60.

57. L. Fu, K. Tang, K. Song, P. A. van Aken, Y. Yu and J. Maier, *Nanoscale*, 2014, **6**, 1384-1389.

58. S. Wenzel, T. Hara, J. Janek and P. Adelhelm, *Energy Environ. Sci.*, 2011, **4**, 3342-3345.

59. J. W. Wang, X. H. Liu, S. X. Mao and J. Y. Huang, *Nano Lett.*, 2012, **12**, 5897-5902.

60. J. F. Qian, Y. Chen, L. Wu, Y. L. Cao, X. P. Ai and H. X. Yang, *Chem. Commun.*, 2012, **48**, 7070-7072.

61. Y. Kim, K.-H. Ha, S. M. Oh and K. T. Lee, *Chem. Eur. J.*, 2014, **20**, 11980-11992.

62. W. J. Li, S. L. Chou, J. Z. Wang, H. K. Liu and S. X. Dou, *Nano Lett.*, 2013, **13**, 5480-5484.

63. Y. Kim, Y. Park, A. Choi, N. S. Choi, J. Kim, J. Lee, J. H. Ryu, S. M. Oh and K. T. Lee, *Adv. Mater.*, 2013, **25**, 3045-3049.

64. J. Song, Z. Yu, M. L. Gordin, S. Hu, R. Yi, D. Tang, T. Walter, M. Regula, D. Choi, X. Li, A. Manivannan and D. Wang, *Nano Lett.*, 2014, **14**, 6329-6335.

65. J. Sun, H.-W. Lee, M. Pasta, H. Yuan, G. Zheng, Y. Sun, Y. Li and Y. Cui, *Nat. Nanotechnol.*, 2015, **10**, 980-985.

66. W. J. Li, S. L. Chou, J. Z. Wang, J. H. Kim, H. K. Liu and S. X. Dou, *Adv. Mater.*, 2014, **26**, 4037-4042.

67. W. J. Li, S. L. Chou, J. Z. Wang, H. K. Liu and S. X. Dou, *Chem. Commun.*, 2015, **51**, 3682-3685.

68. W. J. Li, Q. R. Yang, S. L. Chou, J. Z. Wang and H. K. Liu, *J. Power Sources*, 2015, **294**, 627-632.

69. Y. Kim, Y. Kim, A. Choi, S. Woo, D. Mok, N. S. Choi, Y. S. Jung, J. H. Ryu, S. M. Oh and K. T. Lee, *Adv. Mater.*, 2014, **26**, 4139-4144.

70. J. Fullenwarth, A. Darwiche, A. Soares, B. Donnadieu and L. Monconduit, *J. Mater. Chem. A*, 2014, **2**, 2050-2059.

71. S. Yoon and A. Manthiram, *Chem. Mater.*, 2009, **21**, 3898-3904.

72. D. Applestone and A. Manthiram, *RSC Adv.*, 2012, **2**, 5411-5417.

73. I. T. Kim, E. Allcorn and A. Manthiram, *Phys. Chem. Chem. Phys.*, 2014, **16**, 12884-12889.

74. I. T. Kim, S. O. Kim and A. Manthiram, *J. Power Sources*, 2014, **269**, 848-854.

75. E. Allcorn and A. Manthiram, *J. Mater. Chem. A*, 2015, **3**, 3891-3900.

76. J. Leibowitz, E. Allcorn and A. Manthiram, *J. Power Sources*, 2015, **279**, 549-554.

77. H. L. Jia, Z. H. Zhang, Z. Qi, G. D. Liu and X. F. Bian, *J. Alloys Compd.*, 2009, **472**, 97-103.

78. Y. Yao, K. F. Huo, L. B. Hu, N. A. Liu, J. J. Ha, M. T. McDowell, P. K. Chu and Y. Cui, *ACS Nano*, 2011, **5**, 8346-8351.

79. P. G. Bruce, B. Scrosati and J. M. Tarascon, *Angew. Chem. Int. Ed.*, 2008, **47**, 2930-2946.

80. S. B. Son, S. C. Kim, C. S. Kang, T. A. Yersak, Y. C. Kim, C. G. Lee, S. H. Moon, J. S. Cho, J. T. Moon, K. H. Oh and S. H. Lee, *Adv. Energy Mater.*, 2012, **2**, 1226-1231.

81. U. Kasavajjula, C. S. Wang and A. J. Appleby, *J. Power Sources*, 2007, **163**, 1003-1039.

82. W. J. Lee, T. H. Hwang, J. O. Hwang, H. W. Kim, J. Lim, H. Y. Jeong, J. Shim, T. H. Han, J. Y. Kim, J. W. Choi and S. O. Kim, *Energy Environ. Sci.*, 2014, **7**, 621-626.

83. J. H. Ryu, J. W. Kim, Y. E. Sung and S. M. Oh, *Electrochem. Solid-State Lett.*, 2004, **7**, A306-A309.

84. M. Gauthier, D. Mazouzi, D. Reyter, B. Lestriez, P. Moreau, D. Guyomard and L. Roue, *Energy Environ. Sci.*, 2013, **6**, 2145-2155.

85. J. X. Song, S. R. Chen, M. J. Zhou, T. Xu, D. P. Lv, M. L. Gordin, T. J. Long, M. Melnyk and D. H. Wang, *J. Mater. Chem. A*, 2014, **2**, 1257-1262.

86. N. Liu, Z. D. Lu, J. Zhao, M. T. McDowell, H. W. Lee, W. T. Zhao and Y. Cui, *Nat. Nanotechnol.*, 2014, **9**, 187-192.

87. S. Y. Chen, P. H. Yeh, W. W. Wu, U. S. Chen, Y. L. Chueh, Y. C. Yang, S. Gwo and L. J. Chen, *ACS Nano*, 2011, **5**, 9202-9207.

88. D. Applestone, S. Yoon and A. Manthiram, *J. Mater. Chem.*, 2012, **22**, 3242-3248.

89. E. Allcorn and A. Manthiram, *J. Phys. Chem. C*, 2014, **118**, 811-822.

90. Y. Zheng, J. Yang, J. Wang and Y. NuLi, *Electrochim Acta*, 2007, **52**, 5863-5867.

91. B. Philippe, R. Dedryvere, J. Allouche, F. Lindgren, M. Gorgoi, H. Rensmo, D. Gonbeau and K. Edstrom, *Chem. Mater.*, 2012, **24**, 1107-1115.

92. Y. Cao, L. Nyborg and U. Jelvestam, *Surf. Interface Anal.*, 2009, **41**, 471-483.

93. B.-C. Yu, Y. Hwa, C.-M. Park and H.-J. Sohn, *J. Mater. Chem. A*, 2013, **1**, 4820-4825.

94. L. F. Cui, Y. Yang, C. M. Hsu and Y. Cui, *Nano Lett*, 2009, **9**, 3370-3374.

95. T. D. Bogart, D. Oka, X. T. Lu, M. Gu, C. M. Wang and B. A. Korgel, *ACS Nano*, 2014, **8**, 915-922.

96. A. M. Chockla, J. T. Harris, V. A. Akhavan, T. D. Bogart, V. C. Holmberg, C. Steinhagen, C. B. Mullins, K. J. Stevenson and B. A. Korgel, *J. Am. Chem. Soc.*, 2011, **133**, 20914-20921.

97. A. Netz, R. A. Huggins and W. Weppner, *J. Power Sources*, 2003, **119**, 95-100.

98. Y. S. Ye, X. L. Xie, J. Rick, F. C. Chang and B. J. Hwang, *J. Power Sources*, 2014, **247**, 991-998.

99. J. Li and J. R. Dahn, *J. Electrochem. Soc.*, 2007, **154**, A156-A161.

100. J. Saint, M. Morcrette, D. Larcher, L. Laffont, S. Beattie, J. P. Peres, D. Talaga, M. Couzi and J. M. Tarascon, *Adv. Funct. Mater.*, 2007, **17**, 1765-1774.

101. T. D. Hatchard and J. R. Dahn, *J. Electrochem. Soc.*, 2004, **151**, A838-A842.

102. J. C. Guo, A. Sun, X. L. Chen, C. S. Wang and A. Manivannan, *Electrochim. Acta*, 2011, **56**, 3981-3987.

103. Y. M. Lin, K. C. Klavetter, P. R. Abel, N. C. Davy, J. L. Snider, A. Heller and C. B. Mullins, *Chem. Commun.*, 2012, **48**, 7268-7270.

104. A. Magasinski, B. Zdyrko, I. Kovalenko, B. Hertzberg, R. Burtovyy, C. F. Huebner, T. F. Fuller, I. Luzinov and G. Yushin, *ACS Appl. Mater. Interfaces*, 2010, **2**, 3004-3010.

105. B. Koo, H. Kim, Y. Cho, K. T. Lee, N. S. Choi and J. Cho, *Angew. Chem. Int. Ed.*, 2012, **51**, 8762-8767.

106. X. Huang, H. Kim, S. Cui, P. T. Hurley and J. Chen, *Energy Technol.*, 2013, **1**, 305-308.

107. M. Au, Y. He, Y. Zhao, H. Ghassemi, R. S. Yassar, B. Garcia-Diaz and T. Adams, *J. Power Sources*, 2011, **196**, 9640-9647.

108. S. O. Kim and A. Manthiram, *J. Mater. Chem. A*, 2015, **3**, 2399-2406.

109. S. Chae, M. Ko, S. Park, N. Kim, J. Ma and J. Cho, *Energy Environ. Sci.*, 2016, **9**, 1251-1257.

110. C. Suryanarayana and N. Al-Aqeeli, *Prog. Mater. Sci.*, 2013, **58**, 383-502.

111. M. W. Forney, M. J. Ganter, J. W. Staub, R. D. Ridgley and B. J. Landi, *Nano Lett.*, 2013, **13**, 4158-4163.

112. H. J. Kim, S. Choi, S. J. Lee, M. W. Seo, J. G. Lee, E. Deniz, Y. J. Lee, E. K. Kim and J. W. Choi, *Nano Lett.*, 2016, **16**, 282-288.

113. S. Yoon and A. Manthiram, *J. Mater. Chem.*, 2010, **20**, 236-239.

114. A. Mani, P. Aubert, F. Mercier, H. Khodja, C. Berthier and P. Houdy, *Surf. Coat. Technol.*, 2005, **194**, 190-195.

115. M. C. Biesinger, L. W. M. Lau, A. R. Gerson and R. S. C. Smart, *Appl. Surf. Sci.*, 2010, **257**, 887-898.

116. Y. H. Chang and H. T. Chiu, *J. Mater. Res.*, 2002, **17**, 2779-2782.

117. N. K. Allam, F. Alamgir and M. A. El-Sayed, *ACS Nano*, 2010, **4**, 5819-5826.

118. G. T. S. How, A. Pandikumar, H. N. Ming and L. H. Ngee, *Sci. Rep.*, 2014, **4**.

119. J. E. Krzanowski and R. E. Leuchtner, *J. Am. Ceram. Soc.*, 1997, **80**, 1277-1280.

120. P. C. Tsai, Y. F. Hwang, J. Y. Chiang and W. J. Chen, *Surf. Coat. Technol.*, 2008, **202**, 5350-5355.

121. M. M. O. Thotiyl, S. A. Freunberger, Z. Q. Peng, Y. H. Chen, Z. Liu and P. G. Bruce, *Nat. Mater.*, 2013, **12**, 1049-1055.

122. M. Zhu, C. J. Weber, Y. Yang, M. Konuma, U. Starke, K. Kern and A. M. Bittner, *Carbon*, 2008, **46**, 1829-1840.

123. H. J. Shin, K. K. Kim, A. Benayad, S. M. Yoon, H. K. Park, I. S. Jung, M. H. Jin, H. K. Jeong, J. M. Kim, J. Y. Choi and Y. H. Lee, *Adv. Funct. Mater.*, 2009, **19**, 1987-1992.

124. I. A. Courtney and J. R. Dahn, *J. Electrochem. Soc.*, 1997, **144**, 2943-2948.

125. J. F. Qian, Y. Xiong, Y. L. Cao, X. P. Ai and H. X. Yang, *Nano Lett.*, 2014, **14**, 1865-1869.

126. F. Zhao, N. Han, W. Huang, J. Li, H. Ye, F. Chen and Y. Li, *J. Mater. Chem. A*, 2015, **3**, 21754-21759.

127. W.-J. Li, S.-L. Chou, J.-Z. Wang, H.-K. Liu and S.-X. Dou, *J. Mater. Chem. A*, 2016, **4**, 505-511.

128. Z. Yu, J. Song, M. L. Gordin, R. Yi, D. Tang and D. Wang, *Adv. Sci.*, 2015, **2**, n/a-n/a.

129. J. Song, Z. Yu, M. L. Gordin, X. Li, H. Peng and D. Wang, *ACS Nano*, 2015, **9**, 11933-11941.

130. W. Xing, J. S. Xue and J. R. Dahn, *J. Electrochem. Soc.*, 1996, **143**, 3046-3052.

131. Y. Wen, K. He, Y. Zhu, F. Han, Y. Xu, I. Matsuda, Y. Ishii, J. Cumings and C. Wang, *Nat. Commun.*, 2014, **5**.

132. S.-O. Kim and A. Manthiram, *ACS Appl. Mater. Interfaces*, 2015, **7**, 14801-14807.

133. J. R. Szczech and S. Jin, *Energy Environ. Sci.*, 2011, **4**, 56-72.

134. J. Qian, X. Wu, Y. Cao, X. Ai and H. Yang, *Angew. Chem. Int. Ed.*, 2013, **52**, 4633-4636.

135. Y. J. Zhu, Y. Wen, X. L. Fan, T. Gao, F. D. Han, C. Luo, S. C. Liou and C. S. Wang, *ACS Nano*, 2015, **9**, 3254-3264.

136. J. B. Goodenough and K.-S. Park, *J. Am. Chem. Soc.*, 2013, **135**, 1167-1176.

137. V. Etacheri, R. Marom, R. Elazari, G. Salitra and D. Aurbach, *Energy Environ. Sci.*, 2011, **4**, 3243-3262.

138. N. Yabuuchi, K. Kubota, M. Dahbi and S. Komaba, *Chem. Rev.*, 2014, **114**, 11636-11682.

139. M. Dahbi, N. Yabuuchi, M. Fukunishi, K. Kubota, K. Chihara, K. Tokiwa, X.-f. Yu, H. Ushiyama, K. Yamashita, J.-Y. Son, Y.-T. Cui, H. Oji and S. Komaba, *Chem. Mater.*, 2016, **28**, 1625-1635.

140. P. M. A. Sherwood, *Surf. Sci. Spectra*, 2002, **9**, 62-66.

141. D. W. Boukhvalov, D. M. Korotin, A. V. Efremov, E. Z. Kurmaev, C. Borchers, I. S. Zhidkov, D. V. Gunderov, R. Z. Valiev, N. V. Gavrilov and S. O. Cholakh, *Phys. Status Solidi B*, 2015, **252**, 748-754.

142. T. Ramireddy, T. Xing, M. M. Rahman, Y. Chen, Q. Dutercq, D. Gunzelmann and A. M. Glushenkov, *J. Mater. Chem. A*, 2015, **3**, 5572-5584.

143. L. Monconduit, F. Gillot, M.-L. Doublet and F. Lemoigno, *Ionics*, 2003, **9**, 56-63.

144. F. Gillot, M. P. Bichat, F. Favier, M. Morcrette, J. M. Tarascon and L. Monconduit, *Ionics*, 2003, **9**, 71-76.

145. M. P. Bichat, F. Gillot, L. Monconduit, F. Favier, M. Morcrette, F. Lemoigno and M. L. Doublet, *Chem. Mater.*, 2004, **16**, 1002-1013.

146. S.-G. Woo, J.-H. Jung, H. Kim, M. G. Kim, C. K. Lee, H.-J. Sohn and B. W. Cho, *J. Electrochem. Soc.*, 2006, **153**, A1979-A1983.

Vita

Sang Ok Kim was born in 1982, in Seoul, Republic of Korea. He received his B.S. and M.S. degrees in Materials Science and Engineering from Seoul National University in Seoul, Republic of Korea, respectively, in 2005 and 2007. He worked at Korea Institute of Science and Technology from 2007 to 2012 as a research scientist, carrying out research on lithium-ion battery and hybrid capacitor systems. He entered the graduate program at The University of Texas at Austin in August 2012. His research is focused on the development of alloy-based anodes for lithium- and sodium-ion batteries.

Email address: kso1982@gmail.com

This dissertation was typed by the author.